THE EFFECTS OF MOISTURE ON MOUNTAIN LEE WAVES

by

DALE RICHARD DURRAN

B.S., California State Polytechnic University, San Luis Obispo (1974)
M.A., University of California at Berkeley (1975)

SUBMITTED TO THE DEPARTMENT OF METEOROLOGY AND PHYSICAL OCEANOGRAPHY IN PARTIAL FULFILLMENT OF THE REQUIREMENTS FOR THE DEGREE OF

DOCTOR OF PHILOSOPHY

at the

MASSACHUSETTS INSTITUTE OF TECHNOLOGY

August 1981

©Dale Richard Durran 1981

The author hereby grants to M.I.T. permission to reproduce and to distribute copies of this thesis document in whole of in part

Signature of Author _____
Department of Meteorology and Physical Oceanography
July 28, 1981

Certified by _____
Ronald G. Prinn
Thesis Supervisor

Accepted by _____
Peter B. Stone
Chairman, Departmental Graduate Committee

Archives
MASSACHUSETTS INSTITUTE OF TECHNOLOGY
MAR 22 1982
LIBRARIES

THE EFFECTS OF MOISTURE ON MOUNTAIN LEE WAVES

by

DALE RICHARD DURRAN

B.S., California State Polytechnic University, San Luis Obispo (1974)
M.A., University of California at Berkeley (1975)

SUBMITTED TO THE DEPARTMENT OF METEOROLOGY AND PHYSICAL OCEANOGRAPHY IN PARTIAL FULFILLMENT OF THE REQUIREMENTS FOR THE DEGREE OF

DOCTOR OF PHILOSOPHY

at the

MASSACHUSETTS INSTITUTE OF TECHNOLOGY

August 1981

©Dale Richard Durran 1981

The author hereby grants to M.I.T. permission to reproduce and to distribute copies of this thesis document in whole of in part

Signature of Author_____
Department of Meteorology and Physical Oceanography
July 28, 1981

Certified by_____
Ronald G. Prinn
Thesis Supervisor

Accepted by_____
Peter B. Stone
Chairman, Departmental Graduate Committee

Archives
MASSACHUSETTS INSTITUTE OF TECHNOLOGY
MAR 22 1982
LIBRARIES

THE EFFECTS OF MOISTURE ON MOUNTAIN LEE WAVES

by

DALE DURRAN

Submitted to the Department of Meteorology and Physical Oceanography
on July 28, 1981 in partial fulfillment of the requirements
for the Degree of Doctor of Philosophy

ABSTRACT

In this study a numerical model was used to examine the impact of moisture on the dynamics of mountain lee waves. The model, which was originally designed to simulate convective storms, was modified for lee wave calculations and tested to verify its accuracy. The effects of moisture on trapped and propagating waves were considered separately. In both cases, the release of latent heat was found to significantly influence the wave dynamics.

When moisture was introduced into the lowest layer of a two layer tropospheric structure favorable for the development of trapped lee waves, three different behaviors were encountered. If the atmosphere was convectively unstable, any clouds which formed destroyed the lee waves. If the effective moist stability in the wave environment was weak, but positive, the waves were distorted and untrapped as the upstream humidity increased. If there was strong moist stability in the lowest layer, changes in the upstream humidity changed the tuning properties of the trapped waves. In the last instance, moisture could amplify or damp the wave, depending on the wavenumber spectrum of the orographic forcing. The presence of upper level moisture could either damp or amplify trapped waves depending on the details of the dry wave structure.

The investigation of propagating waves concentrated on atmospheric structures in which there were no sharp gradients in the Scorer parameter structure, so there was little downward partial reflection of wave energy. The only moisture profiles considered were ones in which the relative humidity was constant with height or a cloud was present at low levels. When precipitation was not present, the introduction of moisture into the flow damped the waves and reduced the momentum flux. This effect was stronger in the finite amplitude waves than in their linear counterparts. When precipitation occurred, the wave amplitudes and the wave drags were stronger than those produced by nonprecipitating flows, but, except for the case where liquid water rained out instantly after condensation, the precipitating waves were still much weaker than the dry waves.

Thesis Supervisor: Dr. Ronald Prinn

Title: Associate Professor of Meteorology

ACKNOWLEDGEMENTS

This thesis was completed while the author was a Graduate Research Assistant at the National Center for Atmospheric Research (NCAR)*. It is with pleasure and deep gratitude that I wish to thank my primary adviser, Dr. Joseph Klemp. His guidance and encouragement made the thesis possible, and his friendship made it pleasant. I am most appreciative of the guidance provided by my other joint thesis advisers, Dr. Douglas Lilly and Dr. Ronald Prinn. I would also like to thank Drs. Richard Rotunno, John Brown, Terry Clark and Ronald Smith for their invaluable answers to my many questions. I am indebted to Betty Wilson, the NCAR computing facility, and the NCAR graphics department for their assistance, and to Ursula Rosner and Verlene Leeburg who did a fine job typing this thesis. I would also like to thank Jane McNabb and Virginia Mills for tirelessly sorting out my nonresident student status with the MIT administration. I wish to express my gratitude to NCAR for the support provided me as a Graduate Assistant and UCAR Fellow, and to M.I.T. for the support I received as a research assistant on NASA grant NSG-2010.

*The National Center for Atmospheric Research is sponsored by the National Science Foundation.

Dale Durran received a B.S. in mathematics from the California Polytechnic State University at San Luis Obispo in 1974, and a M.A. in mathematics from the University of California at Berkeley in 1975. In 1976 and 1977 he was involved in the computer modeling of air pollution as a staff scientist at Systems Applications Inc. in San Rafael, California.

TABLE OF CONTENTS

I. INTRODUCTION

Although dry mountain lee waves have been studied extensively for the last 40 years, the influence of moisture on the dynamics of these waves has received little attention. This lack of research is due in part to the qualitative success with which dry dynamical formulations have been able to reproduce lee wave flows, and in part to the difficulty of including latent heating in theoretical models. There is, however, evidence which suggests that moisture can significantly modify the lee wave flow. Barcilon et al. (1979) have found that the presence of low level moisture in an almost linear model reduces the wave drag produced by hydrostatic mountain waves in an atmosphere with constant upstream stability and windspeed. Lilly and Klemp (private communication) have noted that their dry linear mountain wave model tends to over-predict the actual wave response under conditions of high upstream humidity. Larsson (1954) has flown airplanes through lenticular clouds and observed that the upward motion at the leading edge of the cloud is sometimes twice as strong as the downward motion at its trailing edge, suggesting that moisture may distort the sinusoidal wave structure predicted by dry linear theory. In this dissertation I will investigate the effects of moisture on mountain lee waves.

Two previous studies have also been designed to assess the impact of moisture on mountain waves. Barcilon et al. (1979) examined the effects of nonprecipitating clouds on linear hydrostatic waves by replacing the cloudy regions with dry regions of reduced stability.

Since the cloud boundaries were not known apriori, an iterative procedure was used to match the clouds with the regions of upward displacement and obtain a self-consistent flow. In order to study the impact of precipitation, Barcilon et al. (1980) considered a similar linear hydrostatic model in which any condensed water was assumed to rain out instantly. In this second study, the iterative technique was abandoned, and the perturbations produced by latent heating were assumed to be small so that the cloud boundaries could be determined from the dry streamline displacements. In both of these studies the microphysics are very idealized, and the flow regimes examined are limited to linear hydrostatic waves in an atmosphere in which the dry and moist stabilities, and the windspeed, are constant with height.

In order to investigate a wider variety of realistic situations, I will develop a numerical model to compute the influence of moisture on mountain lee waves. The numerical approach has two basic advantages. First, the microphysics can easily be incorporated in a relatively realistic manner through a simple rain parameterization, and second, the study need not be limited to flows for which dry analytic solutions are available. In particular, the numerical model can be designed to simulate nonlinear, nonhydrostatic compressible, time dependent lee waves produced by mountains of arbitrary shape. It is important to have the ability to investigate nonlinear wave amplitudes since the influence of moisture is nonlinear and should be free to interact with other nonlinearities. It is also important to include nonhydrostatic effects since nonhydrostatic resonant waves are among the preferred locations for wave clouds. Even though many of

the cases will be studied in an essentially steady state, there are advantages to a time dependent calculation. The time dependent approach guarantees that any steady state obtained is stable, and it allows the simulation of convective regimes in which the atmospheric response is inherently time dependent.

This dissertation is organized as follows: Chapter II is a review of that portion of the voluminous literature on mountain lee waves which is particularly relevant to the moisture problem. The numerical model is described in chapter III. Tests are presented in chapter IV in which the model is compared with other mountain wave solutions. The effects of moisture on trapped and propagating waves are discussed in chapters V and VI. The conclusions and opportunities for future research are presented in chapter VII.

II. REVIEW OF MOUNTAIN WAVE RESEARCH

The basic flow pattern across a long ridge of mountains is determined by the mountain width. If the ridge is sufficiently wide so that the time required for air to cross it is greater than order 1/f, (where f is the Coriolis parameter), rotational effects generate a disturbance with large displacements in the horizontal x-y plane. As the width decreases, the perturbations in the horizontal plane disappear and waves in the vertical x-z plane develop. In this thesis we will concentrate on narrow mountain ridges (<100 km wide) so that rotation can be neglected. When the wind blows over such a ridge, air parcels are displaced vertically and, if the atmosphere is stably stratified, upon passing the ridge they descend and oscillate about their equilibrium levels. The gravity waves which result, called mountain lee waves, have been observed in mountainous regions all over the world. It is often convenient to divide mountain lee waves into two categories; those which propagate vertically, and those whose wave energy is trapped near the surface.

In this chapter we will briefly review some observations and previous theoretical studies which are particularly relevant to the moisture problem. We will be primarily concerned with the flow across a very long uniform ridge, in which case the dynamics are two dimensional. Trapped and propagating waves are considered separately.

A. Propagating Waves

Vertically propagating waves are often associated with large mountains. They produce strong downslope winds in the lee of the mountain, and exert a significant drag on the upper atmosphere which can affect the larger, synoptic scale airflow. The potential temperature field observed by Lilly and Zipser (1972) in a strong propagating wave generated by the Front Range in the Colorado Rockies is shown in Fig. 2.1. The flow at all heights is dominated by one very strong oscillation with a horizontal wavelength of approximately 60 km; only minimal wave activity appears further downstream. This wave produced winds with gusts exceeding 50 ms^{-1} in Boulder. Note the presence of a cap cloud over the ridge crest and a small rotor cloud in the short waves to the lee of the main wave.

The first mathematical investigations into the dynamics of these waves relied on linear theory. In the standard approach the flow is assumed to be two-dimensional, steady, inviscid and adiabatic. The equations of motion, continuity, thermodynamics and state are linearized about a horizontally uniform basic state with a mean flow across the mountain. If, as is typically the case, the horizontal windspeed is very much less than the speed of sound, these equations may be manipulated to form the following equation for the vertical velocity w

$$\tilde{w}_{xx} + \tilde{w}_{zz} + k_s^2(z)\tilde{w} = 0 \quad , \tag{2.1}$$

where

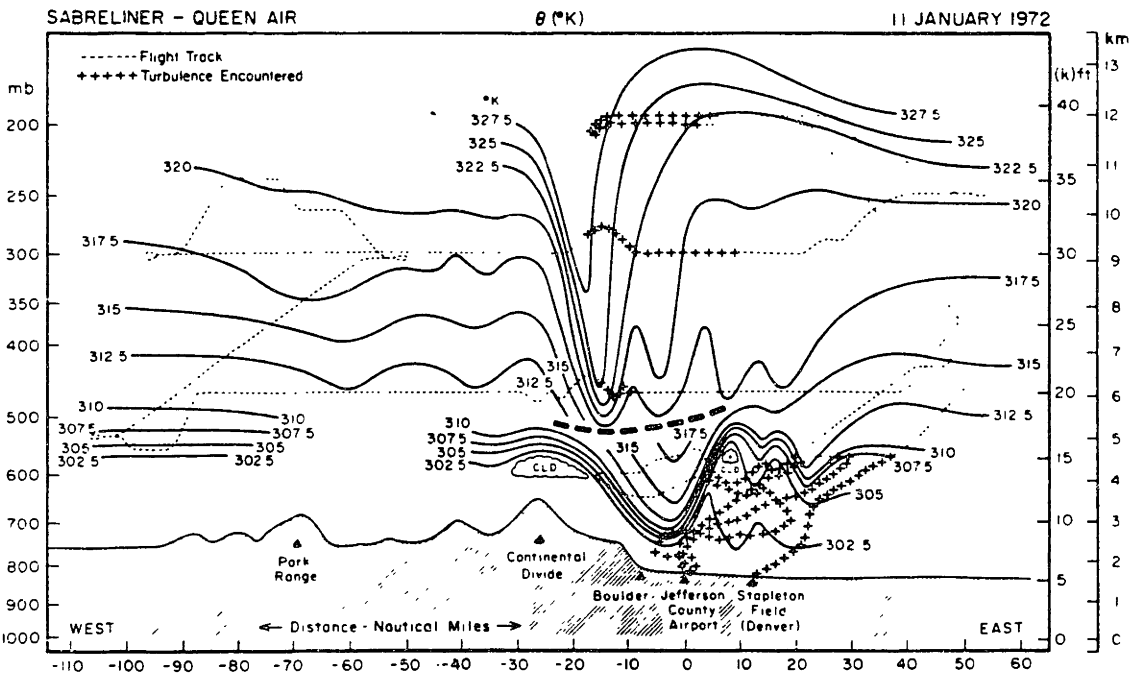

Figure 2.1. Cross-section of the potential temperature field (K) along an east-west line through Boulder, as obtained from analysis of the Queen Air and Sabreliner data on 11 January 1972. For steady adiabatic flow, these isentropes are good indicators of the streamlines of the air motion. Data above the heavy dashed line are from the Sabreliner, taken between 1700 and 2000 MST, while those below this line are primarily from the Queen Air taken from 1330 to 1500. Flight tracks are indicated by the dashed lines, except for crosses in turbulent portions. From Lilly and Zipser (1972).

$$k_s^2(z) = \frac{N^2}{\bar{u}^2} - \frac{\bar{u}_{zz}}{\bar{u}} - \frac{S\bar{u}_z}{\bar{u}} - \frac{1}{4}S^2 - \frac{1}{2}S_z \ , \qquad (2.2)$$

and

$$\tilde{w} = \left(\frac{\rho}{\rho_0}\right)^{1/2} w \ , \quad N^2 = g\frac{\partial \ell n\bar{\theta}}{\partial z} \ , \quad S = \frac{\partial \ell n(\bar{\rho})}{\partial z} \ . \qquad (2.3)$$

Overbars refer to the vertically stratified basic state; the other symbols are defined in the Appendix. Except near the surface where $\bar{u}_z$ is large, or when the temperature structure is nearly adiabatic, the last three terms in $k_s^2(z)$ can be ignored. If the horizontal structure is Fourier decomposed the equation for the amplitude of the k^{th} component, $\hat{w}(z)$ is:

$$\hat{w}_{zz} + (k_s^2 - k^2)\hat{w} = 0 \ . \qquad (2.4)$$

A free slip boundary condition is applied at z = 0:

$$w(0,x) = \bar{u}(0)\frac{\partial z_s}{\partial x} \ , \qquad (2.5)$$

where $z_s(x)$ is the height of the mountain. Note that this has been linearized by applying it at z = 0 instead of $z = z_s$. The solution is determined by specifying the radiation boundary condition at $z = \infty$.

Analytic solutions to (2.4) may be obtained for certain choices of z_s when k_s^2 has a simple structure. Lyra (1943) and Queney (1947, 1948) obtained solutions for an isothermal atmosphere with no wind shear. Lyra studied rather unrealistic rectangular mountains, but Queney chose a "Witch of Agnesi" mountain profile

$$z_s(x) = \frac{ha^2}{x^2 + a^2} , \qquad (2.6)$$

where h is the mountain height and a is the mountain half width at half-height. Due to its easy Fourier decomposition and physically realistic shape, this profile has been widely used in later studies. Queney observed that the response of the airstream to the mountain forcing depended upon the ratio of the effective mountain width and the critical wavelength. The critical wavelength, $L_c = 2\pi/k_s$, which is independent of the mountain, is the natural horizontal wavelength which lee waves would approach asymptotically in the absence of continued forcing. For mountains much narrower than L_c the flow follows the terrain contours and no waves develop. For mountains much wider than L_c the flow is approximately hydrostatic, and a single wave forms above the crest as illustrated in Fig. 2.2. When the mountain width is the same order as L_c the strongest atmospheric response occurs, and several waves appear which damp downstream; they are illustrated in Fig. 2.3. Large mountains are usually much wider than the values of L_c commonly encountered in actual lee wave flows, so it is often appropriate to assume that propagating waves are hydrostatic.

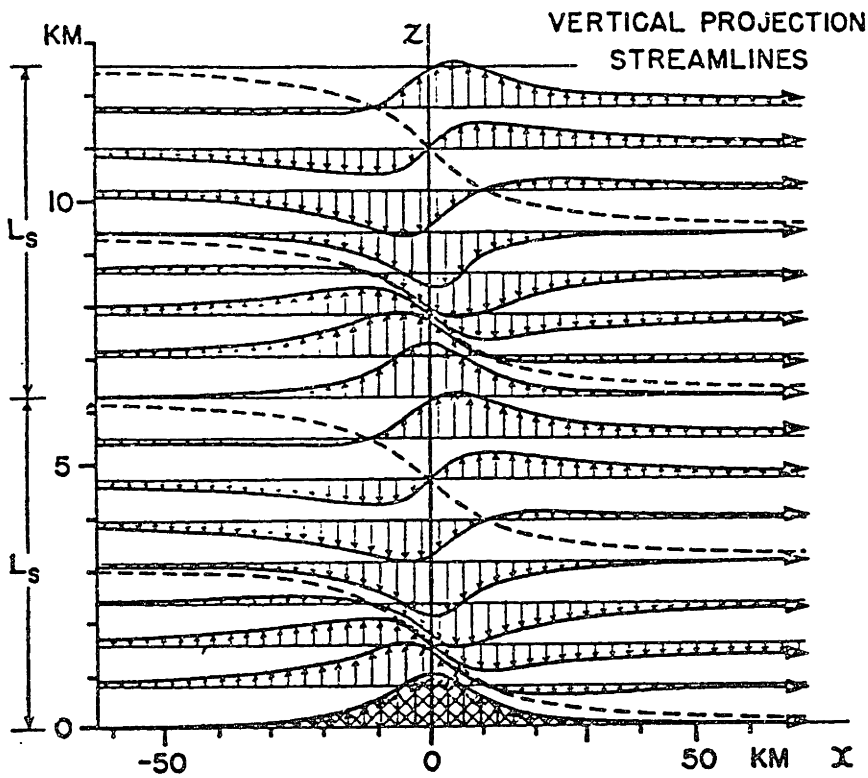

Figure 2.2. Flow over a mountain whose width is large in comparison to the critical wavelength. The effect of the density factor $(\rho/\rho_0)^{-1/2}$ is ignored. From Holmboe and Klieforth (1957).

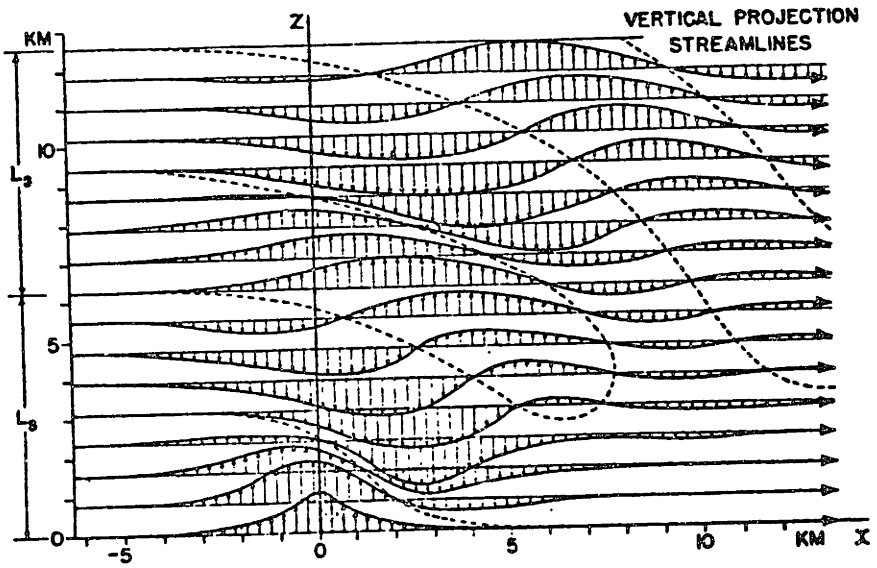

Figure 2.3. Flow over a mountain whose width is the order of the critical wavelength. The effect of the density factor $(\rho/\rho_0)^{-1/2}$ is ignored. From Holmboe and Klieforth (1957).

Klemp and Lilly (1975) noted that the upstream flow during strong mountain wave events in the Colorado Rockies frequently has a three layer structure in which regions of strong stability in the lower troposphere and the stratosphere surround a region of weak stability in the upper troposphere. They constructed solutions for linear hydrostatic waves with constant stability and vertical wind shear in each layer of a multi-layer atmosphere, and found that the wave amplitude was very sensitive to changes in the thickness of the tropospheric layers. The strongest waves were obtained when there was a phase shift of one-half vertical wavelength between the ground and the tropopause. The wave amplification is produced by the partial reflection of upward propagating wave energy at the interface between adjacent layers.

Propagating mountain waves can produce large downward fluxes of horizontal momentum which can significantly affect the synoptic scale flow. Eliassen and Palm (1960) investigated the momentum transfer in steady, linear mountain waves. They showed that the troughs and crests must tilt upstream with height in waves which transfer energy upward and momentum downward. They also noted that, in the absence of resonant lee waves and critical levels, the vertical flux of horizontal momentum is constant with height in a steady mountain wave. However, as discussed by Klemp and Lilly (1980), the momentum flux may approach its constant steady state value very slowly in time dependent flows.

The preceding studies have been limited to small amplitude waves. Long (1953,1955) obtained exact solutions for the stationary flow of an inviscid, incompressible, stratified fluid over an obstacle of finite height. He showed that if $\bar{u}^2\rho$ is constant and the density is linear in z, the following equation for the deviation of a streamline from its upstream height $\delta(x,z)$ can be derived without making any small amplitude assumptions.

$$\delta_{xx} + \delta_{zz} + \frac{N^2}{\bar{u}^2}\delta = 0 \quad . \tag{2.7}$$

This equation is linear and can easily be solved, however, the bottom boundary condition:

$$\delta(x, z_s(x)) = z_s(x) \quad , \tag{2.8}$$

remains a problem since it cannot be linearized without invoking a hypothesis that the disturbance is small. Long circumvented this by first solving (2.7) with a linearized boundary condition and then determining the finite amplitude mountain profile by solving (2.8) for z_s. This inverse approach has the disadvantage that the shape of the mountain depends on $N^2/\bar{u}^2$ so that the N and $\bar{u}$ dependence of the flow over an obstacle of fixed dimensions cannot easily be calculated.

More recently, Miles (1968) obtained solutions for certain mountain shapes which can be specified directly. Figure 2.4 shows computations by Huppert (in Appendix to Miles, 1968) for the flow over

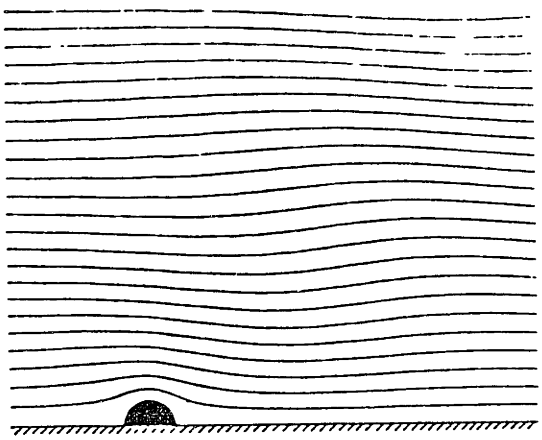

The streamline pattern for flow over a semi-circular obstacle on the basis of Long's model for $\varkappa = 0.5$. The flow is only slightly rotational.

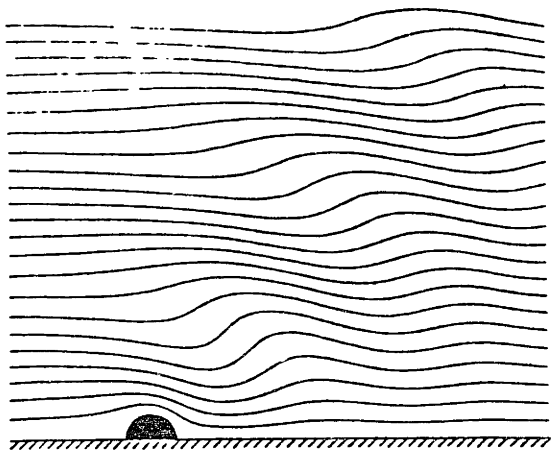

The streamline pattern for flow over a semi-circular obstacle on the basis of Long's model for $\varkappa = 1.0$.

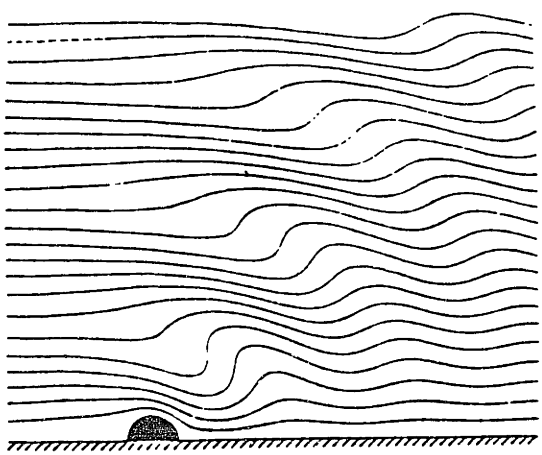

The streamline pattern for flow over a semi-circular obstacle on the basis of Long's model for $\varkappa = \varkappa_c \doteq 1.3$.

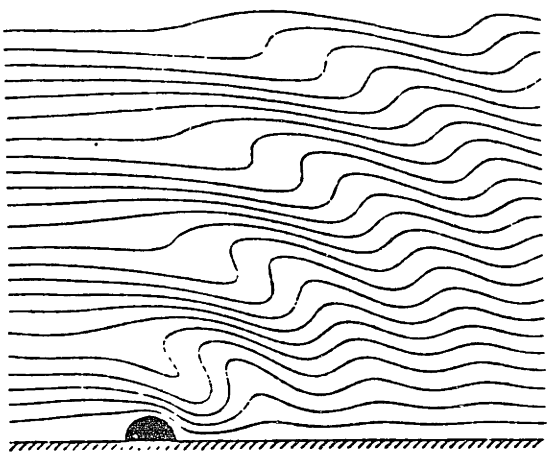

The streamline pattern for flow over a semi-circular obstacle on the basis of Long's model for $\varkappa = 1.5$. This flow contains density inversions in the regions of reversed flow and would be at least locally unstable.

Figure 2.4. Flow over a half-cylinder of finite height. From Miles (1969).

a half cylinder for various values of the parameter $r = HN/\bar{u}$ where H is the maximum height of the obstacle. As r increases, the slope of the wavefront steepens; at the critical value $r = r_c$ (r_c is 1.3 in the figure), the slope goes vertical. For $r > r_c$ the solutions may not be valid because, in the vicinity of the overturned streamlines, the fluid is convectively unstable.

Lilly and Klemp (1979) have obtained a solution to Long's equation for hydrostatic flow over an obstacle of arbitrary shape. They found that mountains with steep lee slopes and gentle windward slopes generate stronger waves than a symmetric mountain of the same height. The weakest waves were produced by mountains with steep windward slopes and gentle lee slopes. Smith (1977) obtained the same result from a perturbation analysis of the linear equations.

Although the solutions to Long's equation include finite amplitude effects exactly, they apply only to an incompressible fluid. Long's approach has been extended to compressible fluids by Claus (1964).

At present, in order to examine nonlinear lee waves in an atmosphere with arbitrary windspeed and stability profiles, one must rely on numerical simulation. Numerical models designed to calculate the airflow over mountains must include careful treatments of the upper and lower boundary conditions. While every numerical model requires boundary conditions, the top and bottom boundaries are critically important in the case of mountain waves. The bottom boundary is important because that is where the forcing is applied. At the top boundary it is important to minimize unphysical reflections

of wave energy back into the computational domain. Since the structure of mountain waves is very strongly affected by the reflection or partial reflection of wave energy at various levels in the atmosphere, an inadequate approximation to the radiation boundary condition can seriously affect the results. Although a number of investigators have applied numerical models to this problem, not all have included a proper treatment of the upper boundary. I will consider just the two most recent and careful studies.

Klemp and Lilly (1978) constructed a time dependent, two dimensional, adiabatic model. The model is hydrostatic, so it cannot produce resonant lee waves, but it seems capable of producing long wave disturbances of the type shown in Fig. 2.1, which generate severe downslope winds. The model uses isentropic coordinates, which eliminates vertical advection terms and greatly simplifies the bottom boundary condition since, in free slip adiabatic flow, the mountain profile is an isentrope. However, isentropic coordinates cannot be used to describe a breaking wave (in which the streamlines overturn). Klemp and Lilly avoid overturning by the use of a turbulent adjustment procedure which stabilizes the flow wherever the Richardson number falls below 0.25. The reflection of energy at the top boundary is minimized by adding a sponge layer, in which the viscosity gradually increases with height, to the top of the computational domain. The model has been able to convincingly reproduce analytic solutions and simulate the hydrostatic portion of the flow in two observational cases. The isentropes calculated for the January 11, 1972 case are shown in Fig. 2.5, and may be compared with the observations plotted in Fig. 2.1.

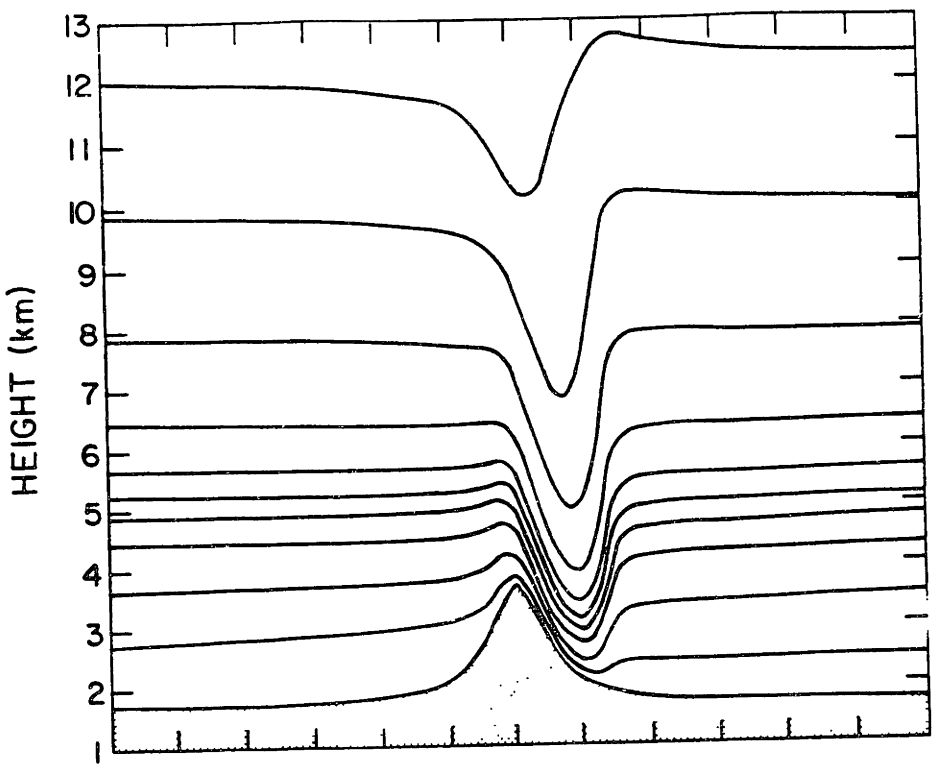

Figure 2.5. Potential temperature field from numerical simulation of 11 January 1972 case. From Klemp and Lilly (1975).

The numerical model developed by Clark and Peltier (1977) is quite different. Their model is also time dependent, two dimensional, and adiabatic, but it is based on the anelastic equations so it is nonhydrostatic. The terrain is included through a coordinate transformation which maps the computational domain, with its arbitrary bottom boundary, into a rectangle. A sponge layer is used to remove wave energy at the top boundary. Subgrid scale turbulence is parameterized as a function of Richardson number after Lilly (1962). Free slip conditions were assumed at the top and bottom of the model. Like Klemp and Lilly, they have been able to simulate both analytically calculable and observed flows rather well. Their simulation of the January 11, 1972 mountain wave is shown in Fig. 2.6.

Peltier and Clark (1979) have emphasized the importance of wave breaking on the flow dynamics. In their calculations, after the streamlines overturn the wave drag on the mountain increases far beyond the value predicted by linear theory. They propose that the turbulent region where the wave has broken reflects wave energy back toward the surface, producing strong resonant waves. They have criticized Klemp and Lilly's model on the grounds that an isentropic coordinate model cannot represent a breaking wave (since the transformation to isentropic coordinates is then undefined). They also suggest that a hydrostatic model should not be used since it eliminates resonant waves which may be important to the dynamics. Further discussion of the merits of these models may be found in the correspondence between Lilly and Klemp (1980), and Peltier and Clark (1980).

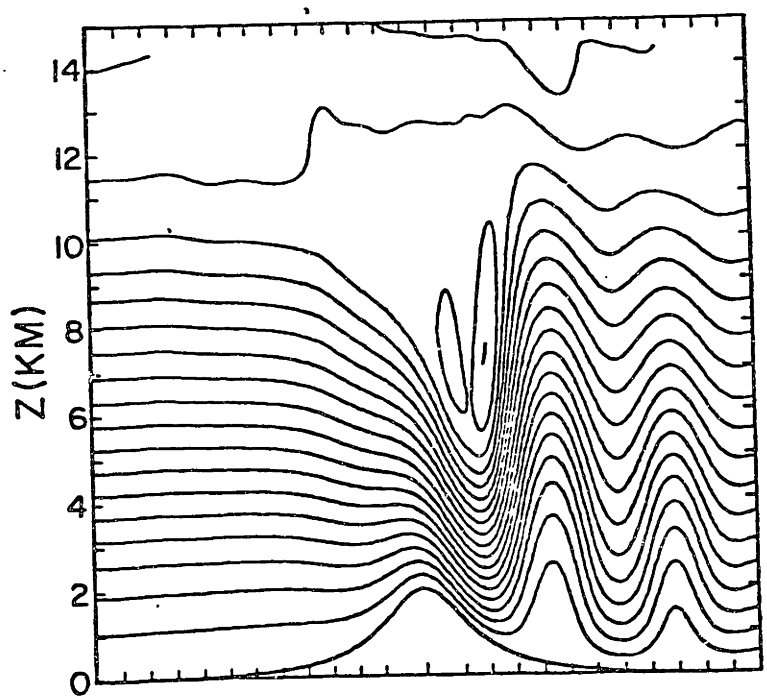

Figure 2.6. Potential temperature field from numerical simulation of 11 January 1972 case. From Peltier and Clark (1979).

Only a few papers have appeared which consider the influence of diabatic heating in clouds on the airflow over a mountain. The approaches taken by Fraser et al. (1973) and Barcilon et al. (1979) are similar. Fraser et al. were interested only in obtaining a flow model for use in predicting upslope precipitation; they do not consider resonant waves. Barcilon et al. do not examine resonant waves either, but they are more concerned with the wave dynamics and present calculations of the effect of moisture on mountain wave drag, so I will concentrate primarily on their work.

Barcilon et al. (hereafter referred to as BJD) consider linearized, inviscid, two dimensional motion, in hydrostatic balance. They incorporate the diabatic heating by replacing the cloudy regions with regions of reduced stability. Clouds are assumed to condense when the displacement, δ, of a streamline from its height upstream exceeds a critical values δ_s. Condensation is allowed only at low levels; at higher altitudes the air is assumed dry so that $\delta_s = \infty$. The resulting equation for the streamline displacement is

$$\begin{aligned} \bar{u}^2\delta_{zz} + N^2\delta &= 0 \qquad \delta < \delta_s \\ \bar{u}^2\delta_{zz} + N^2\delta_s + N_w^2(\delta - \delta_s) &= 0 \qquad \delta > \delta_s \end{aligned} \tag{2.9}$$

where the mean windspeed $\bar{u}$ is constant with height. N_w is the moist brunt Vaisala frequency, defined by Fraser et al. as

$$N_w^2 = gb(\ln\theta_E)_z \ . \tag{2.10}$$

θ_E is the equivalent potential temperature and b is a constant along a streamline. This equation is linear inside and outside of the cloud boundaries. However, the boundaries are not known apriori since they are determined by the flow. BJD present an iterative numerical technique in which the flow is adjusted until the cloud boundaries, streamlines, and mountain profile are approximately selfconsistent. The treament of condensation in BJD is similar to that used by Lilly (1960) to study conditional instability, except that the switch between dry and saturated stability is parameterized as a function of streamline displacement by BJD and vertical velocity by Lilly.

BJD examine the flow across a broad Witch of Agnesi mountain for the case where N, N_w and $\bar{u}$ are constant with height. The dry solution, obtained by Queney, is shown in Fig. 2.2. BJD found that as the moisture content of the air increased the cloud boundaries shrank, indicating a reduction in the upward displacement of the streamlines. They noted that the mountain wave drag can be cut in half when the upstream flow at low levels is very warm and moist. These results suggest that the presence of moisture in a layer near the surface damps the wave response.

No precipitation is allowed in the previous formulation. In a later study Barcilon et al. (1980) denoted here as BJB, the effects of rain and snow are estimated by assuming that any water vapor which condenses falls out instantly as rain. In this case, the effects of latent heat release are totally irreversible. In other respects the approach in this second paper is similar to that just described,

except that they no longer use an iterative scheme to match the heating regions with the streamline displacements. Instead they assume that the influence of latent heating on the flow is small so that to a first approximation the cloud boundaries are determined from the dry solution. Since there is a net heating of the flow, the horizontal integrals used to obtain the streamline displacement, horizontal windspeed, temperature and pressure do not converge. Apparently, ignoring this, BJB evaluate them numerically, and conclude that the presence of moisture in a layer near the ground can slightly increase the mountain wave drag when rain is present.

These pioneering studies of moist mountain waves have produced interesting results for idealized cases. However, they involve a numerical approach which becomes cumbersome as the cloud boundaries become complex, or an analytic approach which presumes that moisture effects will be small and hence somewhat uninteresting. They do not include rain in a realistic manner, and they rely on steady state, linearized, hydrostatic equations. In particular, they do not apply to trapped waves. I am not aware of any work which examines the effects of moisture on trapped lee waves.

B. Trapped Waves

Trapped lee waves are usually produced by narrower ridges than their propagating counterparts. Wave activity is confined to the lower atmosphere, but can extend several wavelengths downstream from the mountains. The wave drag associated with trapped waves is rather small and confined to the lower troposphere. Laminar lenticular clouds and turbulent rotor clouds sometimes appear in the crests of

trapped waves. A train of lenticular clouds observed by Larsson (1954) in the lee of the Ovik Mountains in Sweden is shown in Fig. 2.7. Larsson found evidence of continued wave activity twelve wavelengths downstream from the mountain. Note the cap cloud over the mountain crest.

Scorer (1949) considered steady, linear mountain waves in an atmosphere in which k_s^2 (Eq. 2.2) had a two layer structure. Although k_s^2 was discontinuous, $\theta(\bar{z})$ and $u(\bar{z})$ were chosen so that they were continuous across the interface. He found that in order for resonant waves to occur k_s must decrease upwards in which case the wave energy is trapped at lower levels. The requirement that k_s decrease with height means that either the windspeed must increase upwards or the stability must decrease upwards. His calculated lee waves are reproduced in Fig. 2.8. A misapplication of the radiation boundary condition causes the troughs and crests in this figure to tilt downstream. This does not, however, invalidate the resonant wave analysis. Corby and Wallington (1956) have extended Scorer's work to provide an extensive discussion of the effects of changes in the two layer atmospheric structure and the mountain width on the resonant wave amplitude.

Vergeiner (1971) and Smith (1977) compared lee waves observed in the Colorado Rockies and the Appalachian Blue Ridge with steady linear resonant wave theory. In order to approximate the detailed structure in real atmospheric soundings they used multi-layer models with up to 15 layers. As shown in Fig. 2.9, Vergeiner was able to obtain good agreement between linear theory and steady observed lee waves. However, in order to obtain this agreement it was necessary to chose

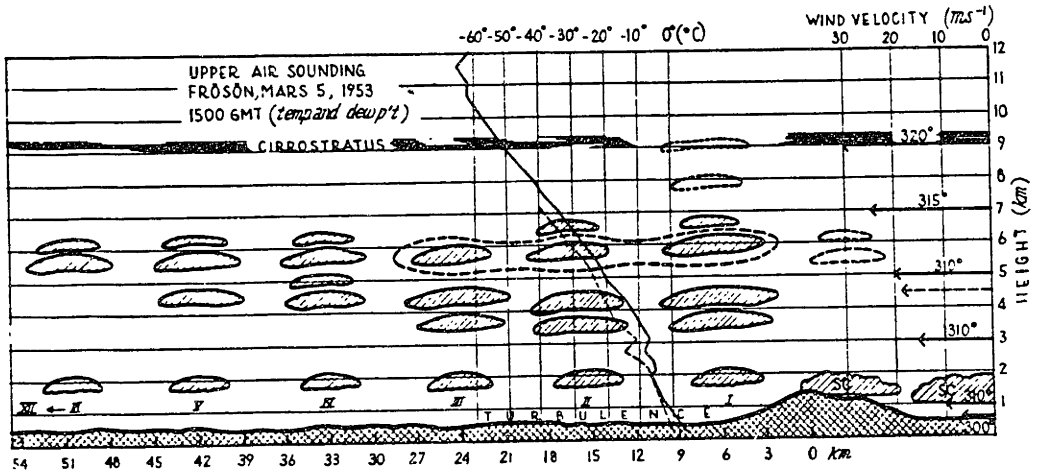

Figure 2.7. Cross-section of a train of wave clouds formed on the lee side of the Ovik Mountains, March 5, 1953. The cross-section is parallel to the average wind flow aloft. Wind data computed from upper level charts are shown to the right. From Larsson (1954).

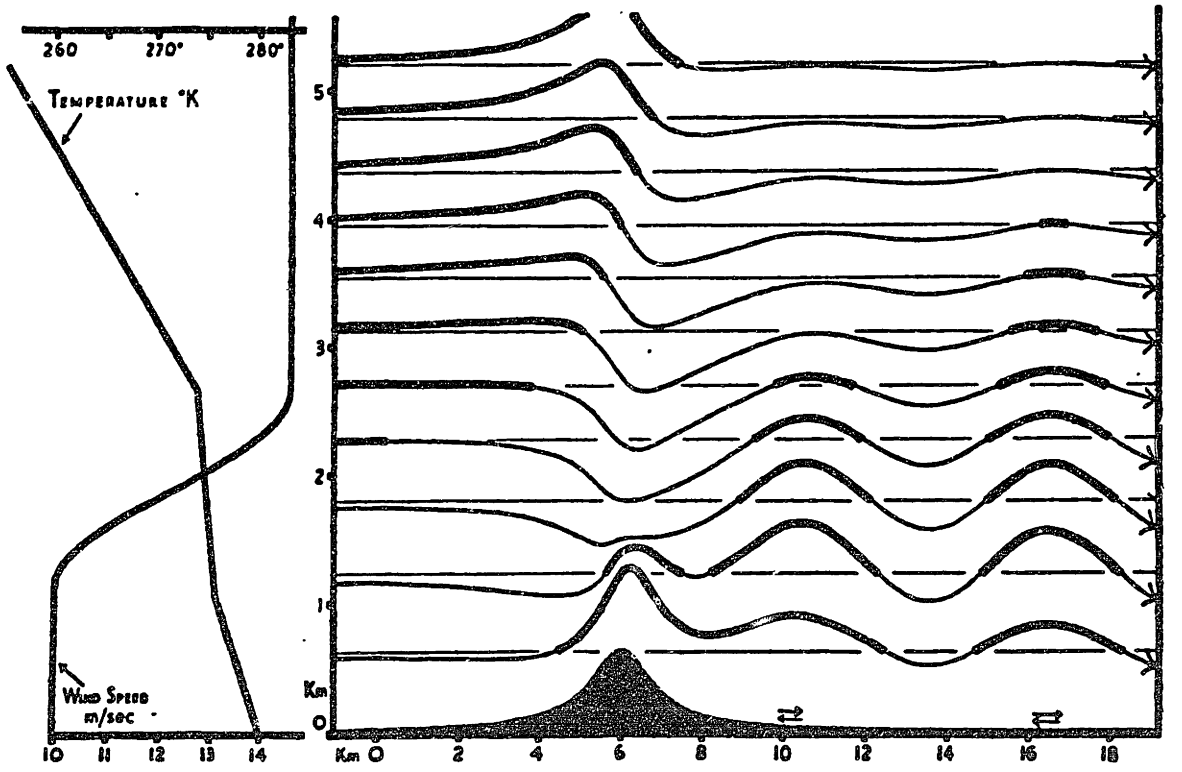

Figure 2.8. Airflow and upstream profiles in a two level model where k_s decreases upwards. From Scorer (1949).

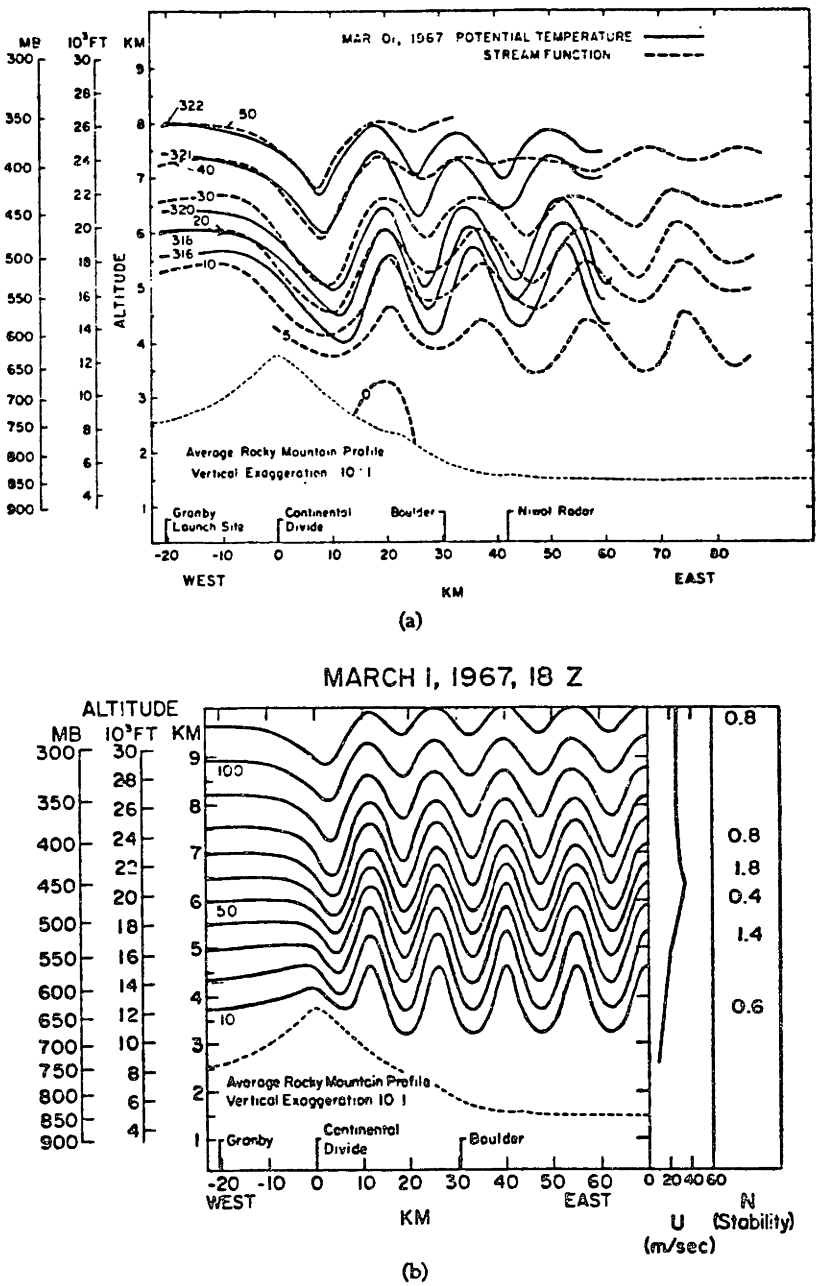

(a) Observed flow pattern for indicated date; (b) Computed flow pattern for same date

Figure 2.9. Observed and calculated flows for March 1, 1967. From Vergeiner (1971).

the mountain height and width in a rather ad hoc manner. Smith found that linear theory correctly estimated the wavelength but badly underestimated the wave amplitude in the observed waves.

In the remainder of this dissertation I will describe a nonhydrostatic, nonlinear numerical model designed to simulate the effects of moisture on mountain lee waves, and discuss the results of those simulations. Both the propagating and trapped wave cases will be discussed.

III. DESCRIPTION OF THE NUMERICAL MODEL

A. The Dynamical Framework

The computer model is designed to calculate the two-dimensional airflow over an infinitely long, uniform mountain barrier. The Coriolis force is neglected since only narrow mountains with widths much less than u/f (the mean wind speed divided by the Coriolis parameter) will be considered. There are several models in the literature that could be modified to simulate moist mountain waves in two dimensions. The model which will be described in this chapter is patterned very closely after the convective cloud model of Klemp and Wilhelmson (1978). Their model was selected as a basis for this work because it appeared to be at least as accurate and efficient as competing schemes, and it was readily available to the author. Three major modifications were made to the existing model; it was reduced from three to two dimensions; a terrain following coordinate system was introduced; and a wave absorbing layer was added to the top of the domain. Less significant changes were also made in the turbulent mixing parameterization, the small time step differencing and the lateral boundary conditions.

The basic continuity, thermodynamic and momentum equations in the Klemp-Wilhemson (KW) model may be written in two dimensions as follows:

$$\frac{du}{dt} + c_p \theta_M \frac{\partial \pi}{\partial x} = D_u \qquad (3.1)$$

$$\frac{dw}{dt} + c_p \theta_M \frac{\partial \pi}{\partial z} = g \frac{\theta_M - \bar{\theta}_M}{\bar{\theta}_M} + D_w \tag{3.2}$$

$$\frac{d\pi}{dt} + w\bar{\Pi}_z + \frac{R}{c_v}(\bar{\Pi}+\pi)\left(\frac{\partial u}{\partial x} + \frac{\partial w}{\partial z}\right) - \frac{R}{c_v}\frac{(\bar{\Pi}+\pi)}{\theta_v}\frac{d\theta_v}{dt} = 0 \tag{3.3}$$

$$\frac{d\phi}{dt} = M_\phi + D_\phi \tag{3.4}$$

where $\phi = \theta, q_v, q_c, q_r$ and

$$\theta_v = \theta (1 + .61\, q_v) \quad ,$$

$$\theta_M = \theta_v (1 - q_c - q_r) \quad , \qquad \frac{d}{dt} = \frac{\partial}{\partial t} + \frac{u\partial}{\partial x} + \frac{w\partial}{\partial z}$$

$$\bar{\Pi} + \pi = \left(\frac{p}{p_0}\right)^{R/c_p} = \left(\frac{R}{p_0}\rho\theta_M\right)^{R/c_v}, \quad \frac{\partial \bar{\Pi}}{\partial z} = \frac{-g}{c_p \bar{\theta}_M(z)} \tag{3.5}$$

In the above, p is the pressure, ρ is the total density, R is the gas constant for dry air, θ is the potential temperature, and u and w are the horizontal and vertical velocity components. The mixing ratios of water vapor, cloud water and rain water are q_v, q_c, and q_r, respectively. The terms D and M contain the contributions from turbulent mixing and microphysics. The microphysics terms are

$$M_\theta = \frac{L}{c_p \bar{\Pi}}\left(\Delta q_c - E_r\right) \tag{3.6}$$

$$M_{q_v} = -\Delta q_c + E_r \tag{3.7}$$

$$M_{q_c} = \Delta q_c - A_r - C_r \tag{3.8}$$

$$M_{q_r} = \frac{1}{\bar{\rho}} \frac{\partial}{\partial z} \left(\bar{\rho} V q_r\right) - E_r + A_r + C_r \tag{3.9}$$

Here L is the latent heat of vaporization; E_r is the evaporation of rain; A_r and C_r are the contributions of autoconversion and collection to raindrop development and growth. The term Δq_c is the rate of condensation or evaporation of rain water; V is the raindrop fall speed. The saturation mixing ratio, used to determine Δq_c, is calculated from Teten's formula

$$q_{vs} = \frac{3.8}{\bar{p}} \exp\left(17.27 \frac{\bar{\Pi}\theta - 273}{\bar{\Pi}\theta - 36}\right) \tag{3.10}$$

The autoconversion and collection rates are given by the Kessler parameterization which assumes that the spectrum of raindrop radius follows a Marshall-Palmer distribution

$$A_r = k_1(q_c - a)\ s^{-1} \tag{3.11}$$

$$C_r = k_2 q_c q_r^{0.875}\ s^{-1} \tag{3.12}$$

The autoconversion threshold and rate constants have nominal values of $a = 0.5$ gm/kg, $k_1 = .001\ s^{-1}$, $k_2 = 2.2\ s^{-1}$. The evaporation of raindrops is given by

$$E_r = \frac{1}{\bar{\rho}} \frac{(1 - q_v/q_{vs})\, C\, (\bar{\rho} q_r)^{0.525}}{5.4 \times 10^5 + 2.55 \times 10^6/(\bar{\rho} q_{vs})} \; s^{-1} \qquad (3.13)$$

where C is the ventilation factor

$$C = 1.6 + 124.9\, (\bar{\rho} q_r)^{0.2046} \qquad (3.14)$$

The raindrop fall speed is approximated as

$$V = 36.34\, (\bar{\rho} q_r)^{0.1346} \left(\frac{\bar{\rho}}{\rho_0}\right)^{-1/2} \; ms^{-1} \qquad (3.15)$$

In Eqs. (3.10) to (3.15), p is expressed in millibars, $\bar{\rho}$ in grams per cubic centimeter and q_v, q_c and q_r in grams per kilogram.

The microphysics terms do not include ice, since the extra computation required for its inclusion is not justified by its actual importance. Although snow and ice can be associated with mountain waves, in many cases of physical interest ice is not present. Even when freezing does occur, the dynamical forcing produced is small compared to that produced by condensation, since the latent heat of vaporization is an order of magnitude larger than the latent heat of fusion. Ice also influences the dynamics in more subtle, though minor, ways. In particular, ice crystals fall and evaporate at different rates than liquid droplets. Unfortunately, it is impossible to accurately capture such behavior without a vastly more complex microphysical model.

When modeling phenomena on the scale of mountain lee waves; it is impractical to use a computational mesh with sufficient resolution to explicitly represent every scale of motion which influences the waves. The effects of subgrid scale motions must be parameterized as a function of the larger scale flow. In the KW model, this is done by solving an additional prognostic equation for the subgrid scale kinetic energy, from which the eddy mixing coefficients are determined. While this approach is more sophisticated than a simple first order closure scheme, it is not primarily designed for two-dimensional calculations. In this two-dimensional model, sufficient accuracy is achieved with less numerical computation, by a conventional first order closure formulation which depends on the relative strengths of stratification and shear (Lilly, 1962). Subgrid scale effects are introduced to the velocity field calculations through the terms D_u and D_w

$$D_u = (K_M A)_x + (K_M B)_z \quad , \qquad D_w = (K_M B)_x - (K_M A)_z \tag{3.16}$$

where

$$A = (u_x - w_z) \quad , \qquad B = (u_z + w_x) \tag{3.17}$$

$$K_M = k^2 \Delta x \, \Delta z \, |Def| \, \left(\max \left(1 - \frac{K_H}{K_M} Ri, \, 0\right)\right)^{1/2} \tag{3.18}$$

and

$$Ri = \frac{N^2}{Def^2} \quad , \qquad Def^2 = A^2 + B^2 \tag{3.19}$$

$$N^2 = \begin{cases} g \dfrac{d\ell n\theta}{dz}, & \text{for } q_v < q_{vs} \\ g\left(1+1.61 \dfrac{\varepsilon L q_{vs}}{RT}\right)\left(1 + \dfrac{\varepsilon L^2 q_{vs}}{c_p RT^2}\right)^{-1} \dfrac{d\ln\theta_E}{dz}, & \text{for } q_v = q_{vs} \end{cases} \tag{3.20}$$

θ_E is the equivalent potential temperature, and $\varepsilon = .622$. The expression for the moist Brunt-Väisälä frequency is similar to that derived by Deardorff (1976). The subgrid scale mixing terms in the scalar equations ($\phi = \theta, q_v, q_c, q_r$) are

$$D_\phi = (K_H \phi_x)_x + (K_H \phi_z)_z \tag{3.21}$$

In the model $k = 0.21$ and $K_H/K_M = 3$ as suggested by Deardorff (1971, 1972). A value of $K_H/K_M = 3$ allows turbulent mixing to begin when Ri drops below 1/3, which is just slightly larger than the commonly accepted critical value for the stability of a shear flow, Ri = 1/4.

Terrain is incorporated in the model by a transformation of the vertical coordinate (Gal-Chen and Somerville, 1975)

$$\zeta = \frac{z_T (z - z_S)}{z_T - z_S} \tag{3.22}$$

where $z_S(x)$ is the terrain elevation and z_T is the height of the top of the modeling regions. Equations (3.1) to (3.4) may be written in transformed form as

$$u_t + uu_x + (Gu + Hw)u_\zeta + c_p\theta_M(\pi_x + G\pi_\zeta) = D_u \tag{3.23}$$

$$w_t + uw_x + (Gu + Hw)w_\zeta + c_p\theta_M H\pi_\zeta = g\frac{(\theta_M - \bar{\theta}_M)}{\bar{\theta}_M} + D_w \tag{3.24}$$

$$\pi_t + u\pi_x + (Gu + Hw)(\bar{\Pi} + \pi)_\zeta + \frac{R}{C_V}(\bar{\Pi} + \pi)(u_x + Gu_\zeta + Hw_\zeta)$$

$$-\frac{R}{c_v}\frac{(\bar{\Pi} + \pi)}{\theta_v}\frac{d\theta_v}{dt} = 0 \tag{3.25}$$

$$\phi_t + u\phi_x + (Gu + Hw)\phi_\zeta = D_\phi + M_\phi \tag{3.26}$$

where

$$G = \frac{\partial\zeta}{\partial x} = \frac{\zeta - z_T}{z_T - z_S}\frac{\partial z_S}{\partial x}$$
$$H = \frac{\partial\zeta}{\partial z} = \frac{z_T}{z_T - z_S} \tag{3.27}$$

B. The Numerical Model

The Eqs. (3.1) to (3.4) which govern the dynamics of mountain waves are compressible, and therefore include sound waves. While the sound waves are not meteorologically significant, they travel at high speeds and thus severly limit the time step in explicit numerical integrations. In order to remove this computational burden, many researchers have chosen the anelastic equations, which do not admit sound waves, as the basis for their models. However, the anelastic system requires the solution of a Poisson equation for the pressure at

each time step, which can be time consuming. The presence of a coordinate transformation makes the Poisson solution even less efficient because it complicates the coefficient structure in the pressure equation.

The KW model uses a technique for the solution of the full compressible equations in which the sound wave modes are integrated separately, with a smaller time step than that used for the other processes of meteorological interest. When a coordinate transformation is present, this technique seems to be more efficient than the conventional anelastic approach. Since it avoids the approximations used in deriving the anelastic system, while reducing the computational burden, the two time step technique is retained in this model.

1. Grid structure

The model uses the standard staggered mesh shown in Fig. 3.1. Thermodynamic and moisture variables are all represented at a common grid point; velocity variables are displaced half a grid interval from that point. This arrangement improves the resolution in the pressure gradient and divergence terms without requiring a reduction in the large time step.

2. Small time step calculations

Although all the terms in Eqs. (3.1) to (3.4) have some influence on the sound waves, only the pressure gradient terms in the momentum equations and divergence terms in the pressure equation are responsible for rapid sound wave propagation. It is useful to linearize these terms and rewrite Eqs. (3.1) to (3.3) as

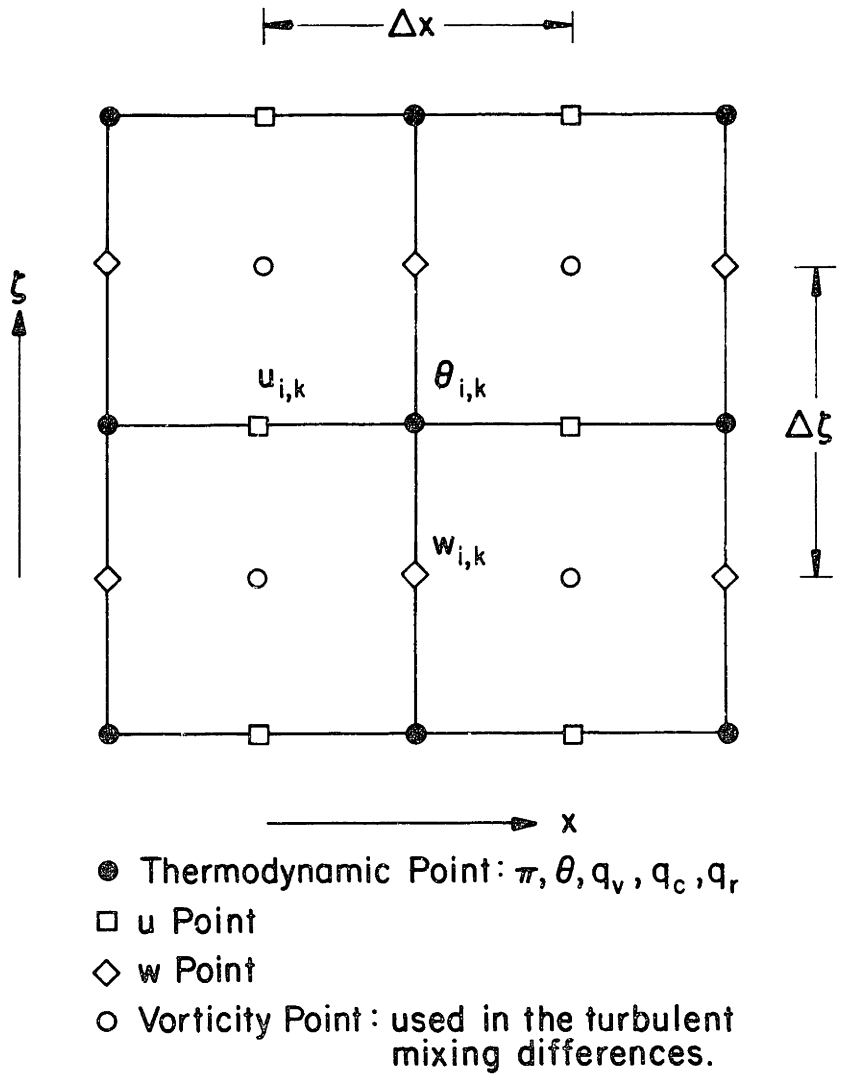

Figure 3.1. The numerical grid structure.

$$u_t + c_p \bar{\theta}_M \pi_x = f_u$$

$$w_t + c_p \bar{\theta}_M \pi_z = f_w \qquad (3.28)$$

$$\pi_t + \frac{\bar{c}^2}{c_p \bar{\rho}\bar{\theta}^2_M} \left(\bar{\rho}\bar{\theta}_M u_x + (\bar{\rho}\bar{\theta}_M w)_z \right) = f_\pi$$

where

$$\bar{c}^2 = c_p R \bar{\Pi} \bar{\theta}_M / c_v \ ,$$

and the remainder of the equation (including the nonlinear part of the divergence and pressure gradient terms) is collected in f_u, f_w and f_π. Now, the only terms which require a small time step for numerical integration are on the left-hand side. The right-hand side is updated on a large time step, Δt; it is held fixed over several small time steps, $\Delta\tau$, during which the left-hand side is integrated in a stable manner. The small time step stability requirement (Courant-Friedrichs-Lewy condition) is $\bar{c}\,\Delta\tau/(\Delta x^2 + \Delta z^2)^{1/2} < 1$. In mountain wave modeling, Δx is typically much larger than Δz, so extra efficiency can be achieved by making the small time step implicit in the vertical. The finite difference representation of the small time step equations, with the coordinate transformation included, is

$$\delta_\tau u + c_p \bar{\theta}_M \left(\delta_x \pi^\tau + G \delta_{2\zeta} \overline{\pi^\tau}^x \right) = f_u^t \qquad (3.29)$$

$$\delta_\tau \tilde{w} + C_p \bar{\bar{\rho}} \bar{\theta}_M^2 \, H\langle \delta_\zeta \pi \rangle_\tau = \bar{\bar{\rho}} \bar{\theta}_M f_w^t \tag{3.30}$$

$$\delta_\tau \pi + \frac{\bar{c}^2}{c_p \bar{\theta}_M} \left(\delta_x u^{\tau+1} + \overline{G\delta_2 \zeta u^{\tau+1}}^x \right) + \frac{\bar{c}^2}{c_p \bar{\bar{\rho}} \bar{\bar{\theta}}_M^2} H\langle \delta_\zeta \tilde{w} \rangle_\tau = f_\pi^t \tag{3.31}$$

where for any independent variable ζ, the finite difference operators are defined:

$$\delta_{n\xi} \phi(\xi) = (1/n\Delta\xi) \left[\phi(\xi + n\Delta\xi/2) - \phi(\xi - n\Delta\xi/2) \right] \tag{3.32}$$

$$\overline{\phi(\xi)}^{n\xi} = \frac{1}{2} \phi(\xi + n\Delta\xi) + \phi(\xi - n\Delta\xi) \tag{3.33}$$

$$\langle \phi(\zeta) \rangle_\tau = \frac{1 + \varepsilon}{2} \phi(\tau + \Delta\tau) + \frac{1 - \varepsilon}{2} \phi(\tau) \tag{3.34}$$

and $\tilde{w} = \bar{\bar{\rho}} \bar{\theta}_M w$. Only those vertical differences which remain in the limit of flat terrain are treated implicitly.

In the original KW model the parameter ε is zero in which case the time differencing is Crank-Nicolson which is unconditionally stable. However, this alone is not adequate to insure the stability of the entire big step small-step integration cycle. A weak instability was encountered in the sound wave modes while simulating mountain waves in deep, very stable environments. This was eliminated by adjusting ε. When $0 < \varepsilon \leq 1$ the scheme is unconditionally stable, and in addition it slowly damps the sound wave modes. Tests were run comparing the effects of different values of ε on the mountain wave solutions. A value of $\varepsilon = 0.2$ was sufficient to completely eliminate the sound wave instability without perceptibly influencing the gravity

waves. The gravity waves are not affected because they change very slowly over a single small time step. In this study $\varepsilon = 0.2$.

It should be emphasized that the purpose of the two time step technique is to treat the sound wave modes in a stable manner. Efficiency in the small time step calculations is achieved at the expense of accuracy in the sound wave modes themselves, but, since the sound waves are not meteorologically significant, they need not be accurately integrated. The gravity wave modes are still accurately computed.

3. Large time step calculations

The differencing on the large time step is leap-frog, which provides second order accuracy and avoids computational damping. The vertical advection, pressure gradient and divergence terms are all second order differences. Phase errors in advection terms are a major source of error in numerical integrations. In general, the phase error experienced by a wave of given physical dimensions can be reduced by either reducing the grid size or using a higher order difference scheme. Since, in mountain wave problems, there are often more grid points per wavelength in the vertical than in the horizontal, the overall accuracy of the model can be improved with little extra computation by using a fourth order scheme for horizontal advection. This is especially appropriate in linear and mildly nonlinear mountain wave problems, since then all the strong advection is in the horizontal. Therefore, centered fourth order differences are used for all horizontal advection terms except the one in the π equation. Second order differences are used for $u\pi_x$

because the changes in π are dominated by sound wave propagation, not horizontal advection.

The right-hand sides of the momentum and continuity equations, with the coordinate transformation included are

$$f_u = \frac{-u}{3}\left(4\delta_{2x}u - \delta_{4x}u\right) - \overline{\left(\bar{u}^{\zeta}G + H\bar{w}^{x}\right)\delta_{\zeta}u}^{\zeta}$$

$$-c_p\left(\bar{\theta}_M^{x} - \overline{\theta_{M_0}}^{x}\right)\left(\delta_x\pi + \overline{G\delta_{2\zeta}\pi}^{x}\right) + D_u \tag{3.35}$$

$$f_w = \frac{\overline{-u}^{\zeta x}}{3}\left(4\delta_{2x}w - \delta_{4x}w\right) - \left(\overline{\bar{u}^{x}}^{\zeta}G + Hw\right)\delta_{2\zeta}w$$

$$+ \left(\bar{\theta}_M^{\zeta} - \bar{\theta}_{M_0}^{\zeta}\right)\left(\frac{g}{\bar{\theta}_{M_0}^{\zeta}} - c_pH\delta_{\zeta}\pi\right) + D_w \tag{3.36}$$

$$f_\pi = \overline{-u\delta_x\pi}^{x} - \overline{\left(\bar{u}^{x}G + Hw\right)\delta_{\zeta}\pi}^{\zeta} - \frac{R}{c_p}\pi\left(\delta_x u + \overline{G\delta_{2\zeta}u}^{x} + H\delta_{\zeta}w\right)$$

$$+ \frac{\bar{c}^2}{c_p\theta_{v_0}}\left(\frac{M_\theta + D_\theta}{\theta} + \frac{.61\left(M_{q_v} + D_{q_v}\right)}{1 + .61q_v}\right) \tag{3.37}$$

and θ_{M_0} is the mean θ_M along a constant z surface (denoted $\bar{\theta}_M$ in earlier equations). Since the operator $\overline{(\;)}^{x}$ averages along a constant ζ surface, $\overline{\theta_{M_0}}^{x} \neq \theta_{M_0}$. In practice, the terms in Eqs. (3.34) and (3.35) involving the pressure gradient, and the entire f_π expression may be omitted with only minor effect on the solution; in fact, they are omitted in the original three-dimensional KW model. They are included in this model since the computational cost is not prohibi-

tive, and their inclusion makes the finite difference equations formally equivalent to the full Navier-Stokes equations.

The scalar advection equations are all differenced identically

$$\delta_{2t}\phi = \frac{-\bar{u}^{x}}{3}\left(4\delta_{2x}\phi - \delta_{4x}\phi\right) - \left(\overline{\bar{u}^{x}}^{\zeta} G + Hw\right)\delta_{\zeta}\phi + M_{\phi} + D_{\phi} \qquad (3.38)$$

The small and large time steps are meshed as follows. The scalar equations for θ, q_v, q_c and q_r are stepped from $t - \Delta t$ to $t + \Delta t$ by a single leap-frog step. The functions f_u, f_w and f_π are evaluated at the central time level t. Finally, the u, w, and π fields are stepped forward from $t - \Delta t$ to $t + \Delta t$ with forward time differencing on the small time step. The total number of small time steps is $2\Delta t/\Delta\tau$.

4. Microphysical calculations

In the KW model, the microphysics are included through a two step procedure suggested by Soong and Ogura (1973). In the first step, the microphysical variables are advected and diffused with the terms M_ϕ ignored in Eqs. (3.26). Then, in the second step, the temperature and moisture fields are adjusted to include microphysical processes. The rain water flux convergence is calculated

$$\frac{\partial}{\partial\zeta}\left(\bar{\rho}\bar{V}q_r\right) = H\delta_{2\zeta}\left(\bar{\rho}\bar{V}q_r\right) \qquad (3\text{-}39)$$

At the lowest grid level, a one sided difference is used; in order to maintain linear stability, it is lagged in time at $t - \Delta t$.

Autoconversion, collection and the evaporation of rainwater are calculated as per Eqs. (3.11) to (3.15). The evaporation of rain is limited by the amount of additional water vapor required to saturate the air. Let the values of θ, q_v and q_c at this point in the calculation be denoted by an asterisk.

In order to complete the evaluation of M_ϕ, we must determine the amount of cloud, Δq_c, which must be condensed or evaporated in order to bring θ and q_v into equilibrium with $q_v^{t+\Delta t} = q_{vs}^{t+\Delta t}$. Of course if the air is unsaturated, Δq_c will be limited by q_c^*. We require the adjustment to proceed moist adiabatically so that

$$\theta^{t+\Delta t} + \frac{L}{c_p \bar{\Pi}} q_v^{t+\Delta t} = \theta^* + \frac{L}{c_p \bar{\Pi}} q_v^* \tag{3.40}$$

Teten's formula for the saturation mixing ratio (Eq. (3.10)) may be lineaized about θ^* to obtain

$$q_{vs}^{t+\Delta t} = q_{vs}^* \left[1 + \frac{4093\ \bar{\Pi}}{(\bar{\Pi}\theta^* - 36)^2} \left(\theta^{t+\Delta t} - \theta^* \right) \right] \tag{3.41}$$

Eqs. (3.40) and (3.41) can be combined to obtain the desired expression for Δq_c,

$$\Delta q_c = \max \left(\frac{q_v^* - q_{vs}^*}{1 + q_{vs}^* \dfrac{4093\ L}{c_p (\bar{\Pi}\theta^* - 36)^2}} , - q_c^* \right) \tag{3.42}$$

The evaluation of M_ϕ is completed according to Eqs. (3.6) to (3.9).

5. Subgrid scale mixing calculations

The presence of the terrain transformation makes the evaluation of horizontal second derivatives in the subgrid scale mixing terms rather cumbersome. The finite differences are computed as follows:

$$A_1 = \delta_x u + G\overline{\delta_{2\zeta} u}^{x} - H\delta_\zeta w$$

$$A_2 = \overline{\delta_{2x} u}^{\zeta} + G\delta_\zeta u - H\overline{\delta_{2\zeta} w}^{x} \tag{3.43}$$

$$B_1 = H\overline{\delta_{2\zeta} u}^{x} + \overline{\delta_{2x} w}^{\zeta} + G\delta_\zeta w$$

$$B_2 = H\delta_\zeta u + \delta_x w + G\overline{\delta_{2\zeta} w}^{x} \tag{3.44}$$

The terms with subscript 1 are evaluated at thermodynamic points; those with subscript 2 are calculated at vorticity points. Continuing, we calculate

$$Def_1^2 = A_1^2 + B_1^2 , \qquad Def_2^2 = A_2^2 + B_2^2 \tag{3.45}$$

$$Ri_1 = \begin{cases} \dfrac{\alpha g H \delta_{2\zeta}\left(\theta + \dfrac{L}{c_p \bar{\Pi}} q_v\right)}{\left(\theta + \dfrac{L}{c_p \bar{\Pi}} q_v\right)(Def_1)^2} , & \text{when } q_c(\zeta-\Delta\zeta) \times q_c(\zeta) \times q_c(\zeta+\Delta\zeta) > 0 \\ \dfrac{g H \delta_{2\zeta}\theta}{\theta (Def_1)^2} , & \text{otherwise} \end{cases} \tag{3.46}$$

$$Ri_2 = \begin{cases} \dfrac{\alpha g H \overline{\delta_\zeta \left(\theta + \dfrac{L}{c_p \bar{\Pi}} q_v\right)}^x}{\overline{\overline{\left(\theta + \dfrac{L}{c_p \bar{\Pi}} q_v\right)}^x}^\zeta \; (Def_2)^2} & \text{when } q_c(\zeta-\Delta\zeta/2) \times q_c(\zeta+\Delta\zeta/2) \\ & \times q_c(x-\Delta x/2) \times q_c(x+\Delta x/2) > 0 \\ \dfrac{g H \overline{\delta_\zeta \theta}^x}{\overline{\bar{\theta}^x}^\zeta \; (Def_2)^2}, & \text{otherwise} \end{cases} \tag{3.47}$$

$$\alpha(z) = \left(1 + 1.61 \frac{\varepsilon L \bar{q}_{vs}}{R \bar{\Pi} \bar{\theta}}\right)\left(1 + \frac{\varepsilon L^2 \bar{q}_{vs}}{c_p R (\bar{\Pi}\bar{\theta})^2}\right)^{-1} \tag{3.48}$$

$$\begin{aligned} K_{M_1} &= k^2 \Delta x \; \Delta\zeta \; Def_1 \left(\max(0,\, 1-3Ri_1)\right)^{1/2} \\ K_{M_2} &= k^2 \Delta x \; \Delta\zeta \; Def_2 \left(\max(0,\, 1-3Ri_2)\right)^{1/2} \end{aligned} \tag{3.49}$$

and finally,

$$D_u = \delta_x(K_{M_1} A_1) + G\delta_\zeta(K_{M_2} A_2) - H\delta_\zeta(K_{M_2} B_2) \tag{3.50}$$

$$D_w = \delta_x(K_{M_2} B_2) + G\delta_\zeta(K_{M_1} B_1) - H\delta_\zeta(K_{M_1} A_1) \tag{3.51}$$

The mixing terms for ılar variables are derived from K_{M_1}

$$K_H = 3K_{M_1} \tag{3.52}$$

let

$$R = \overline{K_H}^{x} \left(\delta_x \phi + G\overline{\delta_{2\zeta}\phi}^{x}\right)$$

$$S = \overline{K_H}^{\zeta} \left(\overline{\delta_{2x}\phi}^{\zeta} + G\delta_\zeta \phi\right) \qquad (3.53)$$

$$T = \overline{K_H}^{\zeta} \delta_\zeta \phi$$

then

$$D_\phi = \delta_x R + G\delta_\zeta S + H^2 \delta_\zeta T \qquad (3.54)$$

6. Boundary conditions

The ground is the only physical boundary associated with the mountain wave problem. We require the normal velocity to vanish at the surface

$$w = u \frac{\partial z_s}{\partial x} \quad \text{at } \zeta = 0 \qquad (3.55)$$

As a result $Gu + Hw = 0$ at $\zeta = 0$, so the vertical flux terms in Eqs. (3.34) to (3.38) vanish at the lower boundary. The subgrid scale mixing term also requires a boundary condition at the surface. Mixing normal to the boundary is assumed to vanish at the boundary point. This condition prevents the mean state vertical gradients from being distorted by mixing near the ground.

The radiation boundary condition, which requires that all energy transport be directed out of the domain, is approximated at the upper boundary. This condition is crucial for the successful simulation of

vertically propagating mountain waves. There are, however, physical situations in which downward propagating waves reflect from sharp gradients in the atmospheric structure or regions of wave overturning and breakdown, and have a significant impact on the wave dynamics below. In such instances the correct solution can be obtained only by applying this boundary condition above the reflecting layers.

The radiation boundary condition requires that waves which propagate upward through the computational domain experience no spurious reflection into a downward propagating mode when they encounter the upper boundary. This requirement can be essentially satisfied by adding an absorbing layer to the top of the model. The boundary condition at the top of the absorbing layer is $w = 0$, which is clearly reflective; however, waves entering the layer from below are artifically damped by the absorber so that they have negligible amplitude when they reach the upper boundary. Reflections from the top boundary can thus be virtually eliminated. It is still possible to produce reflections from the bottom or interior of the absorbing layer due to the changes in wave propagation characteristics produced by vertical variations in the artificial damping. These reflections can be minimized by ensuring that the strength of the damping increases very gradually as a function of height. However, if the damping does increase very gradually, the layer must be quite thick, or waves which reach the top will still have sufficient amplitude to create troublesome reflections. From the standpoint of computational efficiency, the absorbing layer should be as thin as possible, so a compromise must be found between efficiency and accuracy.

Klemp and Lilly (1978) have suggested that, for hydrostatic waves, a minimum depth of one vertical wavelength is necessary for a reliable wave absorber. In mountain wave problems, this may require that as much as one-half of the computational grid be devoted to the absorbing layer. Both viscous and Rayleigh damping have been used in absorbing layers (Clark, 1977; Klemp and Lilly, 1978). Rayleigh damping has been chosen for this model because the second derivatives required for viscous damping have a complicated finite difference structure in the presence of the coordinate transformation. In the absorbing layer, only the perturbations of a variable from its upstream value are damped. The damping terms, which are added to the right-hand sides of the u, w and θ equations, are

$$\begin{aligned} R_u &= \tau(z)(u - \bar{u}) \\ R_w &= \tau(z)w \\ R_\theta &= \tau(z)(\theta - \bar{\theta}) \end{aligned} \tag{3.55}$$

The damping coefficient has the structure

$$\tau(z) = \begin{cases} 0 , & \text{for } z \leq z_D \\ -\frac{\alpha}{2}\left(1 - \cos\frac{z - z_D}{z_T - z_D}\pi\right) , & \text{for } 0 \leq \frac{z - z_D}{z_T - z_D} \leq 1/2 \\ -\frac{\alpha}{2}\left(1 + \left(\frac{z - z_D}{z_T - z_D} - \frac{1}{2}\right)\pi\right) , & \text{for } \frac{1}{2} \leq \frac{z - z_D}{z_T - z_D} \leq 1 \end{cases} \tag{3.56}$$

where z_D is the height of the bottom of the absorbing layer and (in this instance only) π is 3.1416. Klemp and Lilly (1978) have shown that for a single, linear hydrostatic wave, the absorbing layer will be most effective when α satisfies

$$2 \leq \alpha/k\bar{u} \leq 5 \tag{3.57}$$

where k is the horizontal wave number. In actual simulations, α is chosen so that the dominant horizontal wave numbers satisfy Eq. (3.57).

The finite difference formulation requires lateral boundary conditions at the edges of the numerical domain; unfortunately, no horizontal boundaries are actually associated with the physical problem. As a result, the imposed numerical boundary conditions are completely artificial; their sole design is to make the termination of the finite mesh as innocuous as possible. The lateral boundary conditions specified in this model are similar to the wave permiable boundary conditions proposed by Orlanski (1976). In the following we will consider, without loss of generality, only situations in which the mean horizontal windspeed, u, is positive. In the original Orlanski procedure the phase speed, c, of a gravity wave impinging on the boundary is estimated; then the flow variables are advected out the downstream (upstream) boundary at a speed u+c (u-c). This will allow the gravity wave to pass through the boundary with minimal reflection.

A one-dimensional wave of uniform amplitude traveling horizontally downstream will satisfy

$$u_t + (u + c)\, u_x = 0 \tag{3.58}$$

the speed of propagation, u+c, is thus $-u_t/u_x$. Orlanski's original approach was to estimate the propagation speed as

$$u+c^* = \frac{\Delta x}{\Delta t} \frac{u_{b-1}^{t} - u_{b-1}^{t-1}}{u_{b-1}^{t-1} - u_{b-2}^{t-1}} \tag{3.59}$$

where b is the index of the downstream boundary point. Then u_b^{t+1} may be estimated by upstream differencing as

$$u_b^{t+1} - u_b^t = (u+c^*) \frac{\Delta t}{\Delta x} \left(u_b^t - u_{b-1}^t\right) \tag{3.60}$$

In this scheme $u+c^*$ is computed separately at each vertical level along the lateral boundaries. In practice, this leads to large variations in the propagation speeds calculated at adjacent boundary points. In reality, the waves impinging on the boundary are not one-dimensional, but have a vertical structure with some vertical coherence, so Klemp and Lilly (1978) computed a vertical average of $u+c^*$ and used this estimate at each point along the boundary. In the KW model, which was modified to create this model, c^* is specified externally to correspond to the faster gravity waves propagating through the domain. This latter approach has the disadvantage that $u+c^*$ will not approach zero if the flow approaches steady state. In the KW model, this boundary condition is applied

only to the equation for the horizontal velocity, whereas it is applied to all the variables in the original Orlanski scheme.

The different boundary condition options were tested in this new model in two ways. In the first type of test the model was compared against linear analytic solutions. In the second type of test, the model was compared against a "good" nonlinear solution obtained by moving the lateral boundaries far upstream and downstream. The boundary condition which performed best in these empirical tests is essentially a modification of the Klemp and Lilly (1978) formula. As in the KW model, it is applied only to the horizontal velocity field. The estimated propagation speed is averaged in the vertical, and weighted at each level by the approximate local strength of the wave, u_x. The calculations are arbitrarily moved five points in from the boundary to reduce the feedback of boundary condition errors on the phase speed calculations. Then $u+c^*$ is given by

$$u+c^* = \frac{\Delta x}{\Delta t} \frac{\sum_{k=1}^{N} \left(u_{b-4}^{t} - u_{b-4}^{t-1}\right) \operatorname{sgn}\left(u_{b-4}^{t-1} - u_{b-5}^{t-1}\right)}{\sum_{k=1}^{N} \left| u_{b-4}^{t-1} - u_{b-5}^{t-1} \right|} . \qquad (3.61)$$

Negative phase speeds are set to zero at the downstream boundary, since the finite difference form (3.60) is unstable for $u+c^* < 0$. A similar procedure is employed at the upstream boundary. Clearly, the details of the phase speed calculations are rather ad hoc. The model is not very sensitive to small changes in this calculation; the formulation given seems to be slightly superior to the others tested.

Boundary conditions are applied to the horizontal advection terms in the other prognostic equations as follows. At outflow boundaries, the centered differences are replaced by one-sided upstream differences. At inflow boundaries, horizontal gradients in the w, θ, π and q_r fields are set to zero. The equations for q_v and q_c are replaced by the requirements that $q_v + q_c$ remain fixed at inflow. Since the fourth order finite differences also require a boundary condition at grid points one column inside the right and left boundaries, second order differences are used at these locations. Finally, in specifying boundary conditions for the subgrid scale mixing terms, it is assumed that no mixing normal to the boundary occurs at a boundary point.

7. Initialization

The model is initialized by slowly increasing the wind speed everywhere, from zero to its value in the mean upstream profile, over a nondimensional time $t = 4a/u$, where a is the mountain half width. The gradual start-up reduces the transients generated during initialization.

8. Numerical smoothing

A small amount of numerical smoothing is applied to all fields, throughout the domain, to control the growth of nonlinear instability and filter out short wavelength modes, whose behavior cannot be accurately represented by finite difference schemes. The smoother is equivalent to a fourth order damper. Its numerical form is

$$\gamma(\phi_{i+2} + \phi_{i-2} - 4(\phi_{i+1} + \phi_{i-1}) + 6\phi_i) \qquad (3.62)$$

γ has a nominal value of .015 in the horizontal and .001 in the vertical. In the absorbing layer γ gradually increases with height to .0625 in the horizontal, the value at which $2\Delta x$ waves are completely removed each time step. The horizontal smoothing coefficient is increased in the wave absorbing layer to improve the short wavelength absorption because Rayleigh damping attenuates short wavelengths less efficiently than long wavelengths. A second order smoother is used at grid points adjacent to the boundaries with a coefficient that matches the interior smoothing for $2\Delta x$ scale disturbances. No smoothing is performed at boundary points. The smoother is applied only to the perturbations of the variables from their values in the undisturbed upstream flow.

The damping characteristics of this smoother are listed as a function of wavenumber in Table 3.1. Note that the vertical damping coefficient is so small that its influence is largely restricted to $2\Delta z$ waves. The horizontal smoother has a strong impact on waves as long as $5\Delta x$ in the computational domain, and $8\Delta x$ near the top of the damping layer. In order to put these figures in perspective, note that in a typical propagating wave simulation the strongest mountain wave forcing is near $30\Delta x$ and the waves propagate approximately 2/3 of a vertical wavelength in 100 time steps. The impact of this smoother on the calculated flow fields and momentum flux was evaluated in linear and weakly nonlinear cases (for which no numerical smoothing is needed) by performing identical simulations with and without smoothing, and comparing the solutions. The differences were negligible. Even in the momentum flux, which is a second order quantity, they were confined to the third decimal place.

Table 3.1.

The remaining amplitude, after 100 applications of the fourth order smoother to a wave of unit amplitude, for several wavelengths and smoothing coefficients.

	$\gamma = .001$	$\gamma = .015$	$\gamma = .0625$
$2\Delta x$	.20	0.0	0.0
$4\Delta x$	.67	.002	0.0
$8\Delta x$	.97	.60	.11
$16\Delta x$	.998	.97	.87

Leap-frog time differencing allows the solutions at odd and even time steps to gradually diverge. This is prevented by the following time smoothing scheme.

$$\phi_*^{t+\Delta t} = \phi^{t-\Delta t} + 2\Delta t\ F_*^t$$

$$\phi^t = \phi_*^t + \eta(\phi_*^{t+\Delta t} - 2\phi_*^t + \phi^{t-\Delta t}) \tag{3.63}$$

Terms which have not yet been time smoothed are denoted by an asterisk; η is 0.2. The first equation represents a standard leap-frog step; the second, the time smoothing. This technique has been analyzed by Asselin (1972) who found that it strongly damped the computational mode without significantly impacting the physical mode. The smoothing, applied at every time step, has a gentler impact on the solution than schemes which rely on the use of a strong filter or an Euler time step, once in a cycle with a large number of unsmoothed steps.

9. Momentum flux calculations

The vertical flux of horizontal momentum is an important diagnostic quantity in mountain wave studies. The horizontal integral

$$M(z) = \int_{-\infty}^{\infty} \bar{\rho} u' w' dx \tag{3.64}$$

is approximated as follows. The velocity components u and w are linearly interpolated from constant ζ to constant z surfaces at the heights of the upstream u and w grid points. Then

$$M_k \approx \sum_{i=1}^{N_x} \frac{\bar{\rho}_k}{4} \left(u_{i+1,k} + u_{i,k} - 2\bar{u}_k\right)\left(w_{i,k+1} + w_{i,k}\right) \Delta x \quad . \quad (3.65)$$

This calculation is not performed at grid levels below the height of the mountain peak, because the path of horizontal integration would intersect the terrain.

IV. SIMPLE TESTS OF THE NUMERICAL MODEL

The numerical model described in Chapter III is very complex. In this chapter we will examine its performance in simple situations designed primarily to test the model. In later chapters there will be more comparisons between model calculations and analytic theory.

A. Dry Linear Hydrostatic Solution

If the atmosphere is isothermal and the mean wind is constant with height, then the Scorer parameter is a constant

$$k_s^2 = \frac{g^2}{c_p \bar{T} \bar{u}^2} - \frac{g^2}{4R^2 T^2} \quad . \tag{4.1}$$

If in addition the flow is hydrostatic, the $\tilde{w}_{xx}$ term in Eq. (2.1) is small, and the mountain wave solution is particularly simple. The streamline displacements produced by a Witch of Agnesi mountain (Eq. 2.6) satisfy

$$\delta(x,z) = \left(\frac{\bar{\rho}}{\rho_0}\right)^{-1/2} ha \, \frac{a \cos k_s z - x \sin k_s z}{x^2 + a^2} \quad . \tag{4.2}$$

The velocity components may be obtained from the relations

$$w = \bar{u}\delta_x \quad , \qquad u' = \frac{-\bar{u}}{\bar{\rho}} (\bar{\rho}\delta)_z \quad . \tag{4.3}$$

The streamlines and perturbation u and w fields calculated from Eqs. (4.2) and (4.3), for the case T = 250°K, $\bar{u}$ = 20 m/s, a = 10 km, h = 1 m, are displayed in Figs. 4.1a, 4.2a and 4.3a. The corresponding fields obtained with the numerical model are shown in Figs. 4.1b, 4.2b and 4.3b. In this run, the computational domain contains 80 points in the horizontal and 64 levels in the vertical; the absorbing layer occupies the top 32 levels. The grid intervals are Δx = 2 km, Δz = 250 m; the large and small time steps are 20 seconds and 4 seconds, respectively. Figures 4.1 to 4.6 show only the central portion of the domain, in which the grid indices run from 20 to 60 in the horizontal, and 1 to 32 in the vertical. The mountain is centered in the domain.

Although the model is neither linear nor hydrostatic, the influence of the nonlinear and nonhydrostatic terms should be almost negligible for a 1 m high, 10 km wide mountain. As an example, consider the impact of nonhydrostatic effects on the momentum flux. Klemp and Lilly (1980) have shown that in a flow such as this, where $Na/\bar{u}$ = 10, the linear hydrostatic momentum flux is 98% of the full nonhydrostatic value.

Examination of Figs. 4.1 through 4.3 shows that the model reproduces the linear solution rather well. The worst discrepancies appear in the u' field far upstream from the mountain where the magnitude of u' is small. This error is somewhat sensitive to the location of the upstream boundary. Tests have been performed to assess the sensitivity of this, and other solutions to the locations of the lateral boundaries. It was determined that a satisfactory

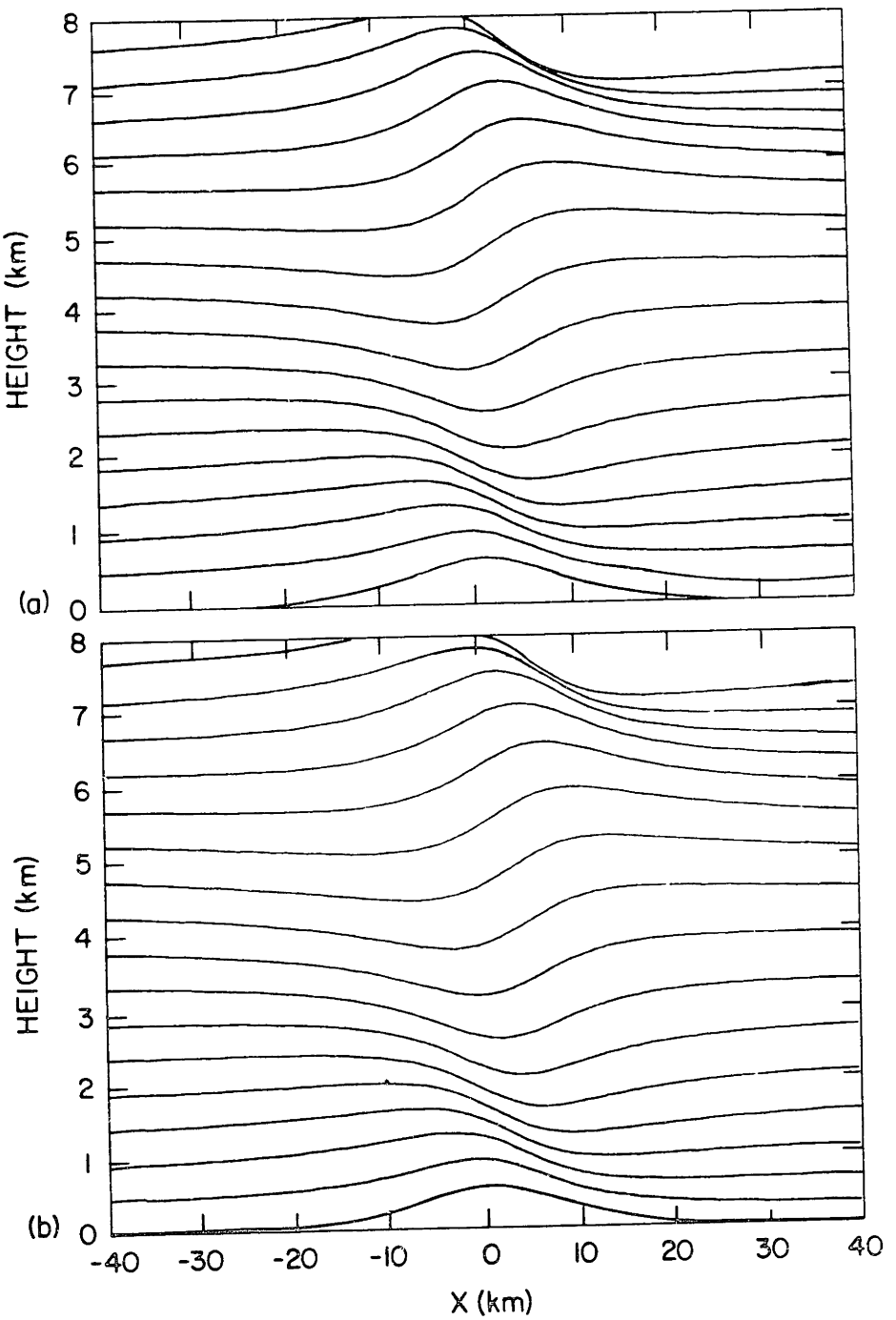

Figure 4.1. (a) Steady state streamlines from the linear hydrostatic analytic solution for a 600 m high mountain. (b) Streamlines obtained by numerical simulation for a 1 m high mountain at ut/a=60. Perturbations are multiplied by 600 to normalize the wave amplitude.

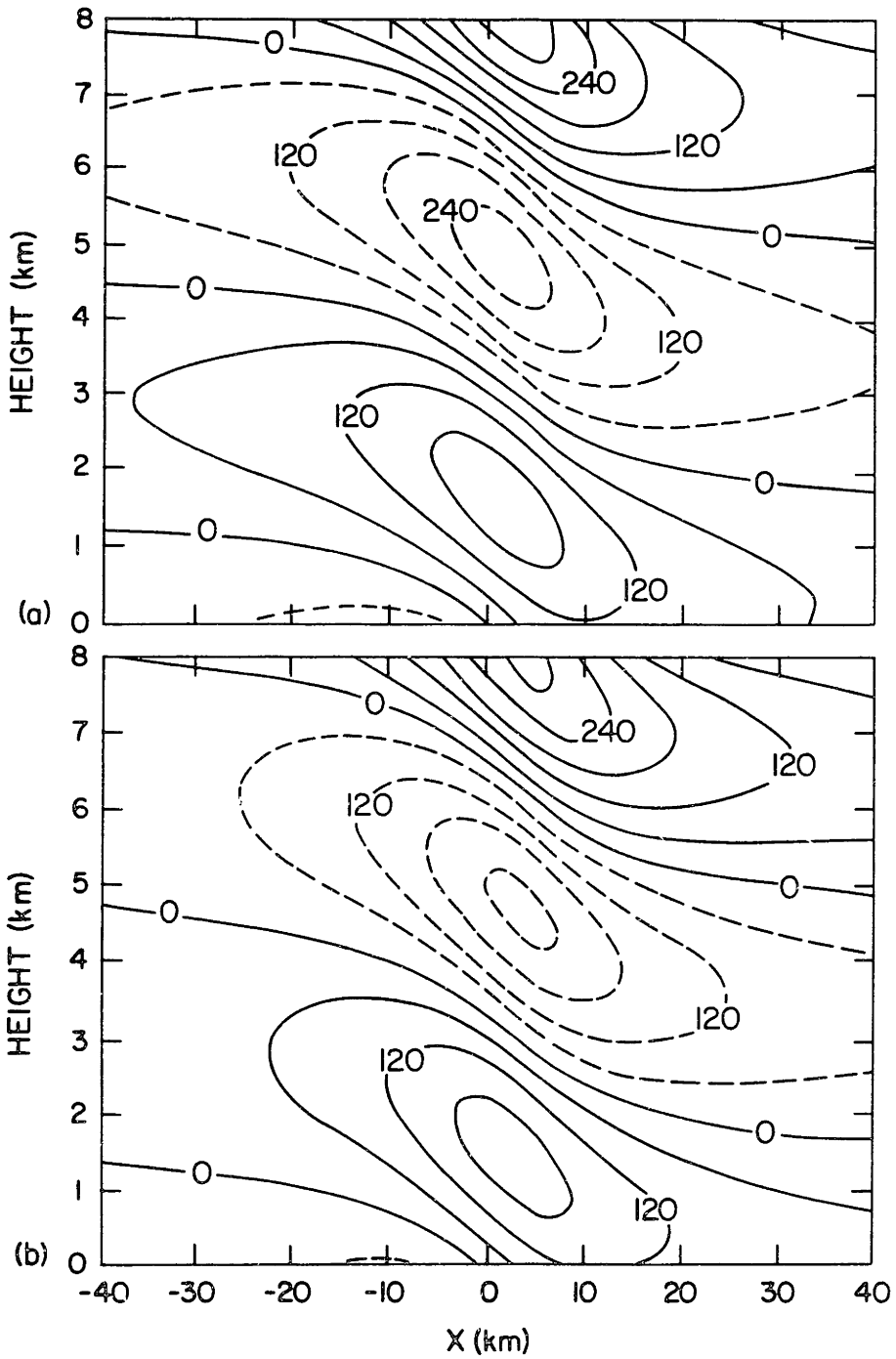

Figure 4.2. (a) Steady state perturbation horizontal velocity from the linear hydrostatic solution for a 1 m high mountain. (b) Perturbation horizontal velocity ($\times 10^{-4}$ ms^{-1}) obtained by numerical simulation for a 1 m high mountain at ut/a=60.

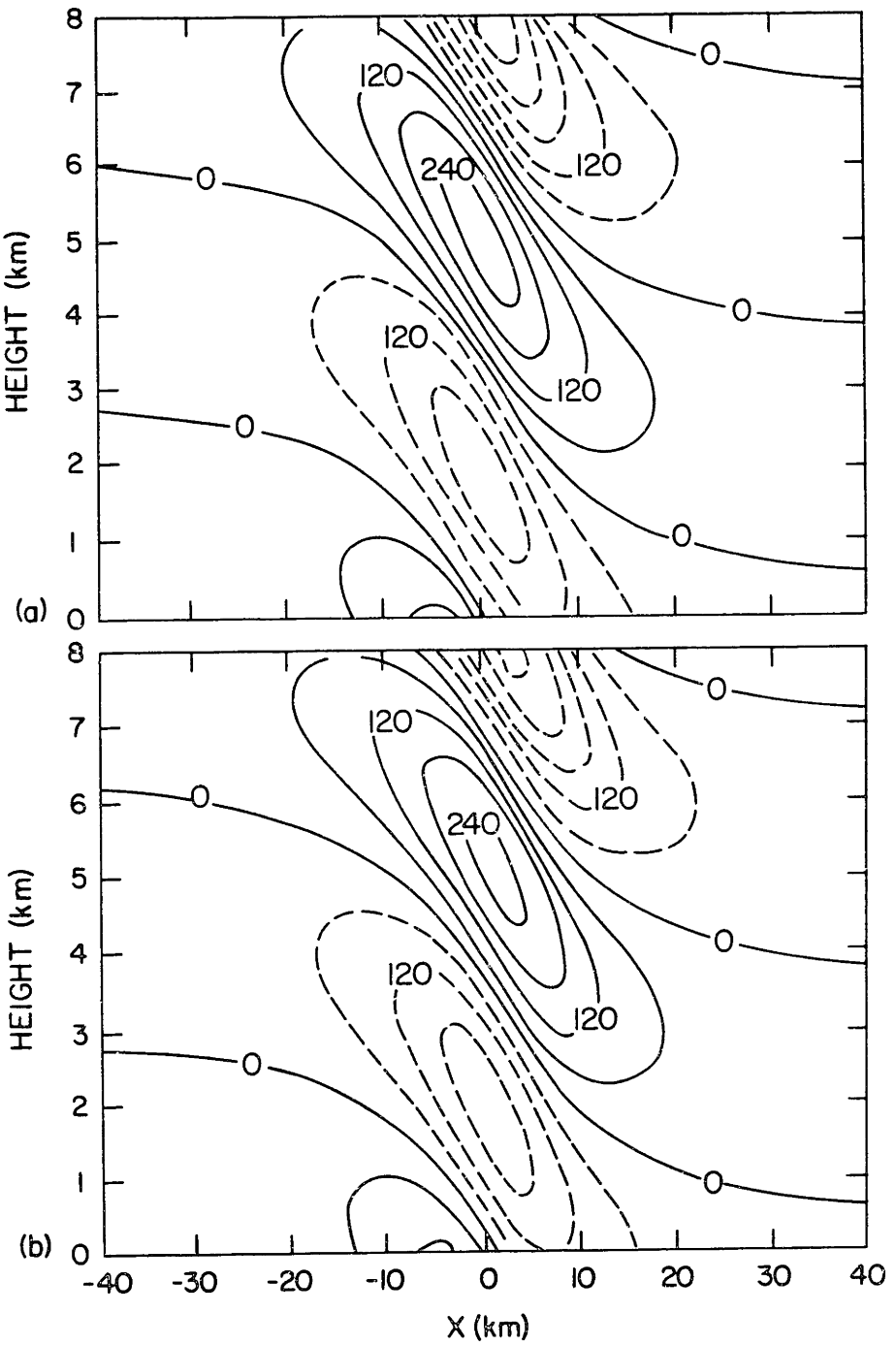

Figure 4.3. (a) Steady state vertical velocity from the linear hydrostatic analytic solution for a 1 m high mountain. (b) Vertical velocity ($\times 10^{-5}$ ms^{-1}) obtained by numerical simulation for a 1 m high mountain at ut/a=60.

compromise between accuracy and computational efficiency could be obtained by locating the lateral boundaries nine mountain quarter widths (9a) upstream and downstream.

Figure 4.4 shows the behavior of the momentum flux computed by the model at several nondimensional times $\bar{u}t/a$; the flux is normalized by its linear analytic value. Below the absorbing layer, in the region from 0 to 8 km, the momentum flux nearly becomes constant with height, but remains a few percent below its linear steady state value. Klemp and Lilly (1980) have calculated the time dependent momentum flux behavior for the linear hydrostatic case in which a mean wind is abruptly introduced at time zero. They found that, at a height of one vertical wavelength (6.4 km), the flux did not reach 95% of its steady state value until a nondimensional time of 35. (Since the model is gradually initialized over four time units, three or four should be subtracted from the times shown in Fig. 4.4 when comparing with Klemp and Lilly's result.) The flux is developing a little more slowly in this model, and even at a nondimensional time of 60, it is still roughly 6% less than the linear analytic value. The difference is not serious, but it may be interpreted as a practical limit on the accuracy of the flux calculations.

The same run was repeated with the fourth order smoother turned off. This change did not affect the vertical momentum flux profiles, so the small gradients in the fluxes shown in Fig. 4.4 are not due to any dissipation explicity included in the numerical formulation. (The subgrid scale mixing was inactive in these simulations because $Ri > 1/3$ everywhere). On the whole, the behavior of the momentum

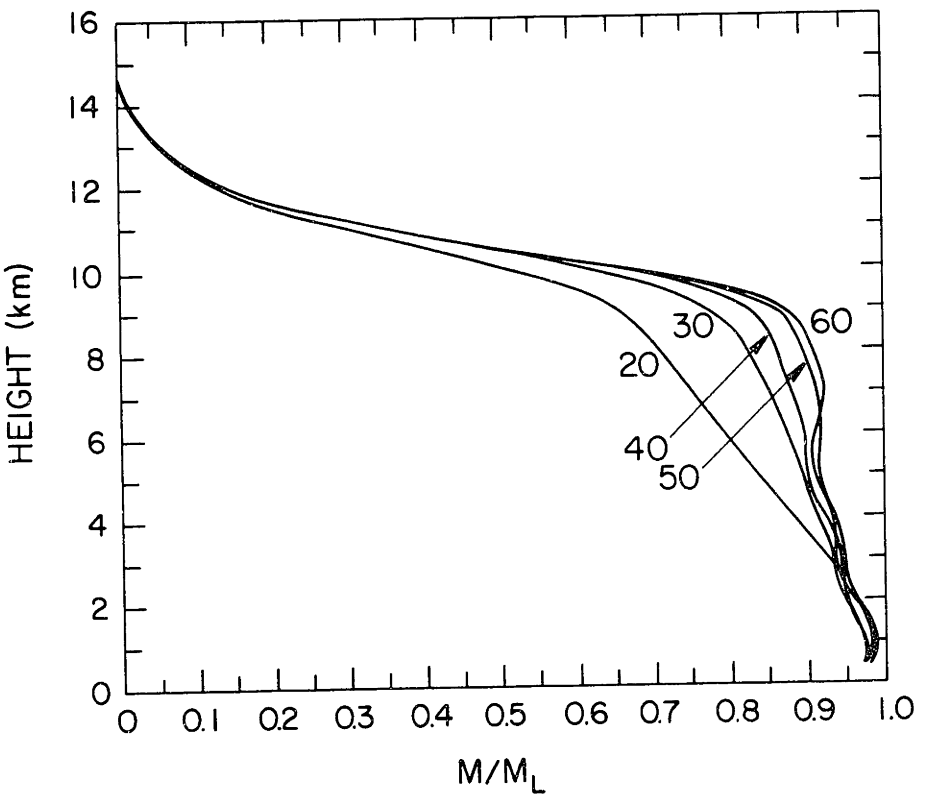

Figure 4.4. Momentum flux normalized by its linear hydrostatic value at several nondimensional times ut/a.

flux, which as a second order quantity is more subject to error than the velocity fields, appears satisfactory.

B. Dry Nonlinear Hydrostatic Solution

In order to examine the model's behavior in a very nonlinear situation, it will be compared against the nonlinear θ coordinate model of Klemp and Lilly, KL, (1978). In the case to be considered, the mean wind far upstream is 20 m/s and constant with height; h = 1000 m, a = 20 km. A wide mountain was selected to minimize the nonhydrostatic mountain forcing. The lowest 10 km represent a troposphere in which the temperature decreases at a constant 6°C/km from a surface value of 280°K. The region from 10-20 km is an isothermal stratosphere which also contains the wave absorbing layer. In this run, the computational domain contains 80 points in the horizontal and 60 levels in the vertical; the absorbing layer occupies the top 30 levels. The grid intervals are Δx = 4 km, Δz = 333 m; the large and small time steps are 16 seconds and 4 seconds, respectively. The streamlines and horizontal velocity field obtained with the model are shown in Figs. 4.5b and 4.6b, which include only the central portion of the domain in which the grid indices run from 10 to 70 in the horizontal and 1 to 30 in the vertical.

The streamlines and horizontal velocity field calculated by the KL model are shown in Figs. 4.5a and 4.6a. Unlike the present model, the KL model is hydrostatic and uses potential temperature as the vertical coordinate. The turbulent mixing parameterization, the strength and structure of the wave absorbing layer, and the positions

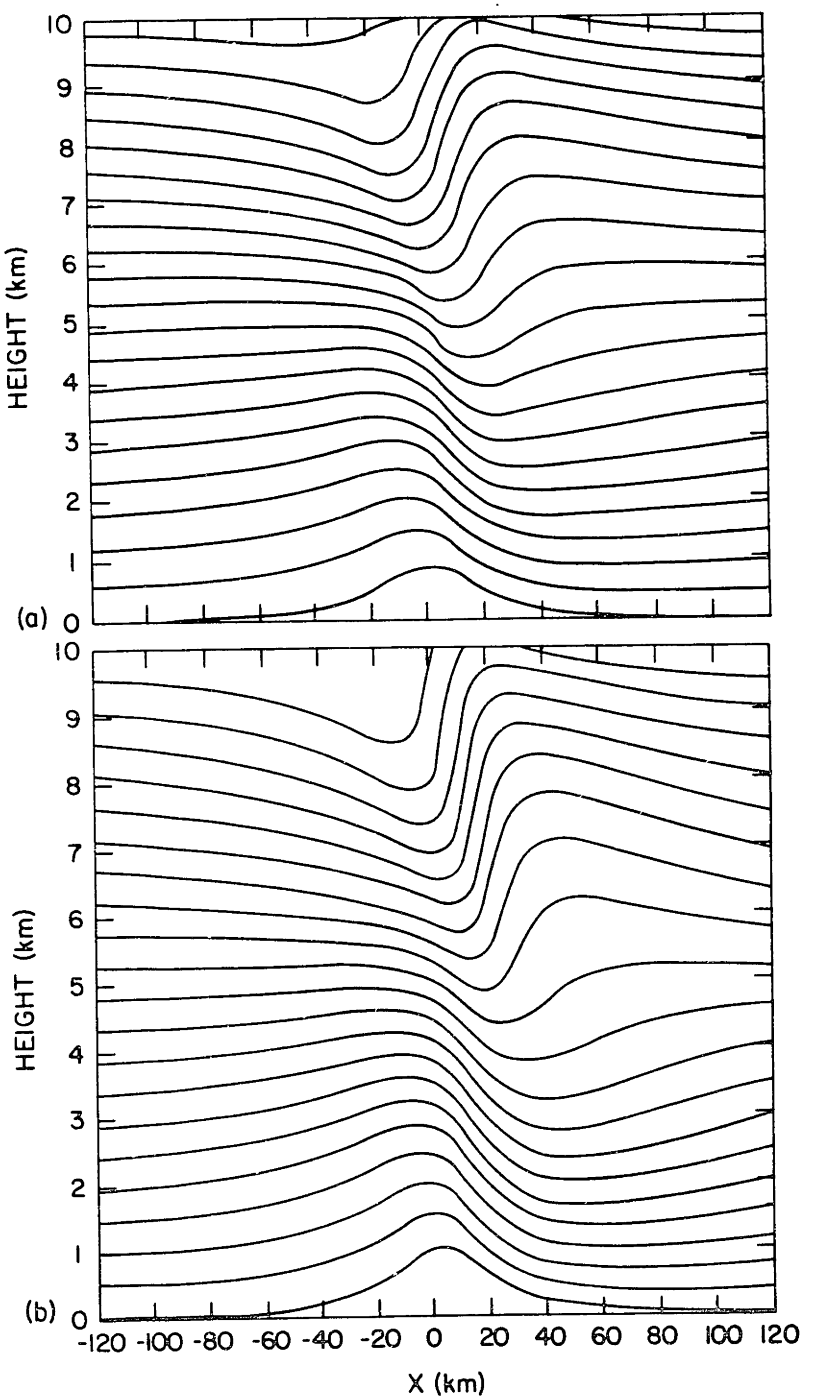

Figure 4.5. (a) Streamlines from the hydrostatic KL model at ut/a=50. (b) Streamlines from the nonhydrostatic model at ut/a=40. Due to differences in the start-up procedures these times are roughly equivalent.

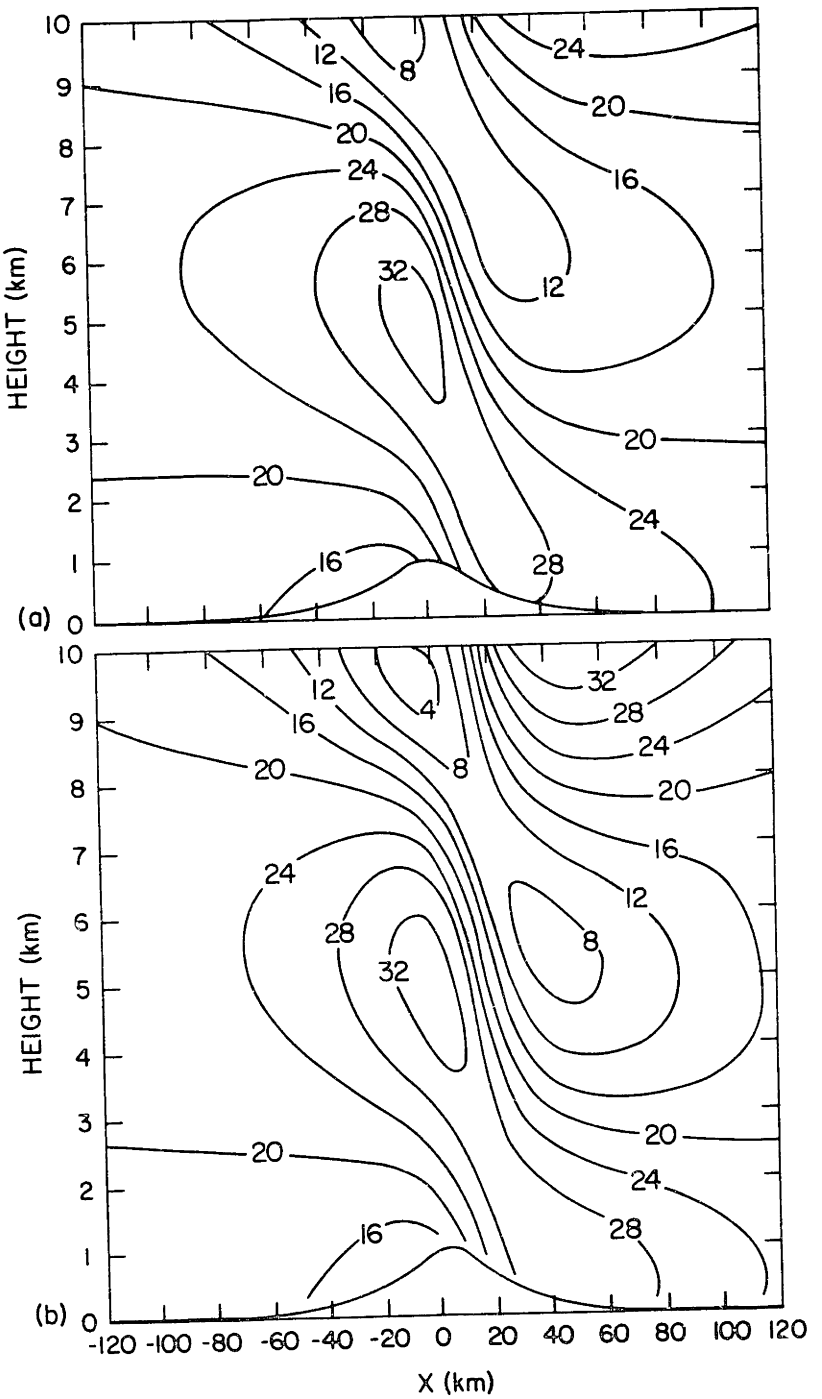

Figure 4.6. (a) Horizontal velocity (ms^{-1}) from the hydrostatic KL model at ut/a=50. (b) Horizontal velocity (ms^{-1}) from the nonhydrostatic model at ut/a=40. Due to differences in the start-up procedures these times are roughly equivalent.

of the lateral boundaries are also different. Details of the KL model and its application to this case may be found in Klemp and Lilly (1978). Considering the difference in the models, Figs. 4.5 and 4.6 agree acceptably well. The biggest differences between the solutions appear around the 10 km level, just below the interface with the wave absorbing layer. It may be that the solutions are being influenced by differences in the absorbing layer structure. Another source of disagreement might be produced by nonhydrostatic effects which could be significant where the highest horizontal wavenumbers appear in the solution, around the steepened wavefront.

The KL solution remains almost steady in time, but the nonhydrostatic solution creeps very slowly toward larger amplitude and eventually overturns. (Note that overturning is not formally allowed by the θ coordinate KL model.) It is not clear whether the small but persistent nonsteadiness in this solution represents a real physical behavior or is simply computational error. Nonsteadiness is not an inherent feature in every model run; many other nonlinear simulations do reach a virtually steady final state. Because of the uncertainties introduced by this slight nonsteadiness, highly nonlinear wave amplitudes will be avoided in the next two chapters in which we examine the effects of moisture on trapped and propagating mountain lee waves.

V. THE EFFECTS OF MOISTURE ON TRAPPED LEE WAVES

The Scorer parameter is the maximum horizontal wavenumber with which steady linear gravity waves can propagate in the vertical. If the Scorer parameter decreases with height, there will be a range of wavenumbers over which gravity waves can have a periodic vertical structure only near the ground. If this decrease is abrupt and sufficiently large, one or more trapped resonant waves can develop. When such a wave is generated by airflow over a mountain of appropriate horizontal scale it is called a trapped lee wave.

In this chapter we will examine the effects of moisture on trapped lee waves. Our attention will be confined to nonprecipitating clouds. In the real atmosphere, precipitation is almost never produced in the short wavelength clouds which form in the crests of trapped lee waves, because the liquid water content in these clouds is too low. If rain or snow is associated with a mountain wave event, it usually falls from a cap cloud which impinges on the windward slopes of the mountain. In this chapter we will consider only narrow ridges which, although they are ideal for generating trapped resonant waves, do not produce large cap clouds. The liquid water concentrations generated by forced uplift, and the in-cloud residence time of the water droplets in these small cap clouds are insufficient to produce precipitation.

A. Linear Trapped Waves

Before considering moisture, it is instructive to review the dynamics of dry lee waves. We will follow the development of Scorer (1949). Consider the behavior of trapped waves in a two layer atmosphere where the Scorer parameter is equal to l_2^2 and l_1^2 in the upper and lower layers, respectively. Suppose that the interface is at z = 0 and the base of the mountain at z = -H. The small effects of compressibility on the Scorer parameter are neglected so that Eq. (2.2) becomes

$$k_s^2 = \frac{N^2}{\bar{u}^2} - \frac{\bar{u}_{zz}}{\bar{u}} \quad . \tag{5.1}$$

If $\hat{z}_s$ is the Fourier transformed mountain profile, the field of vertical motion is given by the inverse transform

$$w(x,z) = \left(\frac{\bar{\rho}}{\bar{\rho}_0}\right)^{-1/2} \mathrm{Re}\left\{\int_0^\infty ik\bar{u}z_s(k)\,\frac{\hat{w}(z,k)}{w(-H,k)}\,e^{ikx}dk\right\} \quad . \tag{5.2}$$

Consider the case where $\bar{u}_z$ is zero at the interface, for a wavenumber in the range $l_2 < k < l_1$, the solution to Eq. (2.4) in the upper and lower layers is

$$\left.\begin{aligned} \hat{w}_1(z,k) &= iAk\bar{u}\left(\cos\lambda_1 z - \frac{\lambda_2}{\lambda_1}\sin\lambda_1 z\right) \\ \hat{w}_2(z,k) &= iAk\bar{u}\,e^{-\lambda_2 z} \end{aligned}\right\} \tag{5.3}$$

where

$$\lambda_1(k) = \sqrt{l_1^2 - k^2} \quad , \qquad \lambda_2(k) = \sqrt{k^2 - l_2^2} \quad . \tag{5.4}$$

The small effects of compressibility have also been ignored in the interface matching conditions. For further discussion of the matching procedure see Vergeiner (1971). The resonant wave must have zero vertical velocity at the ground downstream from the mountain, so the resonant wavenumber k_r must satisfy $\hat{w}_1(-H,k_r) = 0$ or

$$\tan \lambda_1 H = -\frac{\lambda_1}{\lambda_2} \quad . \tag{5.5}$$

This equation will have at least one solution when

$$l_1^2 - l_2^2 \geq \frac{\pi^2}{4H^2} \quad . \tag{5.6}$$

Thus, for a given lower layer depth, a minimum difference in the Scorer parameter is required to support resonant waves. If there is more than one resonant mode, the mode with the lowest horizontal wavenumber dominates.

The most important contributions to the integral in Eq. (5.2) come near $k = 0$ and the pole $k = k_r$. The first may be evaluated asymptotically and represents a vertically propagating wave which decays downstream. The contribution from the pole at $k = k_r$ produces a train of shorter trapped waves which (in the inviscid case)

extend downstream to infinity. The trapped wave streamlines may be obtained exactly by residues, in the lower layer they are

$$\delta_1(x,z) = -2ha\pi \left(\frac{\lambda_1}{H + \frac{1}{\lambda_2}} \right) \frac{e^{-ak_r}}{k_r} \sin\left(\lambda_1(H+z)\right) \sin k_r x \quad . \quad (5.7)$$

The potential temperature, windspeed and Scorer parameter (k_s) profiles for a two layer atmosphere in which k_s^2 decreases abruptly with height are shown in Fig. 5.1. Figure 5.2 shows the streamlines and vertical velocity field produced when this flow encounters a small amplitude mountain of the shape given in Eq. (2.6) with h = 1 m and a = 2.5 km. In this simulation the domain contains 100 points in the horizontal and 48 levels in the vertical; the absorbing layer occupies the top 24 levels. The grid intervals are Δx = 800 m, Δz = 333 m; the large and small time steps are 12.5 and 2-1/12 seconds, respectively. The model is run until the solution reaches a nearly steady state. (This requires between 12000 and 16000 s.) Figure 5.2 includes only the central part of the domain which runs from x = -12 km to x = 36 km in the horizontal and z = 0 to z = 8 km in the vertical. The mountain peak is at x = 0. Trapped lee waves are clearly visible; a weak vertically propagating wave is also present.

If the Scorer parameter used in the numerical calculations had a perfect two layer vertical structure, at distances far downstream from the mountain the streamlines in Fig. 5.2 should be given by Eq. (5.8). However, as shown in Fig. 5.1, the two layer structure is not perfect. The profile used in the calculations drops from a nearly

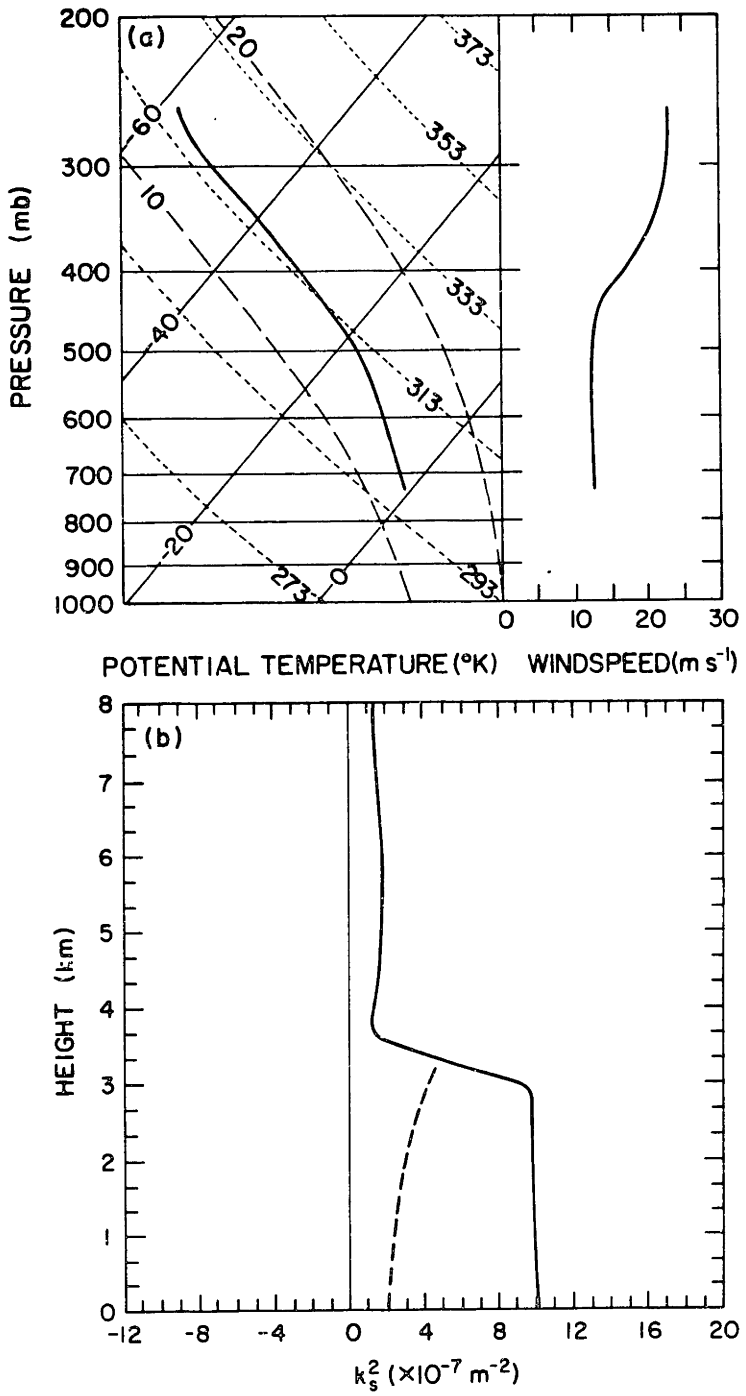

Figure 5.1. Absolutely stable atmosphere favorable for the development of dry lee waves. (a) Temperature and windspeed profiles, dry adiabats are marked with a short dashed line, moist psuedo-adiabats with a long dashed line. (b) Scorer parameter (k_s^2 profiles, the dry k_s^2 is marked with a solid line, the equivalent saturated k_s^2 is dashed.

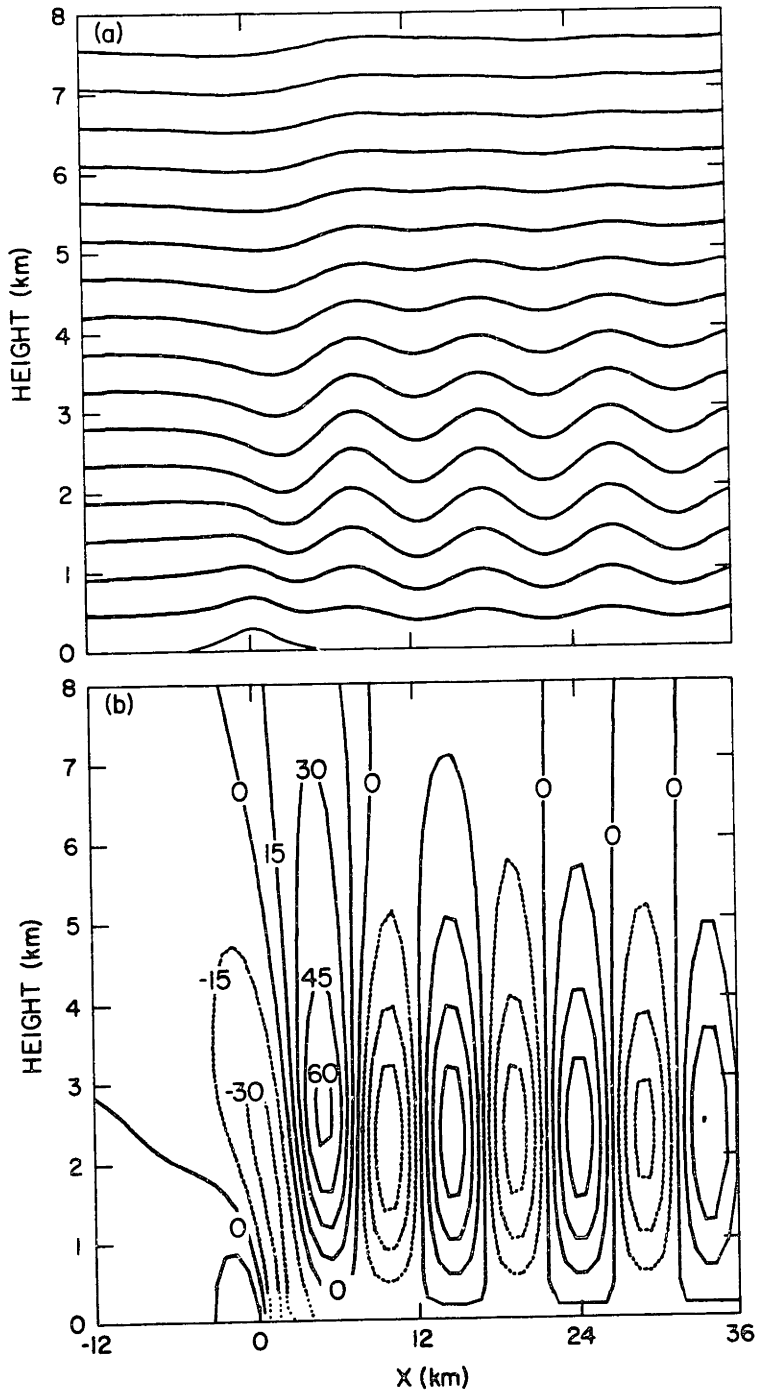

Figure 5.2. (a) Streamlines, and (b) vertical velocities ($\times 10^{-3}$ ms^{-1}) produced by a 1 m high mountain when RH=0% upstream. The streamline displacements are multiplied by 300 for display.

constant value of 1.0×10^{-6} m^{-2} to a nearly constant value of 1.5×10^{-7} m^{-2} in a transition layer two grid points deep. The finite depth of this layer is due in part to the difficulty of resolving discontinuities on a numerical grid , and in part to the difficulty of determining realistic vertical profiles of $\bar{u}$ and θ which produce a single sharp discontinuity in Scorer parameter. Nevertheless, k_s^2 has a basically two layer structure in the numerical calculations, so the resulting flow should be given approximately by Eq. (5.7).

Table 5.1 gives the maximum vertical velocity (w_{max}) and lee wavelength predicted by Eq. (5.7) for interface heights in the range $3 - \Delta z$ km to $3 + \Delta z$ km. Over this range, the wavelength varies between 8.7 and 10.3 km, and w_{max}, which exhibits a strong sensitivity to H, varies between 4.9×10^{-3} and 7.8×10^{-3} ms^{-1}, respectively. The average wavelength and w_{max} estimated from the numerical run (Fig. 5.2) for waves well downstream from the mountain are 9.6 km and 5.5×10^{-3} ms^{-1}, respectively. These fall within the range of Table 5.1. Given the coarse numerical resolution at the interface, this rough quantitative agreement seems satisfactory.

As in the case just discussed, the dynamics of dry lee waves are determined by the vertical profiles of $\bar{u}$ and θ, and the mountain contour. The dynamics of moist waves also depend on the sensible temperature and the vertical profile of moisture. The importance of the sensible temperature must not be overlooked; in order to obtain practical results the vertical profile of sensible temperature must be physically reasonable. Unrealistically high temperatures will allow the air to hold so much water vapor that latent heat effects will be

Table 5.1

The effect of variations in the lowest layer depth on resonant wavelength and vertical velocity

Lower layer depth, H (m)	Lee wavelength (km)	Maximum vertical velocity ($\times 10^{-3}$ ms^{-1})
2667	10.3	7.8
2833	9.7	6.9
3000	9.3	6.1
3167	9.0	5.5
3333	8.7	4.9

exaggerated. Similarly, if the air is unrealistically cold, latent heat effects will be minimized. The physical cases described in this chapter are roughly representative of springtime air masses flowing over the Continental Divide in the Colorado Rockies.

Consider again the atmosphere shown in Fig. 5.1, and let the upstream flow be moist so that the lowest layer (between 0 and 3 km) is saturated and contains a uniform cloud bearing 0.2 g kg^{-1} of liquid water. Figure 5.3 shows the streamlines and vertical velocity field for this case, which, except for the moisture, is identical to the one shown in Fig. 5.2. Since the waves generated by the 1 m high mountain have small amplitude, the cloud never dissipates in the wave troughs and latent heat effects are symmetric in the troughs and crests. The practical effect of the latent heat released is to change the stability, and hence the Scorer parameter, in the lowest layer. The Brunt-Väisälä frequency applicable in a saturated region may be written

$$N_E^2 = g \frac{\gamma_m}{\gamma_d} \frac{d \ln \theta_E}{dz} \quad . \tag{5.8}$$

This is essentially the same expression derived by Deardorff (1976), where the ratio of the moist and dry adiabatic lapse rates γ_m/γ_d is

$$\frac{\gamma_m}{\gamma_d} = \left(1 + \frac{Lq_{vs}}{RT}\right)\left(1 + \frac{\varepsilon L^2 q_{vs}}{c_p R T^2}\right)^{-1} \quad . \tag{5.9}$$

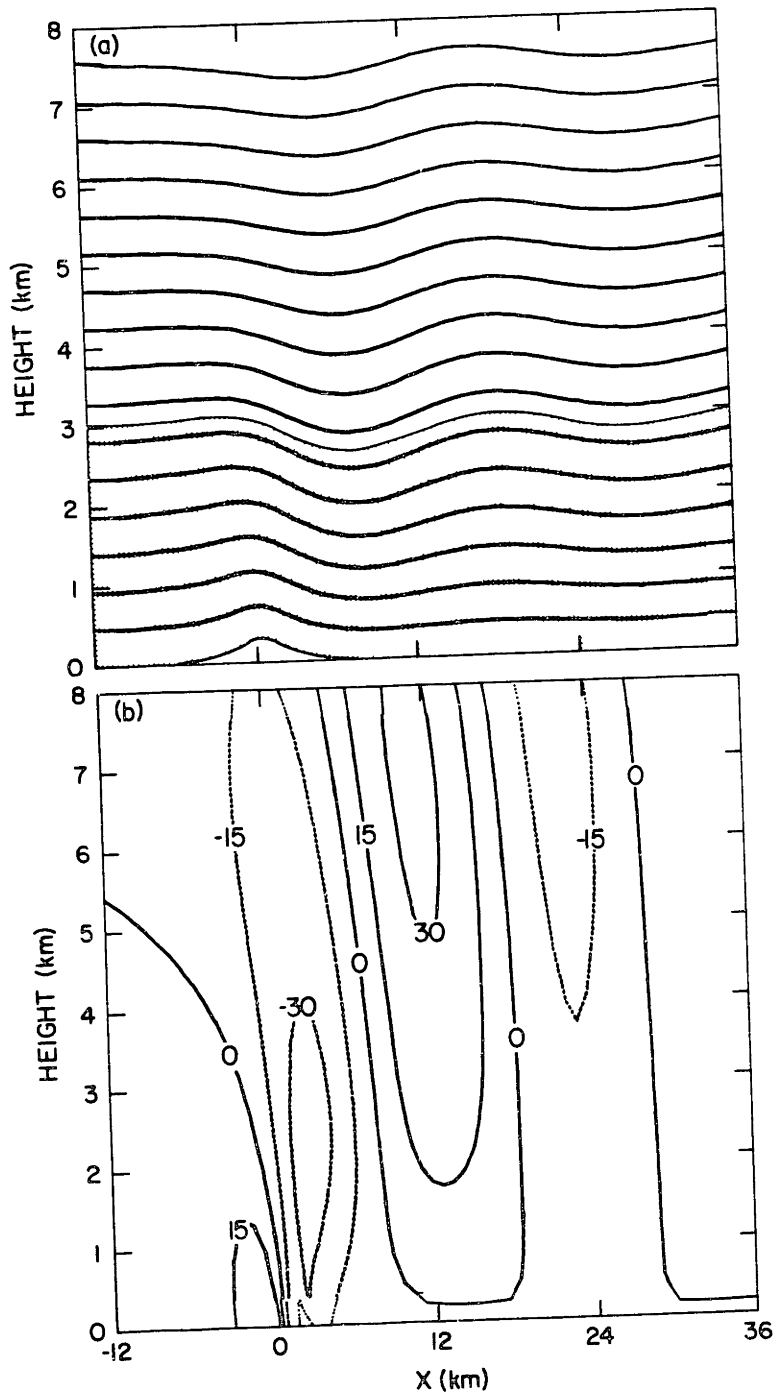

Figure 5.3. As in Fig. 5.2, except that RH=100% and there is 0.2 gm/kg of cloud in the lowest layer upstream. Cloudy regions are stipled.

The saturated Scorer parameter structure obtained by replacing N^2 by N_E^2 in Eq. (5.1) is shown in Fig. 5.1b. Note that the two layer structure is much weaker in the saturated case; in fact the decrease in k_s^2 is too small to satisfy Eq. (5.6) so resonant trapped waves should not occur. This is indeed the case; as shown in Fig. 5.3, the waves are weak and vertically propagating. The addition of moisture untraps the waves.

The dry and everywhere cloudy flows are limiting cases; consider a situation where the lowest upstream layer is saturated but cloud-free. The streamlines and vertical velocity field for this flow are shown in Fig. 5.4. Condensation and evaporation occur only in the wave crests, decreasing the local stability and increasing the local wavelength. The flow in the troughs, which remain unsaturated, is similar to the dry case. The waves develop broad flat crests and narrow troughs, producing the distinctive asymmetry in the vertical velocity field shown in Fig. 5.4b. The waves remain trapped although their overall horizontal wavelength is much longer than in the dry case. The maximum vertical velocities are slightly weaker than those in the dry waves, but much stronger than the maximums in the everywhere cloudy case.

When the lowest layer is cloudy everywhere, the effects of moisture can be approximated by replacing the moist layer with a dry layer of suitably reduced stability. No similar simple a priori approximation can be made in the partially cloudy case. The need to determine the cloud boundaries makes even the small amplitude problem difficult.

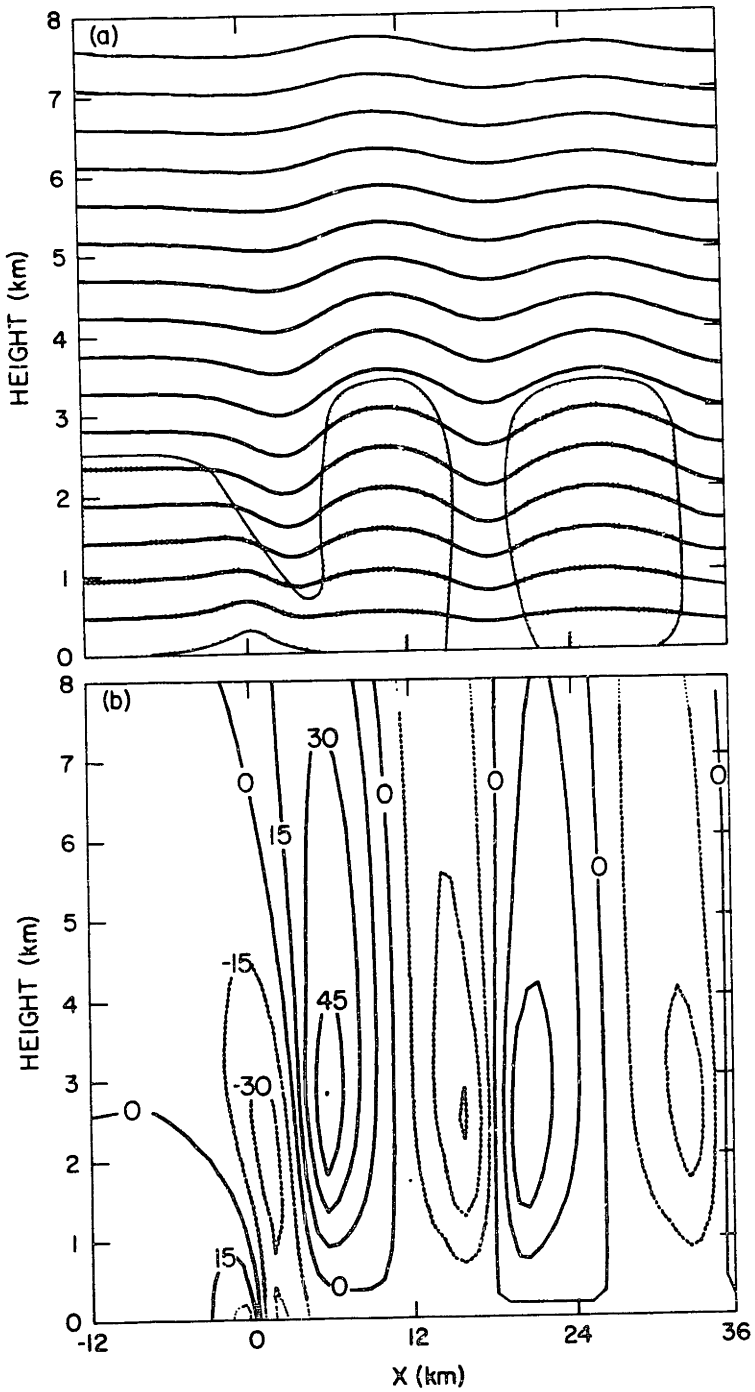

Figure 5.4. As in Figs. 5.2 and 5.3, except that RH=100% in the lowest layer upstream.

Although they can produce useful results, small amplitude flows are not the best situations in which to examine moisture effects, since they produce only very small displacements. As a consequence, they respond identically to flows in which RH = 0% and RH = 99% upstream. In the next section we will remove this constraint by examining the effects of moisture on finite amplitude flows.

B. Finite Amplitude Trapped Waves

1. Resonant wave distortion and untrapping due to the addition of moisture

Consider again the atmosphere shown in Fig. 5.1. The height of the mountain is increased to 300 m, and the linear runs described in the previous section are repeated. All the computational parameters except the mountain height are unchanged. The streamlines produced by different amounts of upstream humidity are shown in Fig. 5.5. The basic behavior is the same as in the linear case; the addition of moisture to the flow distorts and, when enough water is present, untraps the lee waves. As shown in Fig. 5.5b, in the finite amplitude case an upstream humidity of RH = 90% is sufficient to strongly affect the flow.

The linear trapped wave solutions for a 300 m high mountain (Figs. 5.2a and 5.4a) are distinctly weaker than the nonlinear solutions for the same mountain (Fig. 5.5a,c). This agrees with the observation of Smith (1976), who found that linear theory consistently underpredicted the amplitude of lee waves produced by the Blue Ridge. The streamlines for the nonlinear waves also show more variation in

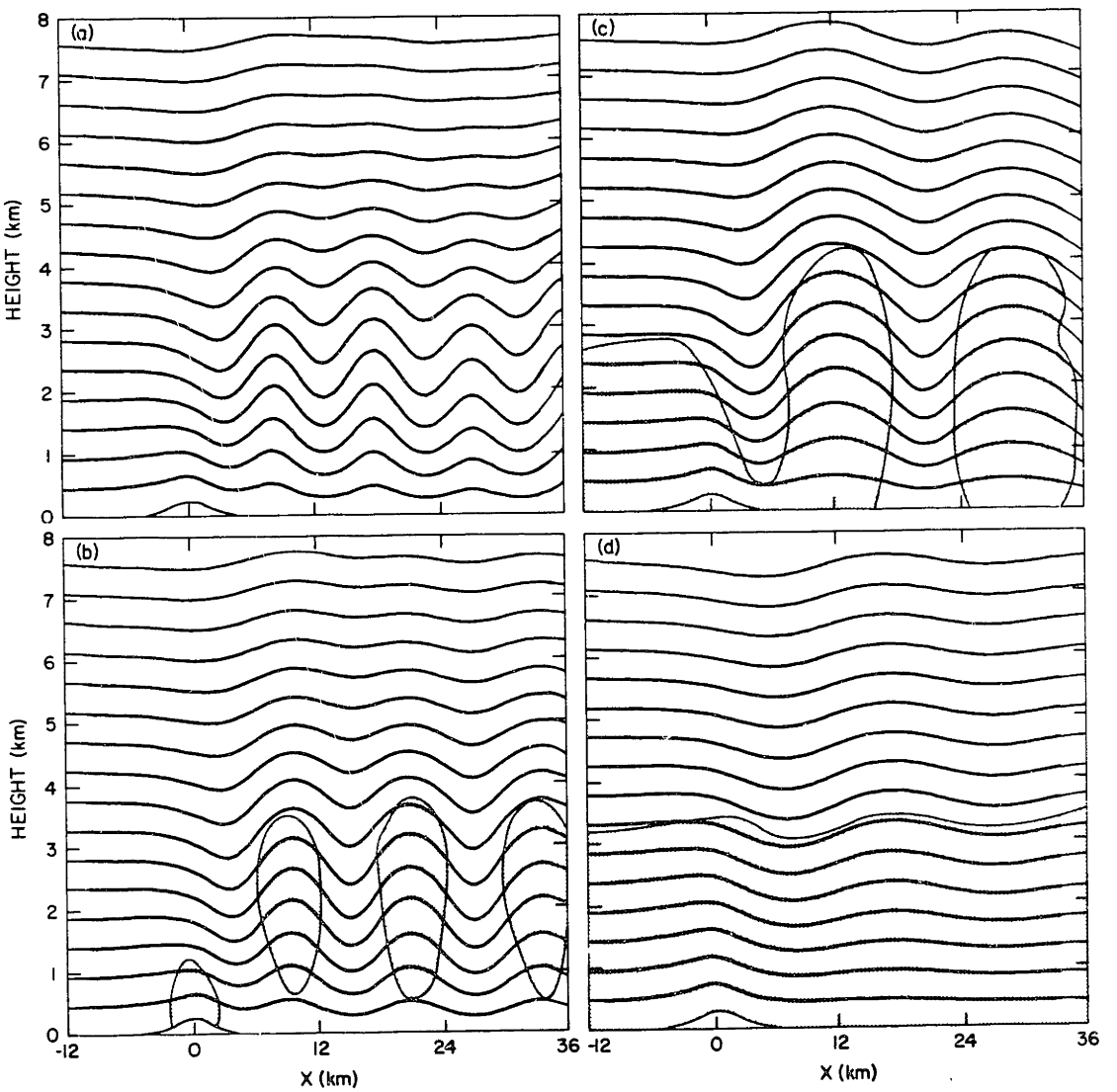

Figure 5.5. Streamlines produced by a 300 m high mountain in the flow shown in Fig. 5.1, for (a) RH=0%, (b) RH=90%, (c) RH=100%, (d) RH=100% with 0.2 gm/kg of cloud, in the lowest layer upstream. Cloudy regions are stipled.

the amplitude of successive waves than their linear counterparts. The difference between successive waves increases as the mountain height increases and the flow becomes more nonlinear.

2. Resonant wave breakdown due to the addition of moisture to a conditionally unstable layer

In the previous case, the lowest layer was absolutely stable, so that latent heat release reduced, but did not destroy the local stability. Dry lee waves can also exist in a region which is conditionally unstable. The potential temperature, windspeed and k_s^2 profiles for such an atmosphere are shown in Fig. 5.6. Although the $\bar{u}$ and θ profiles are different, the dry Scorer parameter structure is nearly identical to that seen earlier in Fig. 5.1. As a result, the streamlines for the dry lee wave solution (Fig. 5.7a) are very similar to those for the previous run (Fig. 5.5a). However, when the flow is initialized with RH = 90% in the lowest layer upstream, the two cases are very different.

As shown in Fig. 5.7b-d, steady waves are not produced in the conditionally unstable case. Condensation occurs in the crest of the first lee wave, but then the cloudy regions act as buoyant plumes. At first their ascent is limited by the lack of moisture in the upper layer, but as more water mixes upward they rise higher and destroy the lee wave structure. This is easy to observe in Fig. 5.7d where the clouds are aligned with the updrafts, rather than the crests, in the short wave turbulence. The two dimensional model probably does not accurately simulate the details of the moist turbulent breakdown, but I believe the basic character of the solution can be accepted with confidence.

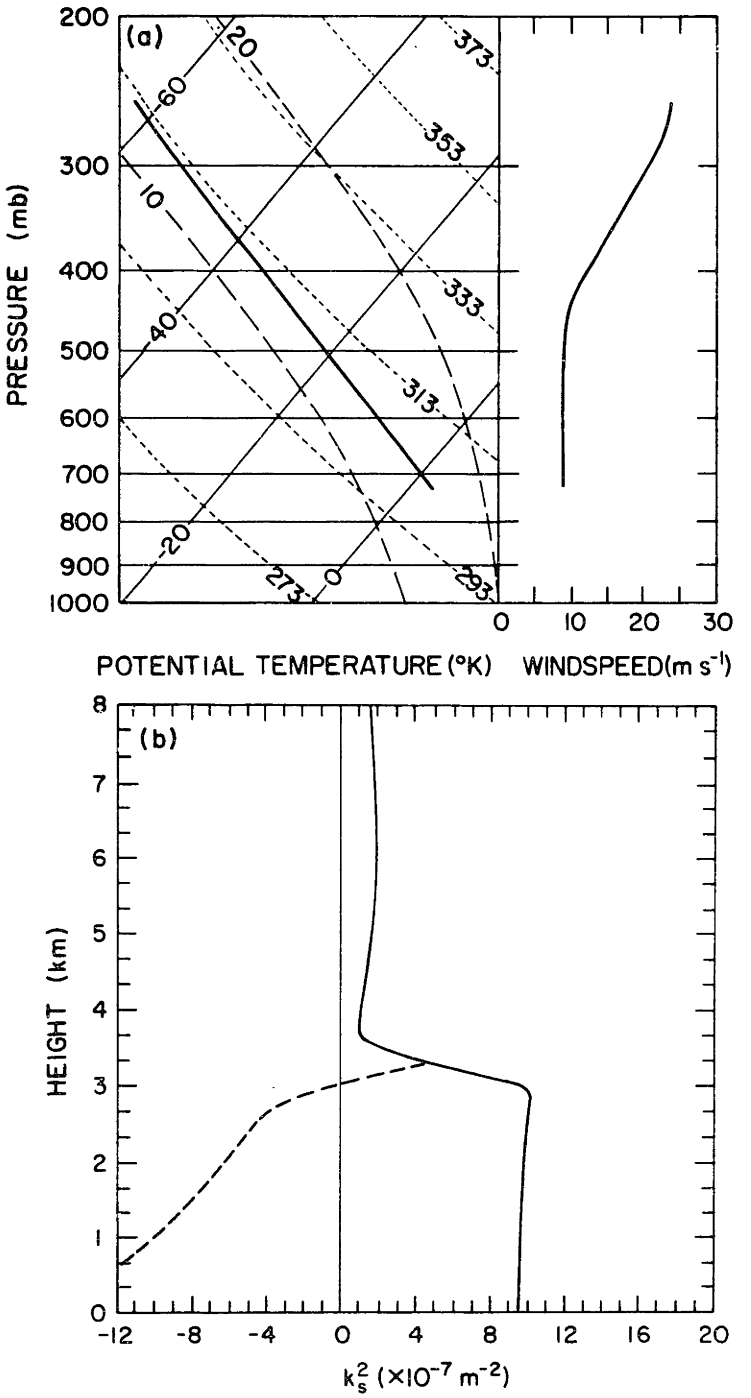

Figure 5.6. As in Fig. 5.1 for a conditionally unstable atmosphere favorable for the development of dry lee waves.

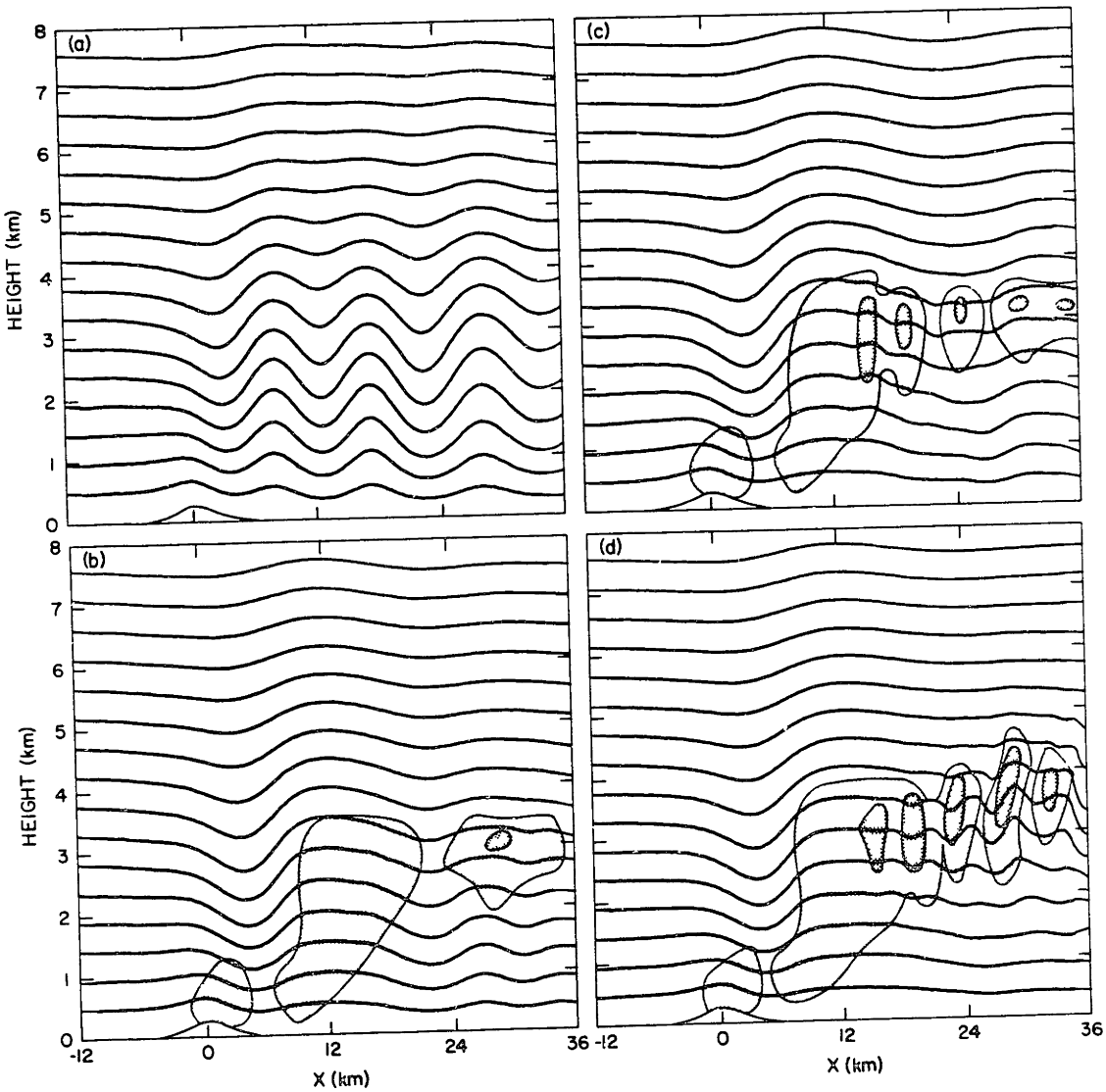

Figure 5.7. Streamlines produced by a 300 m high mountain in the flow shown in Fig. 5.6. (a) Steady solution for RH=0%. Time dependent flow for RH=90% in the lowest upstream layer at, (b) t=8000 s, (c) t=12000 s, (d) t=16000 s. Cloudy regions are stipled; dark stipling indicates cloud densities exceeding 0.3 gm/kg.

3. Resonant wave detuning due to the removal of moisture

Suppose that the atmospheric structure is favorable for trapped resonant waves when the lowest layer is saturated and cloudy upstream. If the cloud is sufficiently dense that the lee wave troughs remain saturated, Eq. (5.9) can be used to compute an effective moist Scorer parameter. Figure 5.8 shows the potential temperature, windspeed and k_s^2 profiles for such a case; note that the moist Scorer parameter structure is almost identical to the dry k_s^2 structure in Figs. 5.1 and 5.6. Since the Scorer parameter is nearly the same, the linear waves produced by a 1 m high mountain in the cloudy atmosphere should be almost identical to the dry linear waves discussed earlier. A comparison of Figs. 5.9a and 5.2a shows that the two solutions agree quite well. This comparison verifies that the moist processes are represented properly in the numerical model.

In the finite amplitude case (Fig. 5.9b) the waves are similar but distinctly stronger than their dry counterparts (Figs. 5.5a and 5.7a), and there is greater variation in amplitude between successive waves. This is not necessarily surprising since the nonlinear terms in the moist equations differ from those in the dry system. The crucial difference seems to be produced by the curvature of the moist adiabats. If the moist adiabats were straight (though not necessarily of uniform slope), a saturated parcel would release the same amount of latent heat every time it was lifted 1 m. In reality, as a parcel rises it cools, so it holds less water vapor and releases less latent heat over each successive meter of its vertical displacement. Thus, in a saturated lee wave the effects of condensation are strongest in

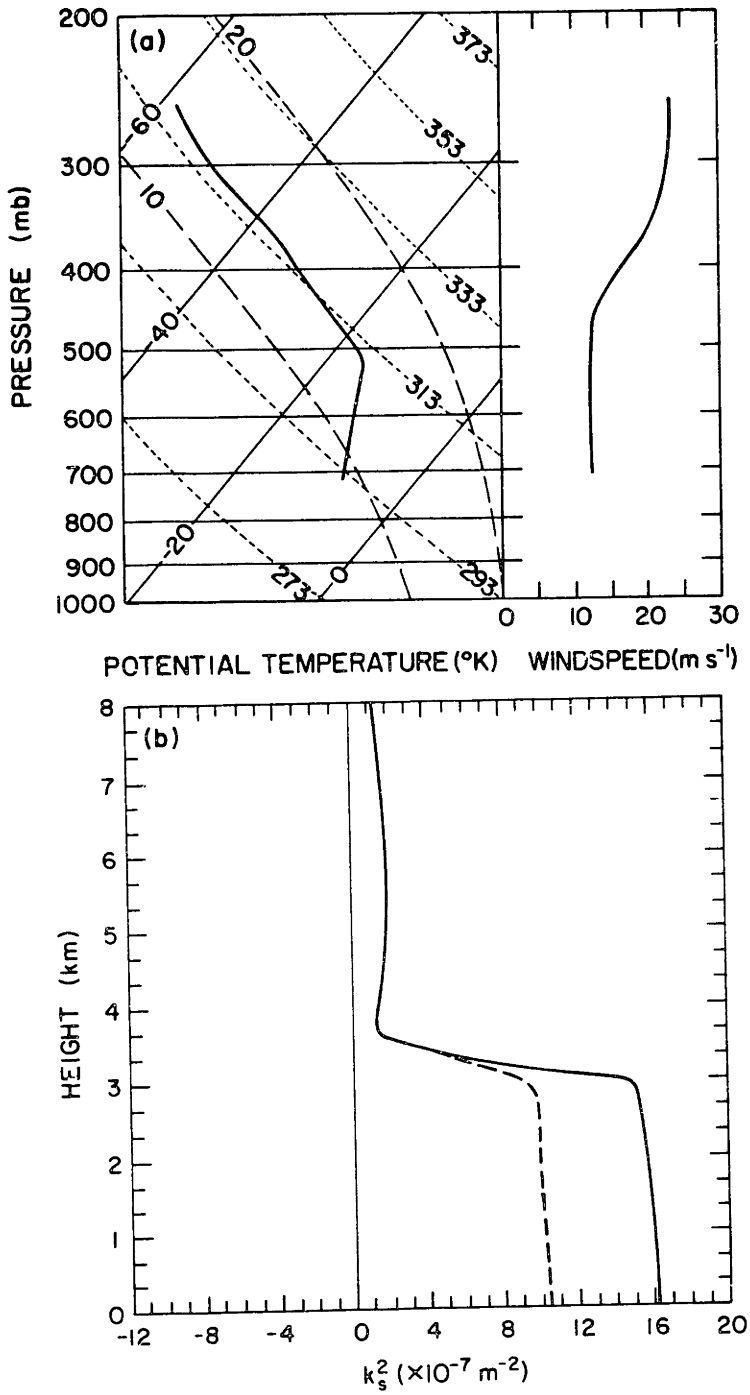

Figure 5.8. As in Fig. 5.1 for an absolutely stable atmosphere favorable for the development of saturated lee waves.

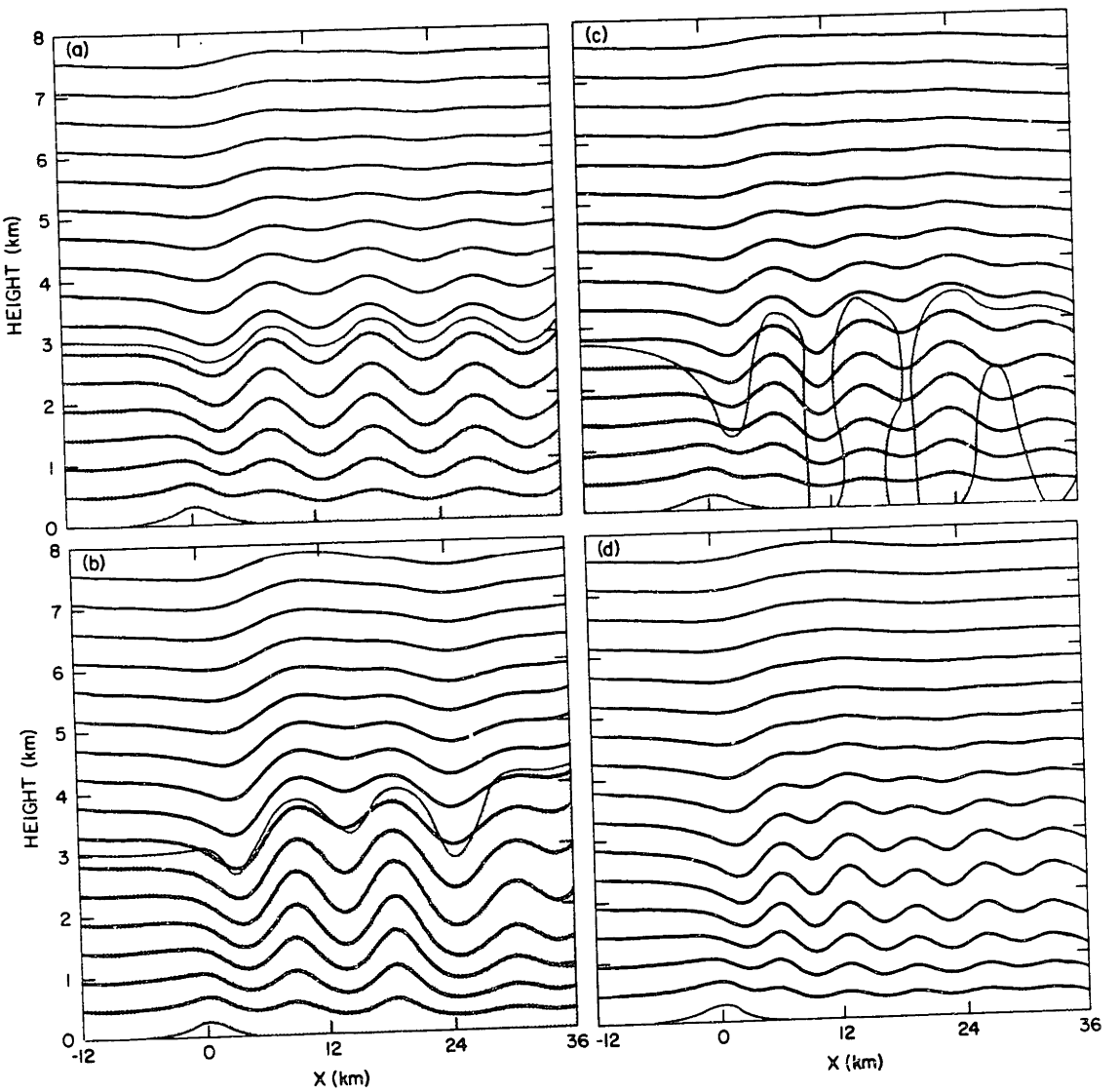

Figure 5.9. Streamlines produced by the flow shown in Fig. 5.8, (a) by a 1 m high mountain when RH=100% and there is 0.2 gm/kg of cloud in the lowest layer upstream, and by a 300 m high mountain when, (b) RH=100% and there is 0.2 gm/kg of cloud, (c) RH=100%, (d) RH=0%, in the lowest layer upstream. Cloudy regions are stipled. In (a) only, the streamline displacements are multiplied by 300, producing a good approximation to the linear solution for a 300 m high mountain.

the wave troughs and weakest in the wave crests. The importance of this asymmetry depends on the amplitude of the wave. It is insignificant in linear waves but, as shown by the difference between Figs. 5.5a and 5.9b, it has considerable influence in moderately strong waves.

When the lowest upstream layer is saturated but cloud-free, condensation does not occur in the wave troughs, and the overall wavelength is decreased. Trapped waves still occur as shown in Fig. 5.9c, but since the mountain does not force this shorter wavelength as efficiently, the wave amplitude is reduced. When the lowest layer is completely dry, the wave amplitude and resonant wavelength are further reduced as shown in Fig. 5.9d. When strong waves exist in a cloudy atmosphere, the removal of moisture detunes the resonance reducing the amplitude of the lee waves.

C. Moisture in the Upper Layer

One might well ask what effect the introduction of moisture above a wave trapping interface has on the flow. If the upper layer is conditionally unstable and rather moist, lee waves could conceivably trigger a thunderstorm. Booker (1963) has suggested that mountain lee waves might sometimes encourage the development of thunderstorms in the Allegheny Mountains. Although the possibilities are interesting, the study of lee wave induced thunderstorms is beyond the scope of this investigation. If the upper level is absolutely stable, the introduction of moisture could reduce the stability and Scorer parameter in that layer, thereby trapping lee waves which could propagate

vertically if the air were dry. However, the upper troposphere, being rather cold, does not contain much water vapor so latent heat effects are reduced, and the impact of moisture on the Scorer parameter decreases accordingly. Therefore, the only waves which could be trapped by changes in moisture in the upper layer would have a horizontal wavenumber very close to the critical value which satisfies Eq. (5.6) by equality. This situation requires a very special atmospheric structure and probably has little physical significance.

A more common situation in which moisture at mid-tropospheric levels might affect trapped lee waves occurs when the lower layer, in which k_s^2 is large, is rather deep. If moisture is introduced to the top of the lower layer, it can reduce the stability and Scorer parameter in that region to a value similar to that in the upper layer. The practical effect is to move the wave trapping interface down, increasing the lee wavelength and amplitude. The k_s^2 profiles for this type of case are shown in Fig. 5.10a. The dry linear lee wave flow is shown in Fig. 5.11a; weak trapped waves are visible. When the flow is saturated and contains 0.2 g kg^{-1} of cloud between the heights of 2.3 and 4.0 km far upstream, the effective height of the wave trapping interface is lowered and, as shown in Fig. 5.11b, a stronger wave develops.

One might conclude from Table 5.1 that decreasing the height of the wave-trapping interface always produces stronger lee waves. Figure 5.12 shows the effects of changes in the interface height on the wavelength and amplitude of the two lowest order trapped wave

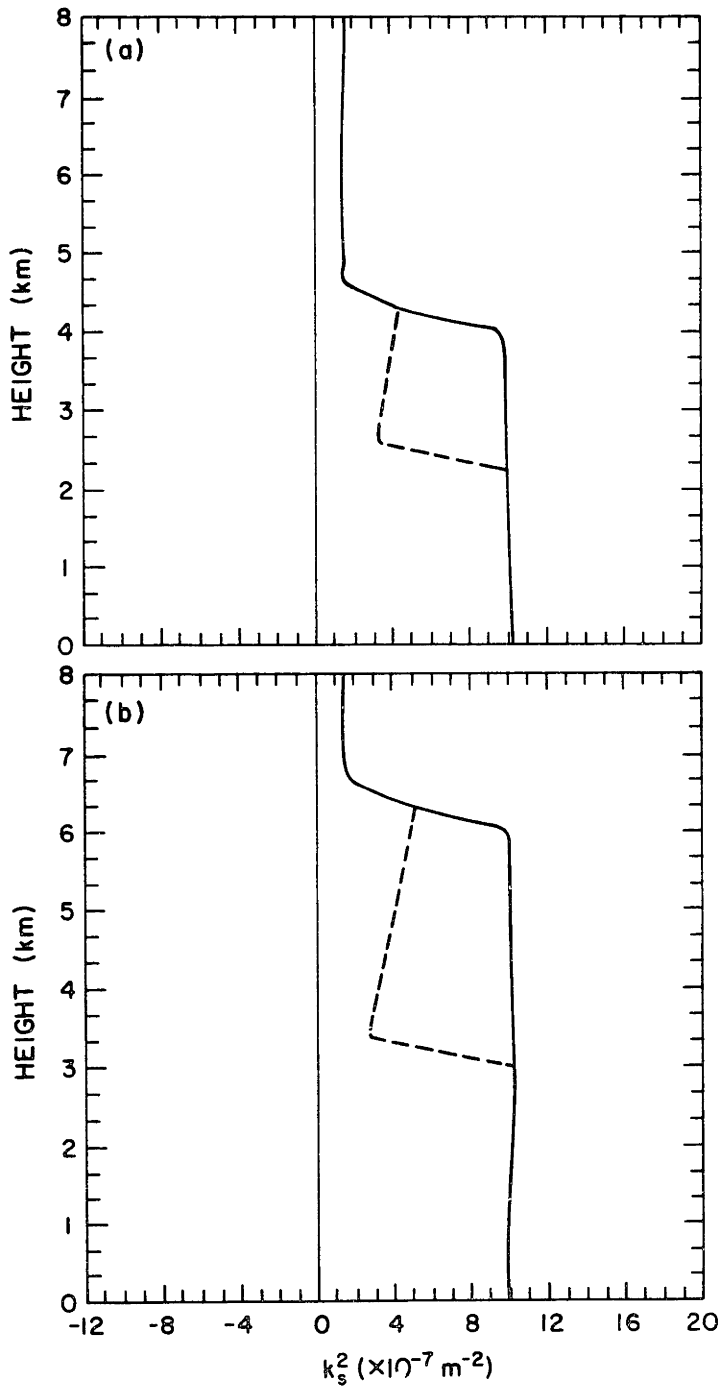

Figure 5.10. Scorer parameter profiles for atmosphere favorable for the development of dry trapped lee waves when the lowest layer is (a) 4 km, and (b) 6 km, deep.

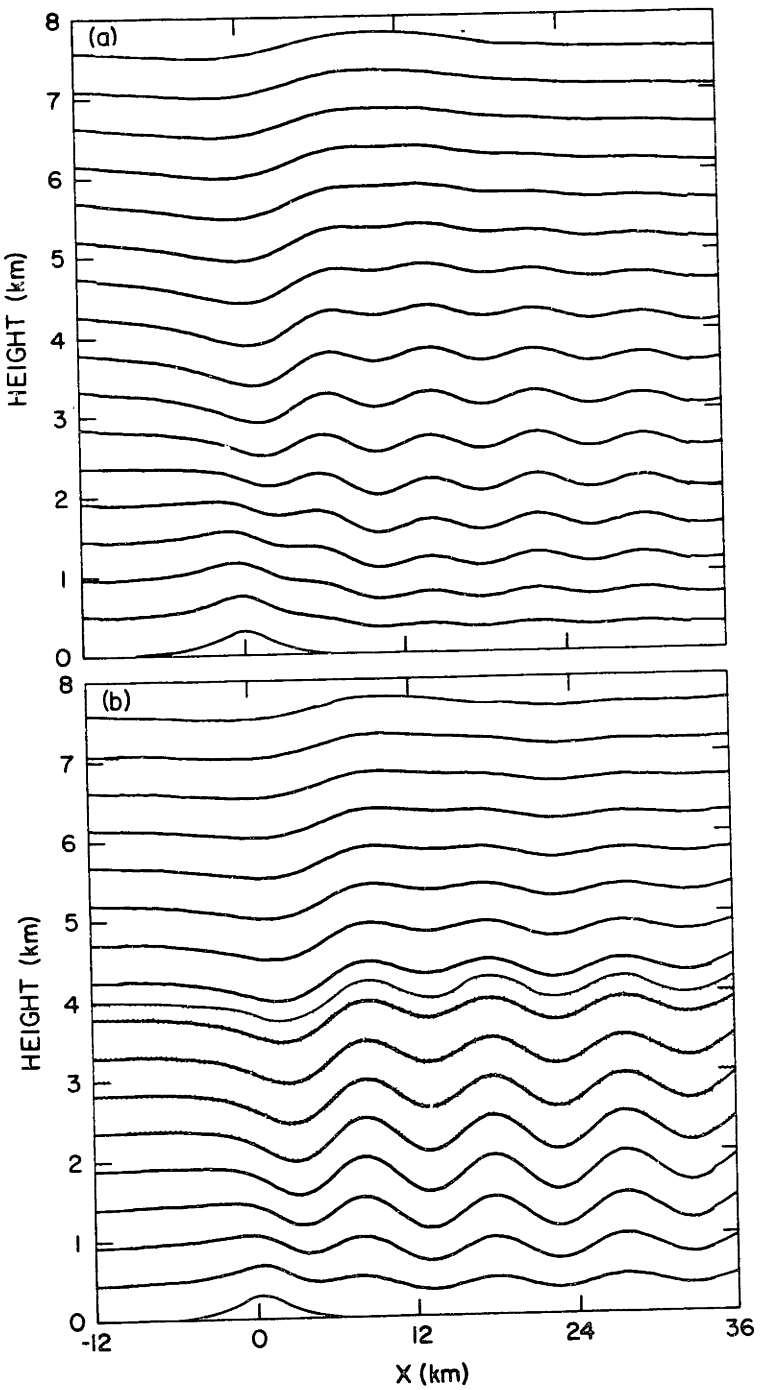

Figure 5.11. Streamlines produced by a 1 m high mountain by the atmosphere shown in Fig. 5.10a when the upstream flow is, (a) dry, and (b) saturated between the heights of 2.3 and 4 km. Cloudy regions are stipled. The streamline displacements are multiplied by 300 for display.

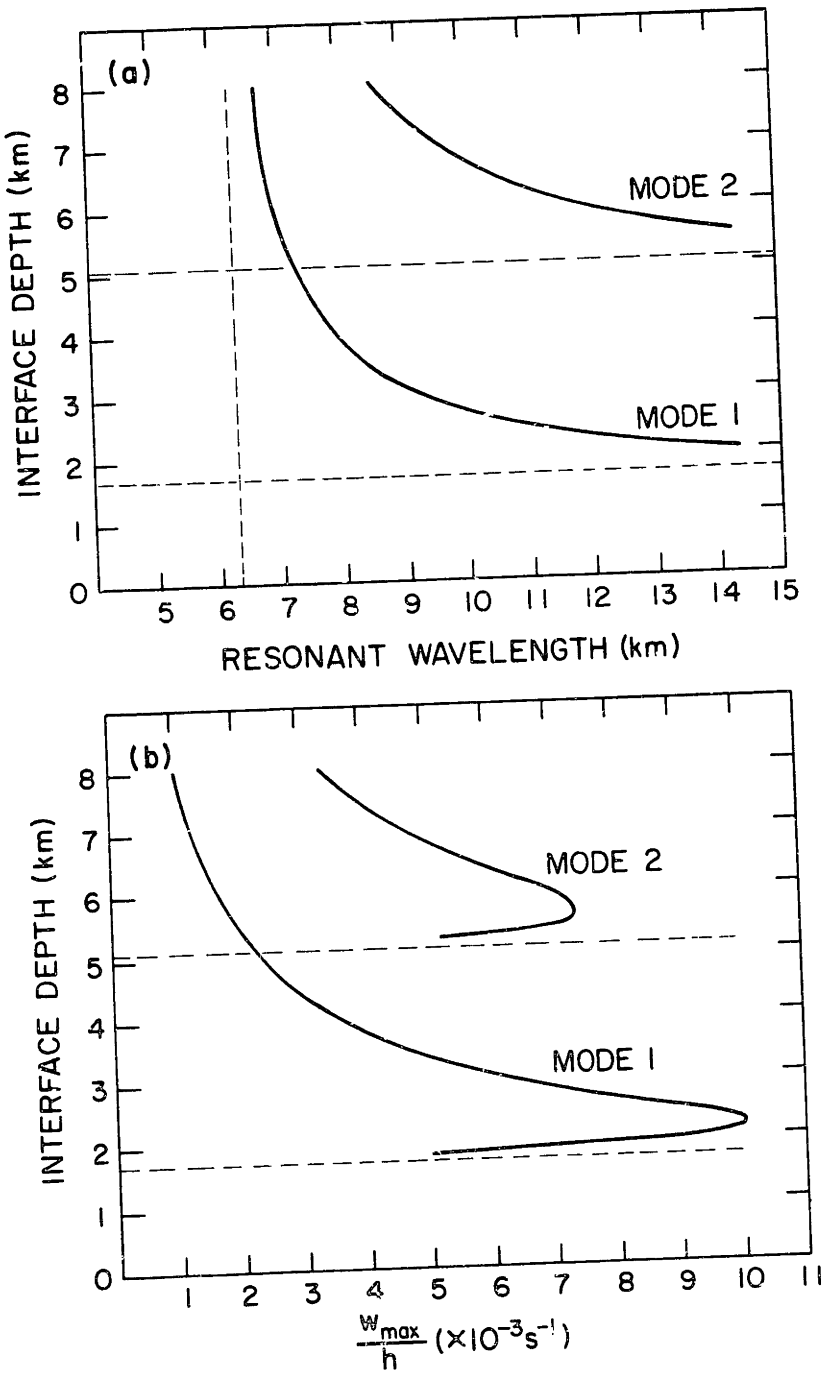

Figure 5.12. The influence of interface height on trapped lee wave (a) wavelength, and (b) amplitude, for the two lowest order modes; k_s^2 is 1.5×10^{-4} m^{-2} and 1.0×10^{-3} m^{-2} in the upper and lower layers, respectively. The amplitude calculations are for a Witch of Agnesi mountain with half-width 2.5 km.

modes. As predicted by Eq. (5.6), a minimum lower layer depth of 1.6 km is required to support mode one waves. A minimum depth of 5.1 km is necessary to support mode two waves. The amplitude of each mode peaks sharply at a depth just slightly greater than the cutoff value. When the atmosphere is capable of supporting both modes, the higher order mode dominates. Further discussion of the effects of changes in the dry atmospheric structure on resonant trapped waves may be found in Corby and Wallington (1956). If moisture is added to the top of a deep wave trapping layer in which the dry lee waves have a mode two structure, the interface depth can be lowered thereby eliminating the higher order mode and producing a weaker, shorter wavelength response. Figure 5.10b shows the k_s^2 structure in such a case, and Fig. 5.13a shows the dry linear lee waves which result. When the upstream flow is saturated and contains 0.2 g kg^{-1} of cloud between the heights of 3 and 6 km, as shown in Fig. 5.13b, the nodal line at 3.5 km disappears, and much weaker waves form in the lowest 3 km. The atmosphere appears to have a three layer structure with very weak short waves in the lowest layer, and stronger, longer waves in the middle moist layer. In the top layer the waves decay with height, but only 2 km of this region are shown in the figure, so the decay is not obvious to the eye.

A deep layer of high k_s^2 like the one just discussed (Fig. 5.10b) would be encountered only rarely in the real atmosphere. The shallower layer (Fig. 5.10a) is probably much more common, so in actual practice moisture at mid-tropospheric levels might be expected to slightly increase the amplitude of trapped lee waves.

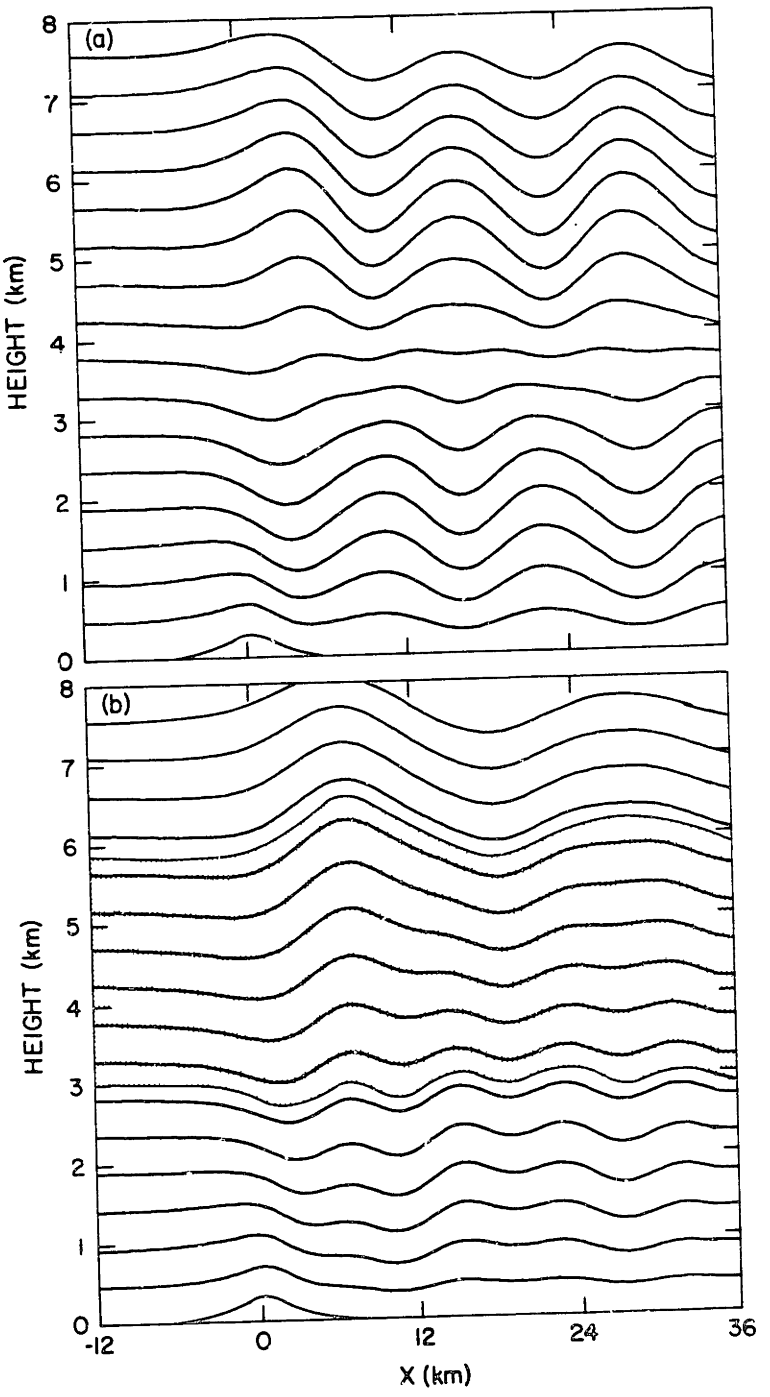

Figure 5.13. Streamlines produced by a 1 m high mountain by the atmosphere shown in Fig. 5.10b when the upstream flow is, (a) dry, and (b) saturated between the heights of 3 and 6 km. Cloudy regions are stipled. The streamline displacements are multiplied by 300 for display.

D. Practical Significance

In the preceding discussion we have often considered two limiting cases, which always produced significantly different lee waves. In the first case the flow is dry, and in the second case some horizontal layer remains saturated everywhere throughout the domain. In each of these situations the lee wave response can be estimated without explicitly modeling the details of condensation and evaporation. In linear flows it is possible to faithfully represent the effects of moisture by replacing saturated horizontal layers by dry layers in which the static stability is suitably reduced. In a nonlinear flow the same simple substitution, while not exactly correct, still allows a reasonable approximation. When the flow is just partially saturated, the effects of moisture can only be included by solving the complete moist thermodynamic equations.

The influence of moisture is greatest when the atmosphere is conditionally unstable, in which case an unsaturated lee wave can be destroyed by moist convection. Moisture also plays a significant role when the atmosphere is absolutely stable, but the effective saturated stability is low so that dry lee waves can be untrapped by an increase in humidity. In these situations the release of latent heat can have a rather dramatic effect on the waves even when the flow is only partially saturated, and an accurate dynamical model must include the complete moist thermodynamics. When changes in humidity serve only to tune or detune the trapped wave response, moisture plays a less fundamental role in the dynamics. In this case, if RH $<$ 100% in the upstream flow, a qualitatively correct solution can be obtained by ignoring moisture and solving the dry problem.

The preceding discussion has concentrated on simple two layer atmospheres. A variety of more complex structures could be examined which might provide more dramatic examples of the influence of moisture on trapped waves. Instead of attempting to construct an exhaustive catalog of interesting physical cases, we have concentrated on the basic physical behavior produced by the release of latent heat when a single wave trapping interface is present. The results are intended to serve as a basis for understanding more complicated situations. Nevertheless, the cases just discussed are representative of real atmospheric flows; it should be possible to qualitatively verify these results by observation.

VI. THE EFFECTS OF MOISTURE ON PROPAGATING MOUNTAIN WAVES

When stably stratified air flows over a large mountain barrier such as the Sierra Nevada in California, or the Front Range in the Colorado Rockies, gravity waves are produced with horizontal wavelengths on the order of 50 km. These mountain waves are too long to be trapped by the Scorer parameter values commonly encountered in the upper troposphere, so they propagate vertically into the stratosphere, where they eventually dissipate. The propagating waves generated by large mountains can extract a significant amount of momentum from the mean flow. Lilly (1978) has suggested that the drag produced by a strong propagating mountain wave has an effect on the earth's momentum budget comparable to that produced by a major mid-latitude cyclone. In contrast, Smith (1976) observed that the drag produced by trapped lee waves is often only a tenth of the drag associated with surface friction. Both trapped and propagating waves generate strong surface winds on the lee slopes of the mountain, but since propagating waves are usually associated with larger mountains, they are often responsible for the most severe downslope windstorms. In this chapter we will examine the effects of moisture on propagating mountain waves.

A. Small Amplitude Waves in an Atmosphere with Constant Wind and Stability

If the effects of compressibility on the Scorer parameter are neglected to obtain Eq. (5.1) (usually a good approximation), the

Scorer parameter will be constant in an atmosphere with constant windspeed and stability. In such a case, the streamline displacements in the linear hydrostatic wave produced by the mountain contour in Eq. (2.6) are given by Eq. (4.2). This wave propagates vertically; except for the effects of decreasing density it is periodic in the vertical with a wavelength of $2\pi/k_s$. The horizontal structure, which unlike the resonant wave case is not periodic, is determined by the mountain profile.

Figure 6.1 shows the streamline and perturbation horizontal velocities computed by the model for a dry flow in which $N = .0132\ s^{-1}$ and $\bar{u} = 20\ ms^{-1}$. The mountain contour is specified by Eq. (2.6) with $h = 1$ m and $a = 10$ km. In this simulation the domain contains 90 points in the horizontal and 66 levels in the vertical; the wave absorbing layer occupies the top 33 levels. The grid intervals are $\Delta x = 2$ km, $\Delta z = 333$ m; the large and small time steps are 20 and 5 seconds, respectively. The model is run until the solution reaches an essentially steady state (20000 to 30000 s after start-up). Figure 6.1 includes only the central portion of the domain, from $x = -60$ km to $x = 60$ km in the horizontal and $z = 0$ to $z = 11$ km in the vertical. The mountain peak is at $x = 0$.

Since the mountain height used in the computations is small, the influence of the nonlinear terms in the model equations is also small, and the solution obtained is approximately linear. The perturbations have been multiplied by 1000 for display; as such, they represent the linear solution for a 1 km high mountain. This case is similar to the test case presented in the first part of Chapter IV, except that in

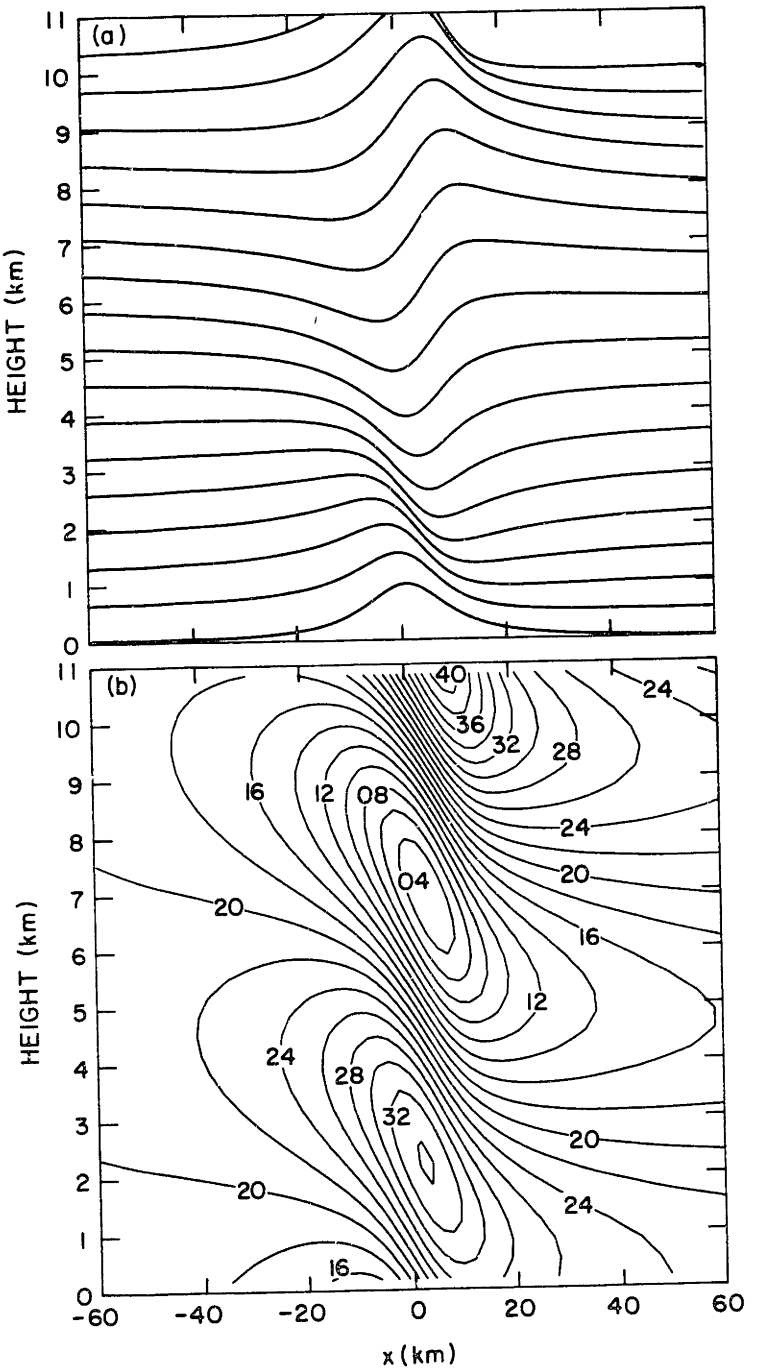

Figure 6.1. (a) Streamlines, and (b) horizontal velocities produced by a 1 m high mountain in a flow with constant windspeed and stability when RH=0% upstream. The perturbations are multiplied by 1000 for display, as such they constitute a linear numerical solution for a 1 km high mountain.

this instance the atmosphere is not isothermal so the dry stability is reduced from .0196 to .0132 s^{-1}.

Figures 6.2 and 6.3 show the waves produced in the same flow for cases where RH = 100% with 0.0 and 0.2 g kg^{-1} of cloud upstream. No rain is allowed in these runs so condensation and evaporation are reversible. A comparison of Figs. 6.1 through 6.3 shows that the moist waves are appreciably weaker than the dry wave. The differences in the horizontal windspeed maxima and minima are particularly pronounced. In an atmosphere with constant N and $\bar{u}$ the horizontal windspeed perturbations are proportional to N, so it is reasonable to expect the reductions in effective stability which occur in saturated regions to have a strong impact on the horizontal windspeed. The change in stability also has a large impact on the vertical wavelength, which in the case of constant N and $\bar{u}$ is $2\pi\bar{u}/N$. In the dry case the first vertical half-wavelength, the height at which the streamline contour is a mirror image of the mountain, is 4.7 km; it increases to 5.8 and 7.1 km in the partially cloudy and everywhere cloudy cases.

In the everywhere cloudy atmosphere shown in Fig. 6.3, the effective moist stability N_E (given by Eq. (5.8)), increases from .0062 s^{-1} at the surface to .0128 s^{-1} at a height of 10 km. This change in the stability occurs because the latent heat released when a saturated air parcel is lifted a given distance decreases as temperatures and water vapor concentrations decrease with height. Since N_E changes by a factor of two in almost 2/3 of a vertical wavelength, it is difficult to obtain accurate estimates of the

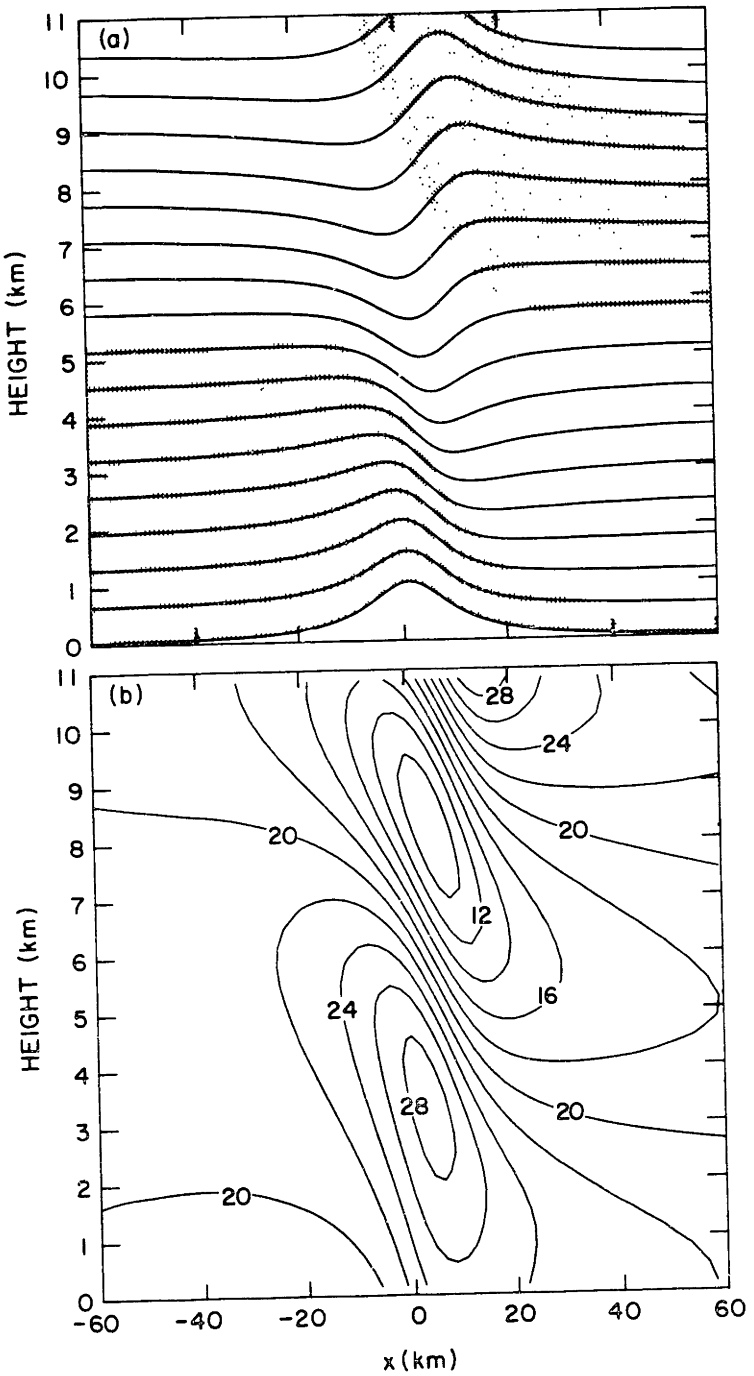

Figure 6.2. As in Fig. 6.1, except that RH=100% in the upstream flow. Cloudy regions are stipled.

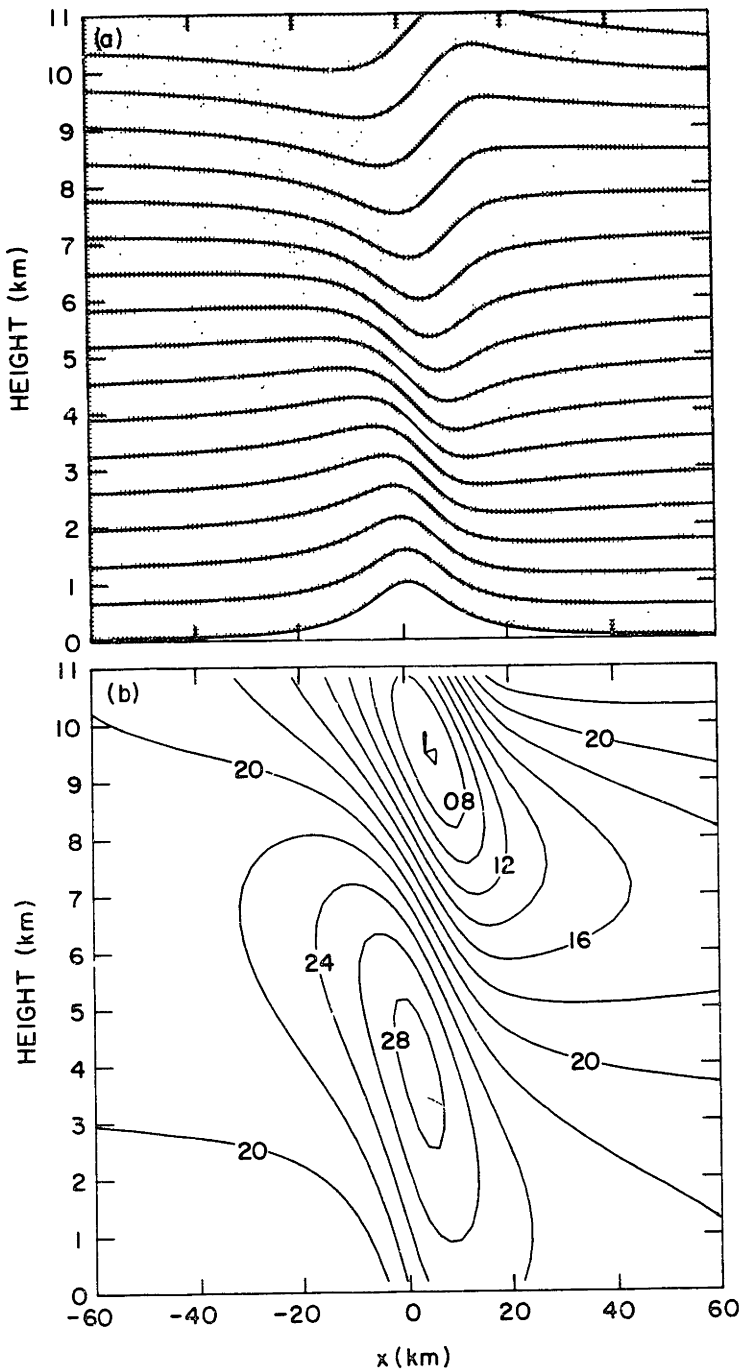

Figure 6.3. As in Fig. 6.2, except that RH=100% with 0.2 gm/kg of cloud in the upstream flow.

horizontal windspeed and vertical wavelength in the everywhere cloudy case by approximating N with N_E in a W.K.B. sense. A much better estimate can be obtained analytically for the effects of moisture on the momentum flux.

The analytic linear momentum flux for a hydrostatic wave produced by the mountain profile given by Eq. (2.6) in a dry atmosphere with constant N and $\bar{u}$ is

$$M_{LC} = \frac{\pi}{4} \rho_0 N \bar{u} h^2 \quad . \tag{6.1}$$

M_{LC} is independent of height. The momentum flux will remain independent of height even when N or $\bar{u}$ change abruptly in certain regions, but since partial reflections of the upward propagating wave energy can occur wherever there are strong gradients in the Scorer parameter, the flux magnitude cannot be calculated from Eq. (6.1). However, if N and $\bar{u}$ change smoothly so that no reflections occur, Eq. (6.1) can be applied using the surface values of N and $\bar{u}$. Using this approach with $N_E = .0062\ s^{-1}$ yields a prediction for a momentum flux in the everywhere cloudy case of 0.47 M_{LC}. Figure 6.4 shows the momentum fluxes produced in each of the simulations shown in Figs. 6.1 through 6.3; the fluxes have been normalized by M_{LC}. The dry flux is almost constant with height below the wave absorbing region (which begins at 11 km), and agrees well with its analytic value. The flux in the everywhere cloudy case (RH = 100%, $q_c = 0.2\ g\ kg^{-1}$) also agrees well with the previously predicted value of 0.47 M_{LC}. The flux is similarly reduced in the partially

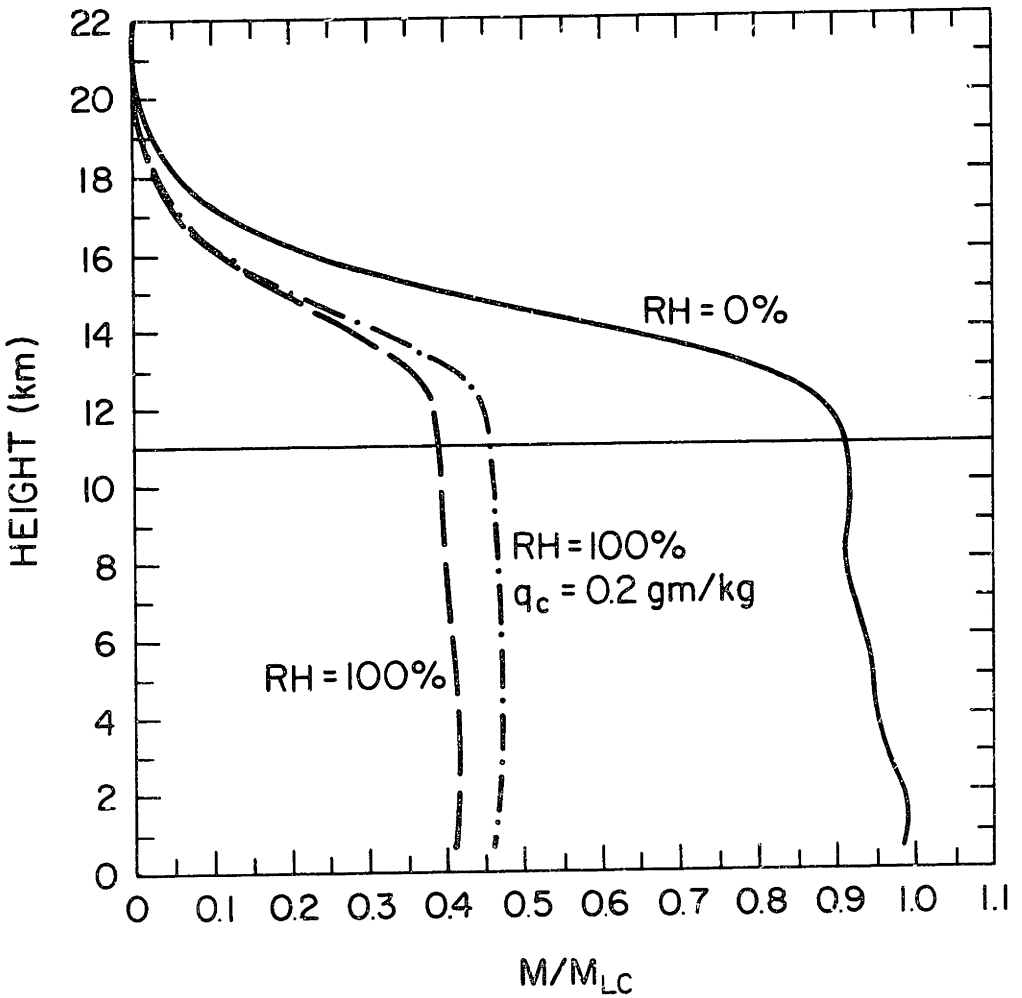

Figure 6.4. Vertical profiles of momentum flux produced for different upstream humidities by linear waves in an atmosphere with constant windspeed and stability. The fluxes are normalized by M_{LC}. The wave absorbing layer begins at 11 km.

cloudy wave. Note that the momentum fluxes are also constant with height in the moist cases, since the essential effect of reversible latent heating is only to change the stability.

With respect to momentum flux, streamline displacements, and horizontal windspeeds, the partially cloudy case is very similar to the everywhere cloudy case, and significantly different from the dry case. This is opposite to the result obtained for trapped waves where the partially cloudy waves resembled the completely dry waves more nearly than the completely cloudy ones.

B. Small Amplitude Waves in an Atmosphere with Constant Wind Shear and Stability

In the real atmosphere one seldom encounters vertical profiles in which the stability and windspeed are constant. In the following we continue to assume a constant dry stability, but allow the windspeed to increase realistically with height. The specified wind increases linearly from 15 to 35 ms^{-1} over a depth of 10 km. Above the 10 km level, which is a representative height for the tropopause, the windspeed remains a constant 35 ms^{-1}. Klemp and Lilly (1975) have obtained the steady state linear hydrostatic wave response for this type of flow by transforming the vertical coordinate

$$z + \eta = \frac{1}{\alpha} \ln (1 + \alpha z) \quad , \tag{6.2}$$

where u_0 is the surface windspeed and $\bar{u}_z = u_0 \alpha$. If the terrain

profile is specified by Eq. (2.6), the streamline displacements in the constant shear layer satisfy

$$\delta(x,z) = \left(\frac{\bar{\rho}}{\rho_0}\right)^{1/2} \frac{ha\, e^{-\alpha\eta/2}}{x^2 + a^2} \left(a \cos \mu\eta + (ab_R - b_I x) \sin \mu\eta\right) , \quad (6.3)$$

where

$$\left.\begin{aligned} b_R &= \frac{u_0^2\left(\mu^2 + \frac{\mu\alpha}{2}(\cot\phi - \tan\phi) - \frac{\alpha^2}{4}\right) - N^2}{u_0^2\left(\mu\cot\phi - \frac{\alpha}{2}\right)^2 + N^2} \cot\phi \ , \\ b_I &= \frac{\mu N u_0 (1 + \cot^2\phi)}{u_0^2\left(\mu\cot\phi - \frac{\alpha}{2}\right)^2 + N^2} \ , \\ \mu^2 &= \frac{N^2}{u_0^2} - \frac{\alpha^2}{4} \ , \quad \phi = \frac{\mu}{\alpha} \ell n \left(1 + \frac{\Delta u}{u_0}\right) \ , \end{aligned}\right\} \quad (6.4)$$

and Δu is the change in windspeed across the shear layer. Note that the vertical wavelength increases exponentially as a function of z in the shear layer. The associated momentum flux is

$$M_{LS} = \frac{\pi}{4} \bar{\rho}_0 \mu b_I u_0^2 h^2 \approx M_{LC}\left(1 + \left(\frac{1}{2} \sin 2\phi\right)\left(\frac{u_0\alpha}{N}\right) + O\left[\left(\frac{u_0\alpha}{N}\right)^2\right]\right) \quad (6.5)$$

M_{LC} is the flux produced by a constant windspeed of u_0. The approximate equality in Eq. (6.5) holds when the mean shear is small enough that the mean state Richardson number is much greater than 1. Details of the solution procedure may be found in Klemp and Lilly.

In the remainder of this investigation a wind profile with constant tropospheric shear will be used instead of a constant windspeed profile, since the constant shear assumption allows a better approximation of observed winds. In addition, in the constant shear case the Froude number ($\bar{u}/Nh$) and the vertical wavelength, both of which vary with height, are smallest in the lower troposphere. Thus, the flow is most nonlinear in that region of the atmosphere where water vapor concentrations are greatest and moisture effects most pronounced.

Figure 6.5 shows the streamlines and horizontal velocities produced by a dry flow with constant tropospheric shear. Note the weak waves which appear to the lee of the main wave. These waves are partially trapped due to the change in windspeed which forces the Scorer parameter to decrease with height. Similar waves have been observed in real atmospheric flows (see (Fig. 1.1). Except for the windspeed (and the large and small time steps which were reduced to 16 and 5-1/3 seconds, respectively), the physical and computational parameters for these runs are identical to those described in the previous section. As before, the computations were performed on a 1 m high mountain; the perturbations were then multiplied by 1000 to numerically obtain the linear solution for a 1000 m high mountain.

The influence of moisture on this flow is illustrated in Figs. 6.6 and 6.7 which show the streamlines and horizontal velocities that develop when RH = 100% with 0.0 and 0.2 gm/kg of cloud in the upstream flow. As in the constant wind case, the presence of moisture reduces the streamline displacements and the perturbation horizontal

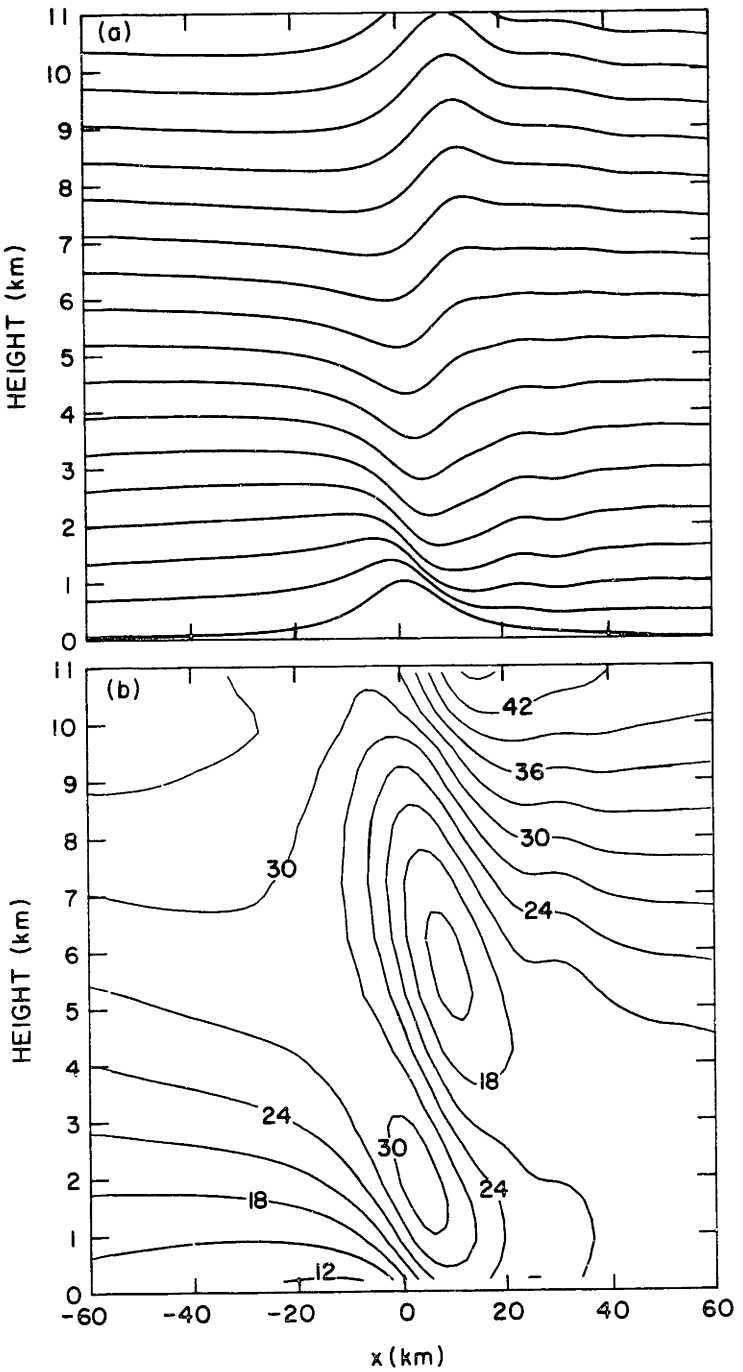

Figure 6.5. (a) Streamlines, and (b) horizontal velocities produced by a 1 m high mountain in a flow with constant stability and tropospheric wind shear when RH=0% upstream. The perturbations are multiplied by 1000 for display, as such they constitute a linear numerical solution for a 1 km high mountain.

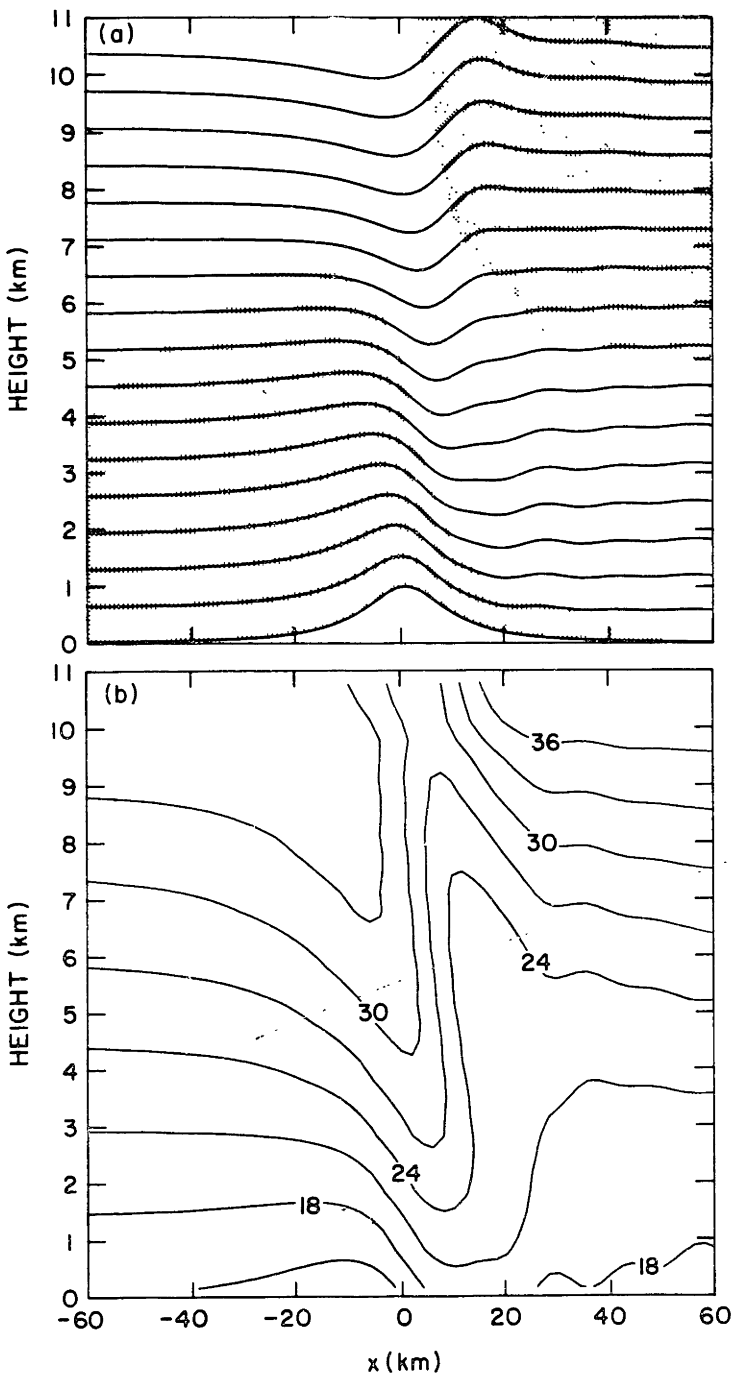

Figure 6.6. As in Fig. 6.5, except that RH=100% in the upstream flow. Cloudy regions are stipled.

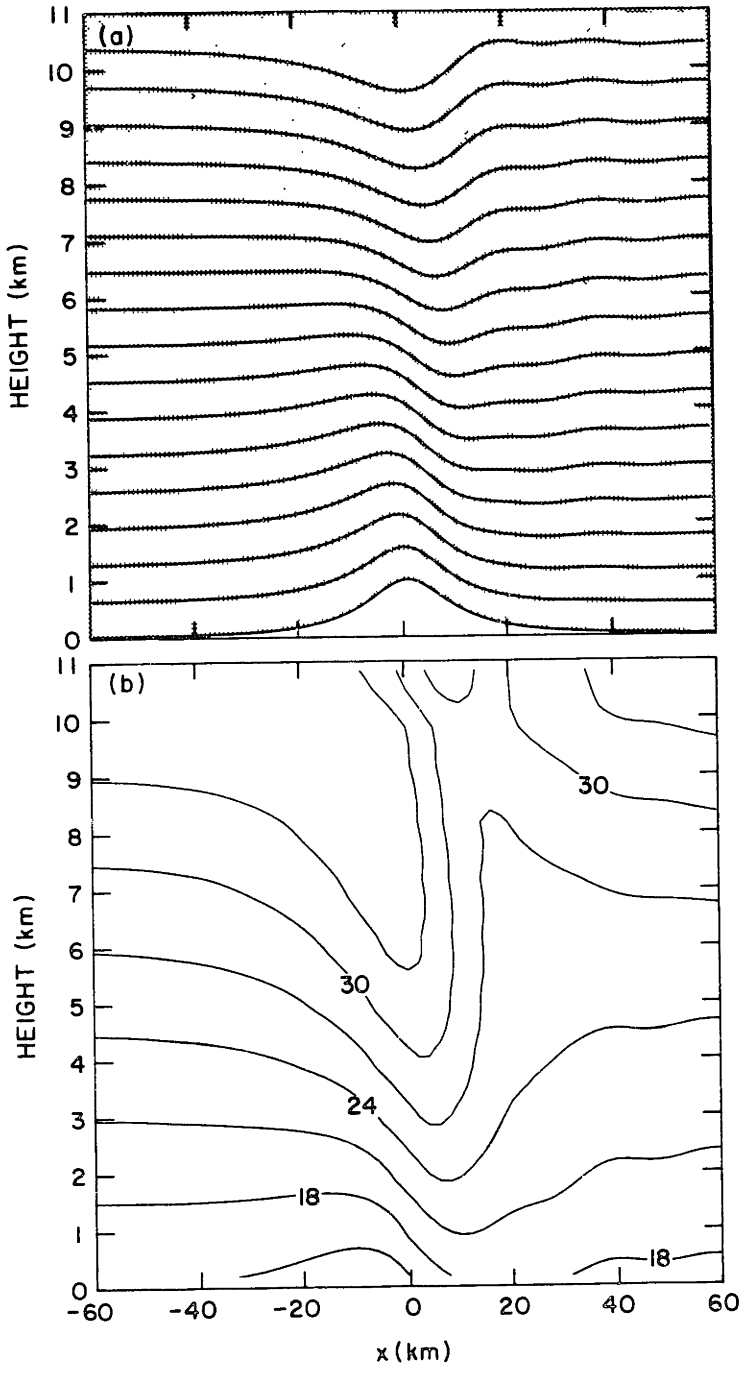

Figure 6.7. As in Fig. 6.6, except that RH=100% with 0.2 gm/kg of cloud in the upstream flow.

windspeeds, and increases the vertical wavelength. However, in this case the changes are slightly more pronounced. As an example, the vertical half-wavelength increases from 4.5 km in the dry flow, to 6.5 and 8.5 km in the partially cloudy and completely cloudy flows.

The momentum flux profiles for these runs are shown in Fig. 6.8. As before, there is no precipitation so condensation and evaporation only act to change the effective stability, and the flux profiles are constant with the height below the wave absorbing region. The fluxes are nondimensionalized by M_{LC}; so the dry analytic flux has a scaled value 0.93 according to Eq. (6.5). The partial reflection produced by the discontinuity in wind shear at the tropopause is sufficient to reduce the momentum flux 7% from its value in a constant property atmosphere. The flux for the everywhere cloudy case, estimated by replacing N with N_E = .0062 s^{-1}, has a scaled value of 0.40. These numbers agree with the numerical results in Fig. 6.8 very well. As before, the moist fluxes are less than half the dry value, and the partially cloudy case is much more similar to the completely cloudy case than the completely dry case.

We have seen that the presence of moisture can strongly modify the vertical wavelength. Klemp and Lilly (1975) have shown that linear hydrostatic waves experience strong amplification in three-layer atmospheres where the phase shift across each of the two lowest layers is nearly one quarter wavelength. A three-layer atmosphere is often a good idealization of the actual upstream profile during strong mountain wave events, so this amplification process may have a significant effect on real atmospheric waves. The ability of

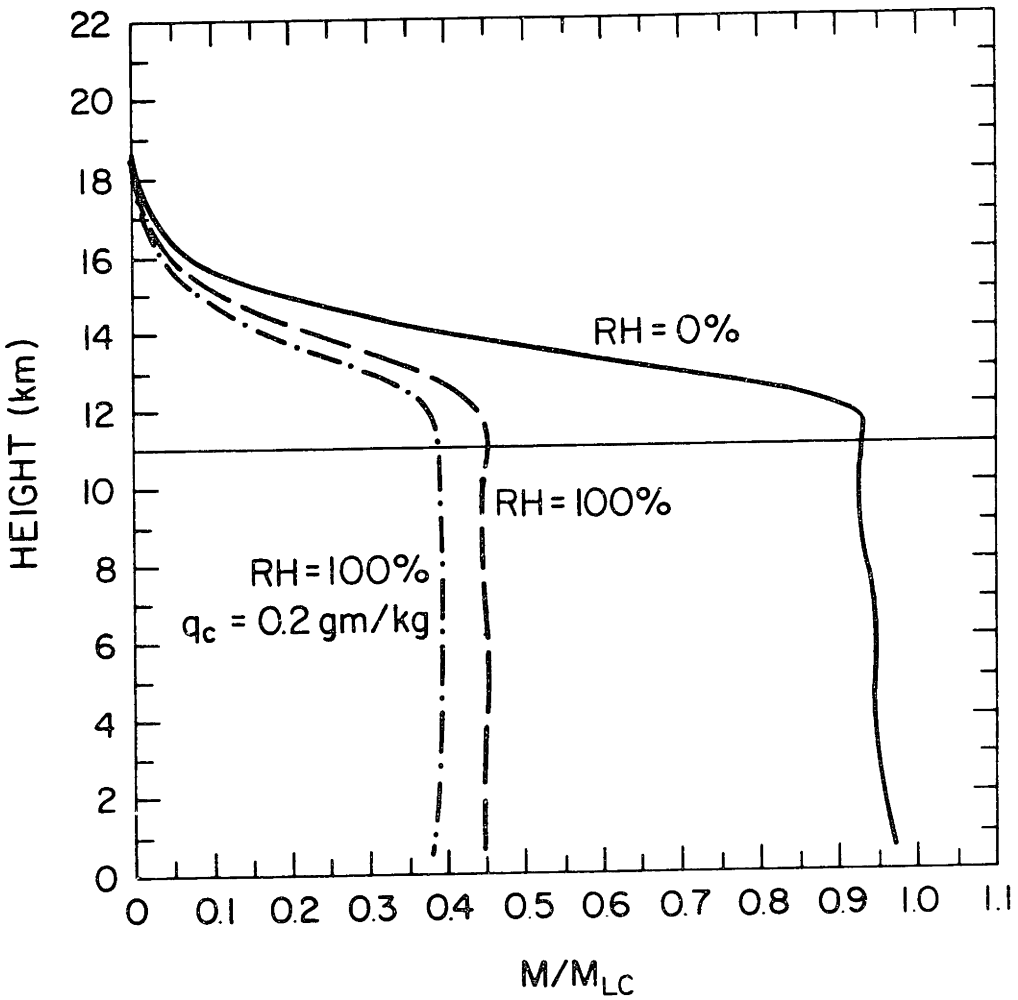

Figure 6.8. Vertical profiles of momentum flux produced for different upstream humidities by linear waves in a flow with constant stability and tropospheric wind shear. The fluxes are normalized by M_{LC}. The wave absorbing layer begins at 11 km.

moisture to alter the vertical wavelength, especially in the lowest layer, should allow it to tune or detune the three-layer structure, and significantly affect the mountain wave response. The influence of moisture in such three-layer atmospheres was tested, and it appears to be important. However, the flow in conditions favorable for a strong wave response often does not reach a steady state because the wave moves off the mountain and drifts downstream like a weak hydraulic jump. It seems possible to stop the downstream drift by appropriately including the effects of surface friction, but a careful treatment of the boundary layer in mountainous terrain is beyond the scope of this thesis. We therefore limit our investigation to flows in which the neglect of surface friction does not appear to have a fundamental impact on the wave dynamics.

C. Finite Amplitude Waves in an Atmosphere with Constant Stability and Wind Shear

Although they can produce useful results, small amplitude flows are not the best situations in which to examine moisture effects, since they produce only very small displacements. As a consequence, they respond identically to flows in which RH = 0% and RH = 99% upstream. In the following, we will examine the behavior of moisture in waves which produce realistic vertical displacements. Consider again the atmosphere with constant wind shear and stability described in the previous section, and increase the mountain height to 1 km. All other physical and computational parameters are unchanged. Four different upstream moisture profiles are examined; dry, RH = 80%,

RH = 100%, and low level cloud. The low level cloud case is representative of the wettest realistic moisture profiles which might be commonly encountered upstream of a mid-continental mountain range. In this case the air upstream contains 0.2 g kg^{-1} of cloud between the heights of 667 and 3000 m; the relative humidity drops smoothly to zero 1 km above and below the cloud. The streamlines and horizontal velocities produced by each of these flows are shown in Figs. 6.9 and 6.10. Note that the nonlinear dry wave is stronger than its linear counterpart (Fig. 6.5). The steepening of the wave fronts in the dry nonlinear wave (Fig. 6.9a) is in accord with the prediction of Miles and Huppert (1969). Further discussion of the steepening of nonlinear mountain waves may be found in Smith (1977), Lilly and Klemp (1979), and Peltier and Clark (1979). As in the linear case, the addition of moisture to the wave weakens it, but in the finite amplitude case the damping effect is stronger. The influence of moisture is noticeable in the RH = 80% case, and very important in the RH = 100% and low cloud cases.

The momentum flux profile associated with each of these wave regimes is plotted in Fig. 6.11. Although the fluxes are approximately constant with height below the wave absorbing region, small, long wavelength oscillations in its magnitude are visible in the RH = 0% and RH = 80% cases. These variations may be caused by a slight nonsteadiness of the solution, by weak reflections from the wave absorbing layer, or by the finite integration limits (±9a) used in the momentum flux calculations. In these nonlinear waves, the dry momentum flux is 50% larger, and the flux for the RH = 100% case is

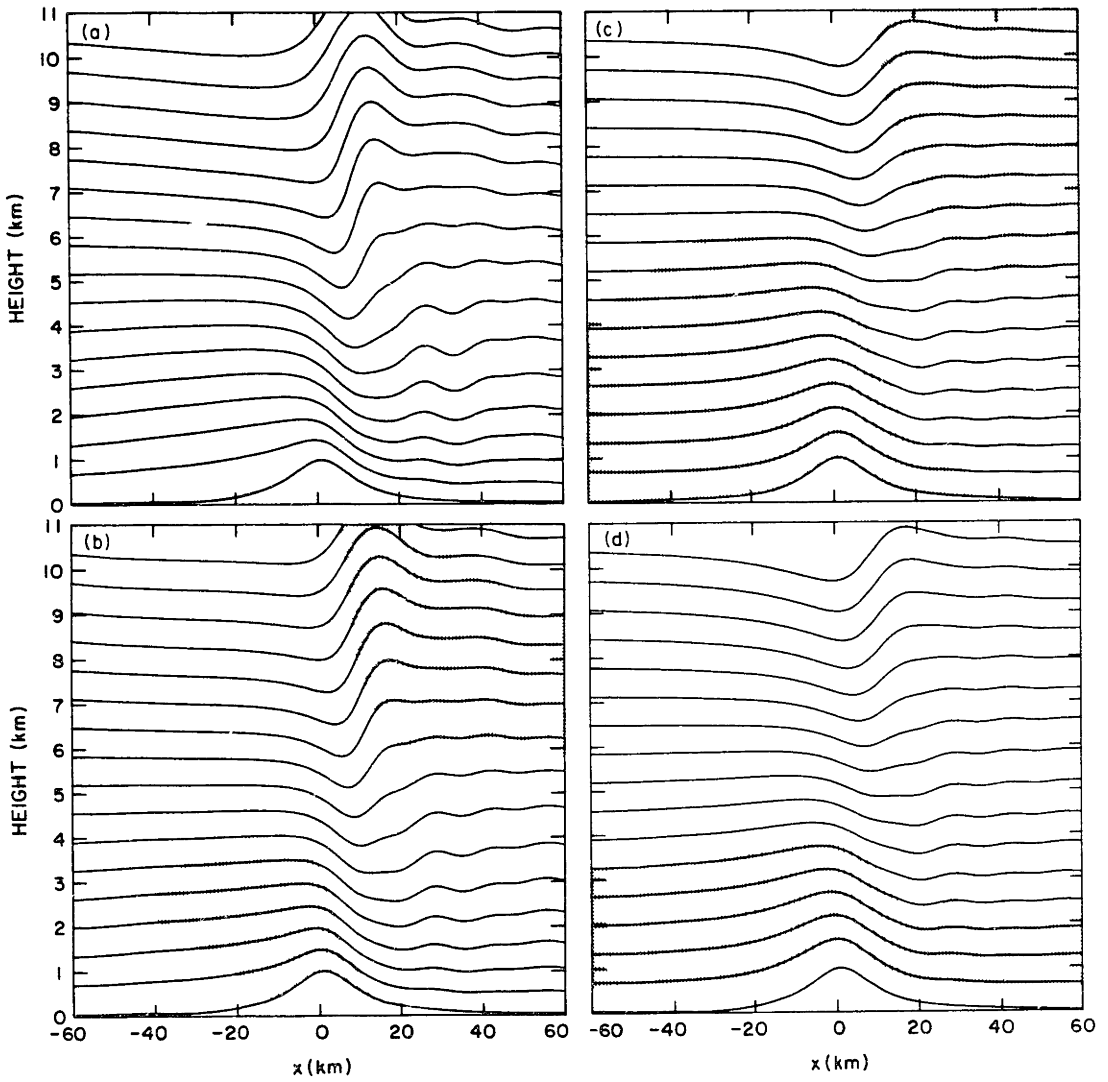

Figure 6.9. Streamlines produced by a 1 km high mountain in a flow with constant stability and tropospheric wind shear for upstream moisture profiles in which (a) RH=0%, (b) RH=80% everywhere, (c) RH=100% everywhere, and (d) low cloud lies between the heights of 667 m and 3000 m. Cloudy regions are stipled.

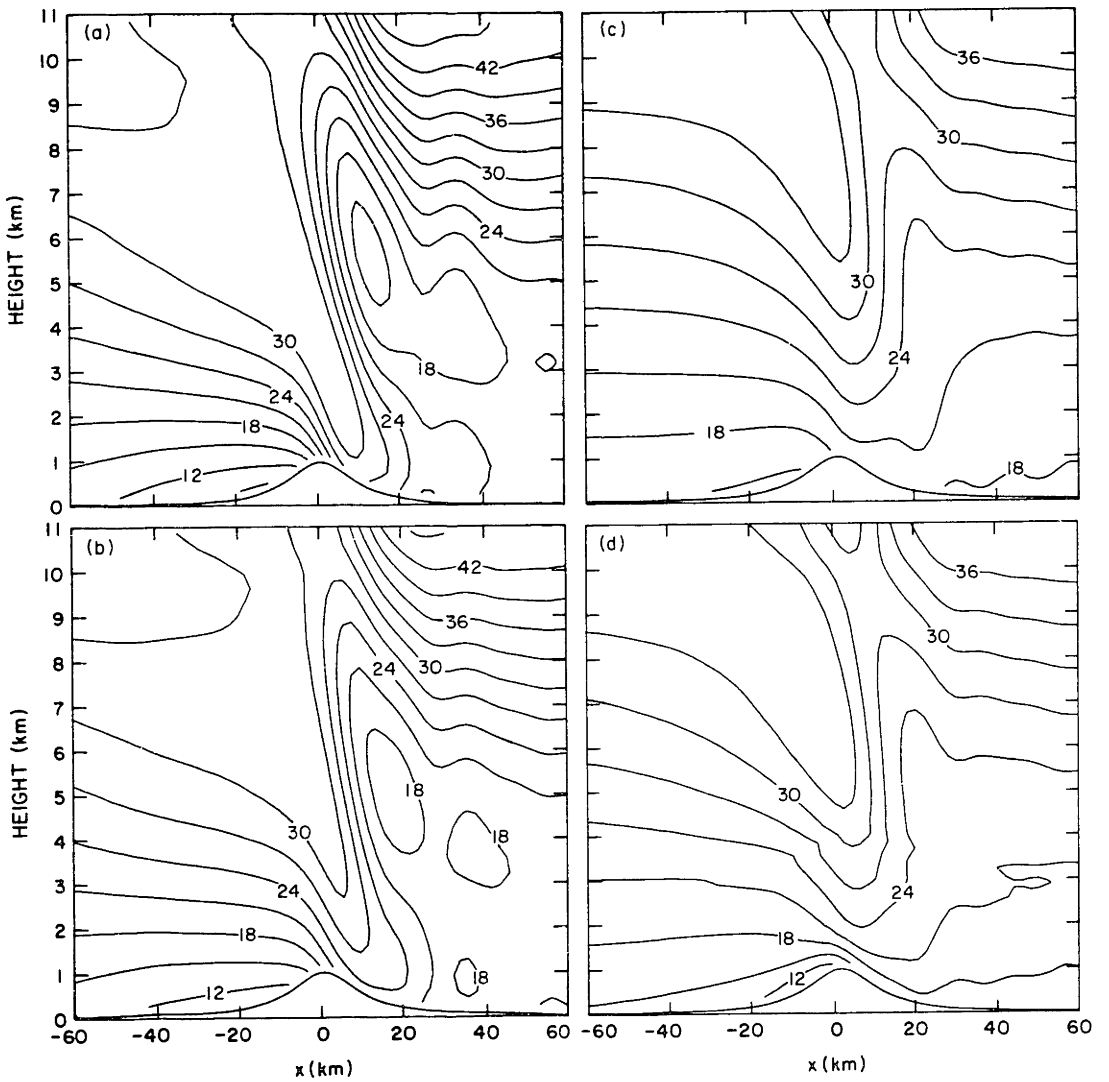

Figure 6.10. As in Fig. 6.9, except the variable displayed is horizontal windspeed.

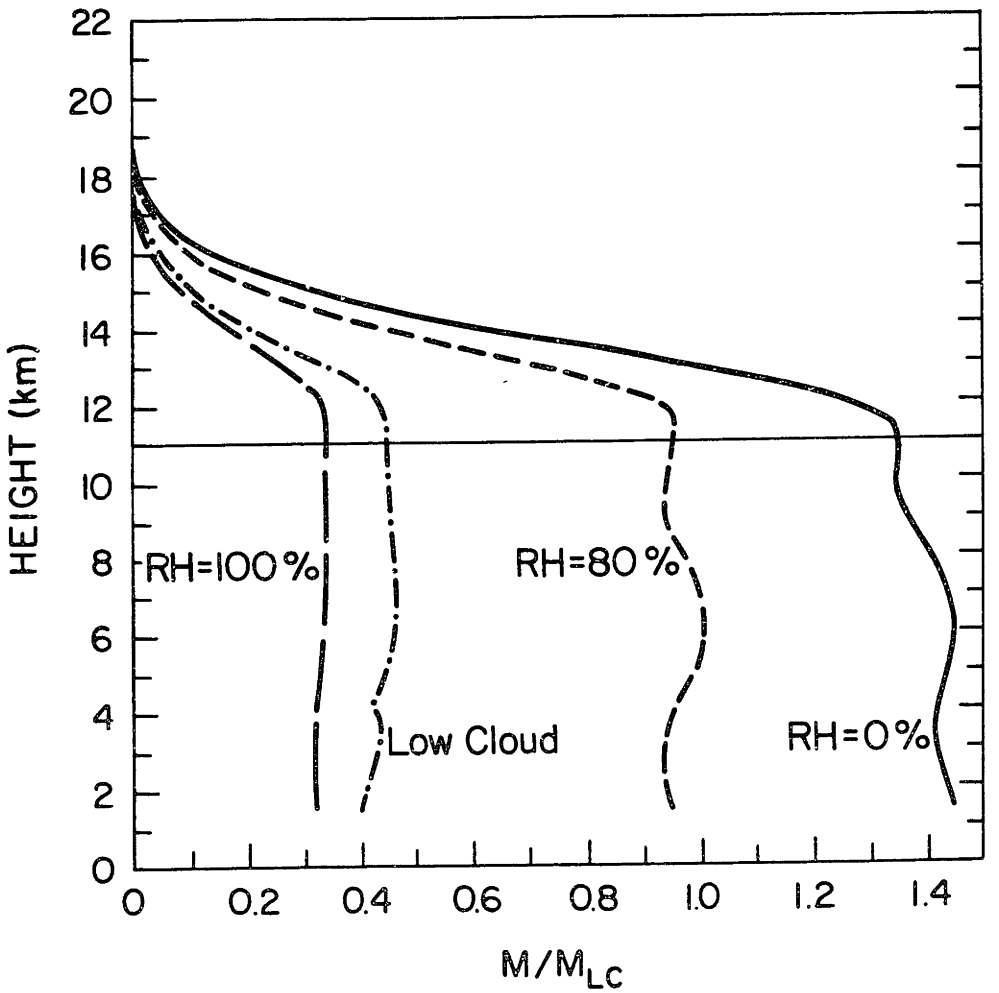

Figure 6.11. Vertical profiles of momentum flux produced for different upstream humidities by finite amplitude waves in a flow with constant stability and tropospheric wind shear. The fluxes are normalized by M_{LC}. The wave absorbing layer begins at 11 km.

30% smaller, than the fluxes in the corresponding linear waves. The presence of moisture appears to have a greater impact on the momentum flux in finite amplitude waves. In this instance a total flux reduction of 75% is produced when the upstream flow is just at saturation. When the upstream relative humditiy is only 80%, the momentum flux produced by the partially saturated wave is 2/3 the flux for a dry flow, showing that comparably small amounts of moisture can significantly influence the wave drag.

In the preceding, the clouds have not been allowed to precipitate, in which case the microphysics are reversible and the practical effect of moisture is to decrease the stability in the saturated regions. In principle, the moist flow could be calculated by replacing the clouds with regions of suitably reduced stability and solving the dry problem. Barcilon et al. (1978) have taken such an approach and found that in their small amplitude calculations, low level moisture could reduce the wave drag by up to 50% in an atmosphere with constant wind and stability. Their estimate is consistent with the small amplitude results presented here. In finite amplitude waves even stronger wave drag reductions are possible.

D. The Importance of Precipitation

The strong downslope winds produced by mountain lee waves are often accompanied by a large increase in surface temperature. Early investigators attributed this to the latent heat released irreversibly by precipitation deposited near the mountain summit. Later studies have shown that a surface temperature rise can be produced by dry

dynamics alone, and have tended to de-emphasize the importance of precipitation. In this section we will describe the influence of precipitation on the mountain waves examined in the last section.

The RH = 100% and low cloud simulations discussed in the previous section, are repeated with the rain parameterization (see Chapter III) turned on. All the rain falls from the cap cloud which impinges on the mountain peak; no rain forms in any of the wave clouds. In the case where RH = 100% everywhere upstream, there was a maximum rainfall rate of 5.4 mm hr^{-1} just to the lee of the mountain crest; the average rainfall rate at elevations above 500 m (half the height of the summit) was 2.9 mm hr^{-1}. In the low cloud case the corresponding maximum and average rates were 6.1 and 3.6 mm hr^{-1}. The maximum occurred 10 km upwind from the crest, with a secondary maximum just to the lee of the crest. These are heavy, but not unrealistic, precipitation rates. The RH = 100% case was run a second time with the microphysics replaced by the assumption that liquid water rains out instantly after condensation; then there is no evaporation and the flow experiences the maximum net heating.

The momentum fluxes for the low cloud and RH = 100% cases are shown in Fig. 6.12. The momentum flux is not calculated at levels below the mountain height where the horizontal integral of u'w' would pass through the terrain. However, the pressure drag across the mountain

$$M_p = -\int_{-\infty}^{\infty} p \frac{dz_s}{dx} dx \quad , \tag{6.6}$$

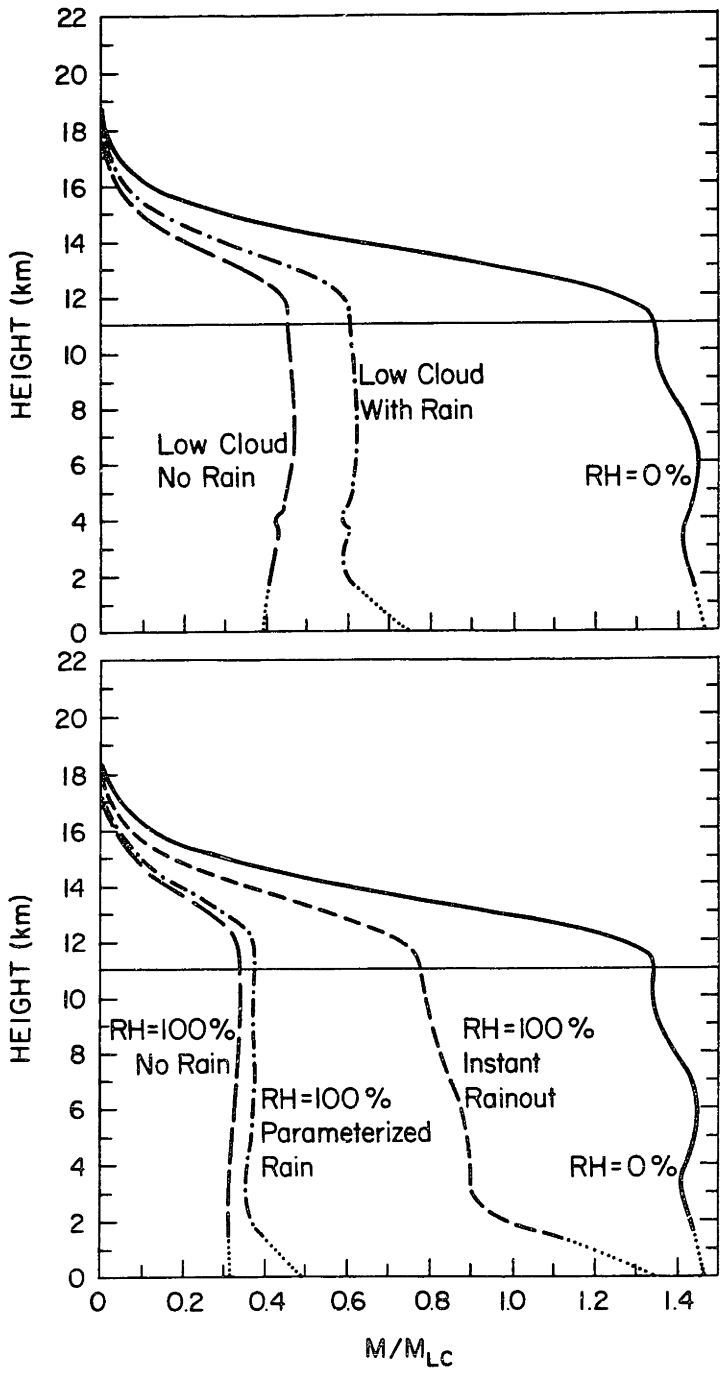

Figure 6.12. The effects of rain on the vertical profiles of momentum flux produced by upstream moisture profiles in which (a) there is low cloud between the heights of 667 m and 3000 m, and (b) RH=100% everywhere. The fluxes are normalized by M_{LC}. The pressure drag associated with each wave is plotted at z=0, and connected to the appropriate momentum flux profile by a dotted line. The wave absorbing layer begins at 11 km.

is computed at the surface. The pressure drag produced in each of the previous cases is plotted at ground level in Fig. 6.12 and connected to the corresponding momentum flux profile by a dotted line. Although it is not explicitly calculated as such, a value on the dotted line represents the momentum flux integrated along a horizontal level interrupted by the terrain plus the surface pressure drag across that portion of the mountain which extends above the level of integration.

The Eliassen-Palm theorem states that in the absence of dissipation and diabatic heating, the momentum flux should be constant with height. However, when precipitation occurs there is net heating, and in the lowest 2 or 3 km, where this heating is present, the flux is not constant with height. Except in the instant rain-out case, in which there is also net heating at higher levels, the momentum flux is constant with height above 3 km. In the low cloud case (Fig. 6.12a), the mid-tropospheric momentum flux produced when precipitation is present is 50% stronger than when it is absent, but it is still less than half the value calculated when the flow is dry. In the RH = 100% case (Fig. 6.12b), the "realistic" rain parameterization produces only a slight increase in the momentum flux beyond that in the no rain case, but when condensed water is rained out instantly, the increase is very large (up to a factor of 3 near mountain top level). However, even the fluxes produced with instant rain-out are weaker than those in the dry wave.

Smith and Lin (unpublished manuscript) have investigated the response of linear hydrostatic mountain waves to regions of specified heating and cooling. They found that heating produces a disturbance

in the pressure field which can interact with the topography to increase or decrease the low level momentum flux and surface pressure drag depending on the phase of the induced pressure perturbation at the ground. The net effect on the drag is thus a function of the relative position of the mountain peak and the heating regions. It is difficult to directly apply their results to the complicated heating and cooling regions produced by these flows, and we will not attempt to do so here. Instead we will concentrate on the qualitative changes produced by precipitation in the low cloud case, a representative and hopefully realistic situation.

The streamlines, horizontal velocity and heating fields for the low cloud case are shown in Figs. 6.13 through 6.15. While the precipitating flow is still much weaker than the dry flow, it is significantly stronger than the nonprecipitating flow. Note in particular the increase in low level windspeed on the lee side of the terrain.

In an actual foehn wind, the air arriving at the base of the lee slope is usually warm and dry. It is interesting to note in Fig. 6.13 that the cap cloud looks much more realistic in the precipitating case because the cloud droplets, which otherwise sweep down the lee slope, are rained out. The absence of lee side cloud may have a major influence on the wave dynamics, since the stability in that region is greatly increased when the air is unsaturated. A second difference between the precipitating and nonprecipitating cases, which may have a major influence on the dyanmics is shown in Fig. 6.15. The cooling region in the descending part of the cap cloud is more concentrated, and locally more intense, when rain is present.

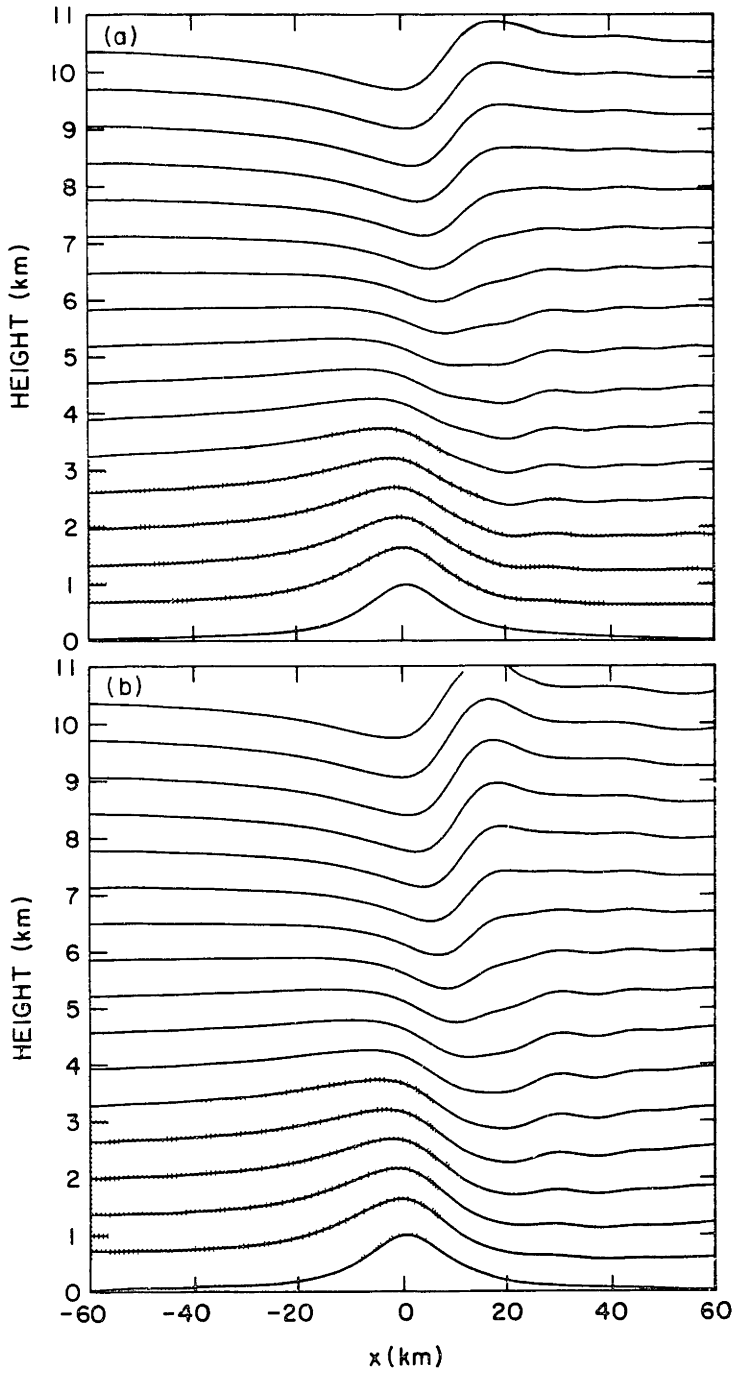

Figure 6.13. Streamlines produced by a 1 km high mountain in a flow with constant stability and tropospheric wind shear, and low cloud upstream (a) when no rain is allowed, (b) when rain is allowed.

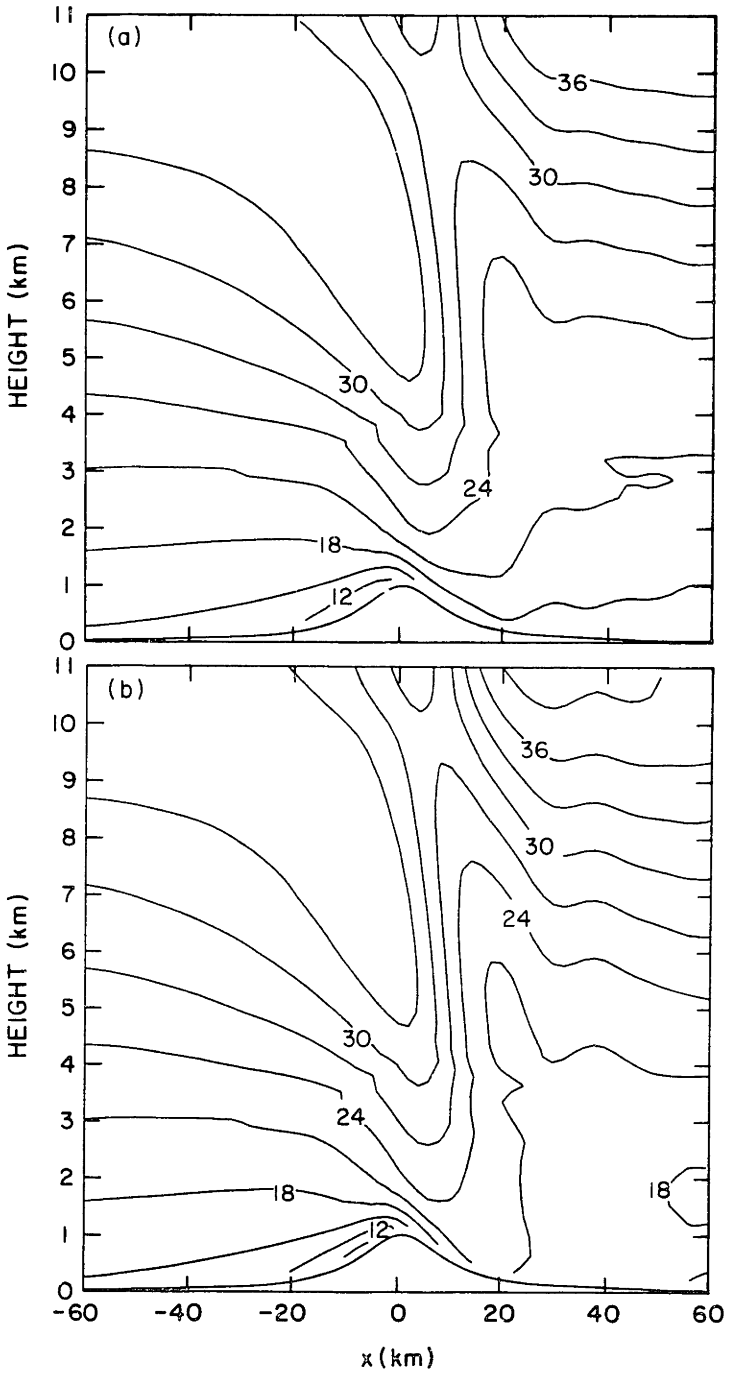

Figure 6.14. As in Fig. 6.13, except the variable displayed is horizontal windspeed.

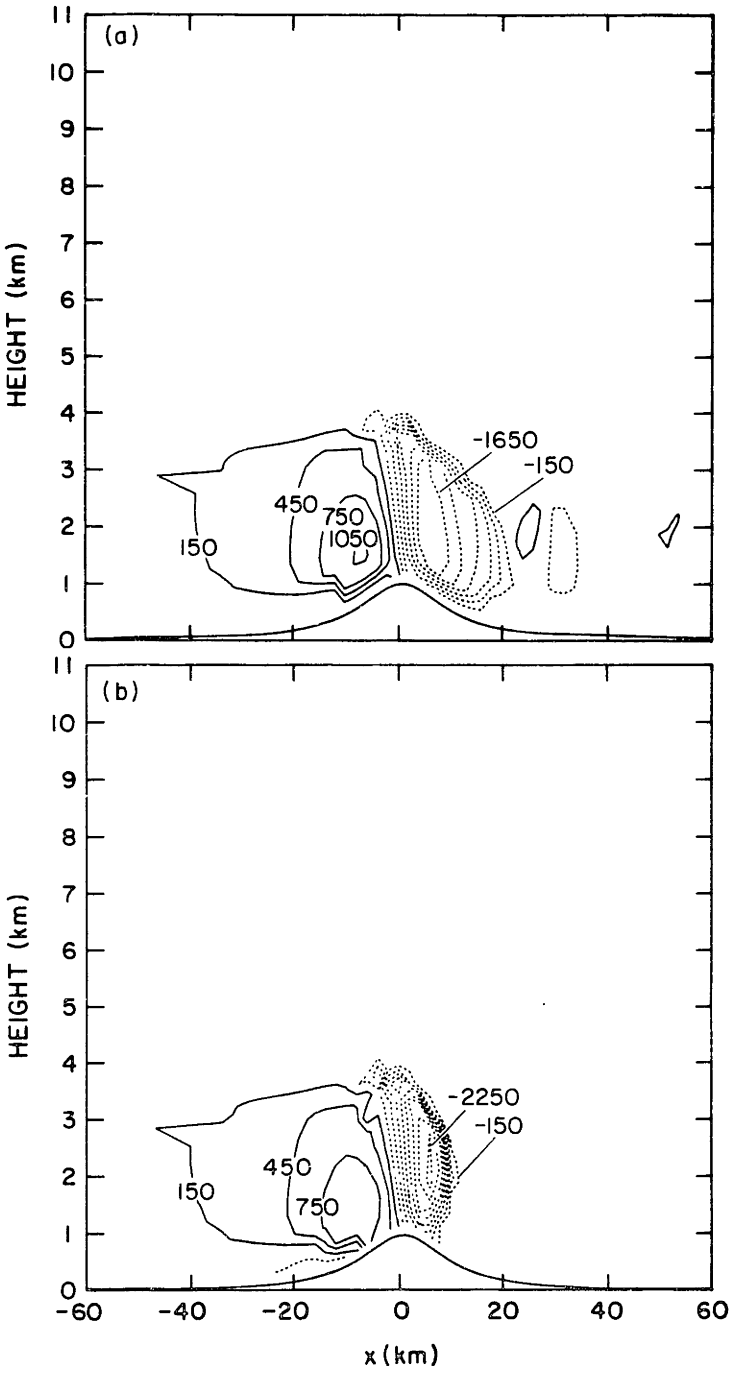

Figure 6.15. As in Fig. 6.13, except the variable displayed is the heating rate due to condensation and evaporation in watt-m/kg. In (a) the velocity weighted integral of the heating along a streamline is zero.

Although there is net heating only in the precipitating case, the total heating over the windward slope of the mountain is actually slightly reduced when rain occurs (Fig. 6.15). This is consistent with the results of Smith and Lin who predicted that uncompensated heating should locally reduce the upward streamline displacements, and thus reduce the forcing which produces the heating. In a case such as this, where stable layers are mechanically lifted by the mountain, this negative feedback is not nearly sufficient to entirely eliminate the uplift.

Barcilon et al. (1980) have examined linear hydrostatic mountain waves in an atmosphere with constant wind and dry stability. In their calculations, condensed water is rained out immediately. The heat released is assumed to produce only a small perturbation on the flow so that the cloud boundaries are determined by the dry solution. They found that irreversible latent heat release near mountain top level produced a pressure drag slightly larger than that obtained in the dry case. In the previous runs, when precipitation was allowed, the moist waves were consistently stronger than their nonprecipitating counterparts, but never as strong as the dry wave. When the realistic rain parameterization is used, the precipitating waves were less than half as strong as the dry wave. Only in the instant rain-out case did the wave amplitude and drag approach that in the dry flow. This is different from Barcilon's result, but since we have examined a somewhat different situation (nonlinear waves in constant shear instead of linear waves in a constant wind), this may merely reflect the variety of ways in which precipitation can affect different

mountain wave flows. However, it does seem likely that the instant rain-out assumption significantly exaggerates the influence of precipitation.

E. Conclusions

We have examined the effects of moisture on propagating mountain waves. In the cases considered, the dry Scorer parameter did not change abruptly with height so partial downward reflections of wave energy did not occur. In a future study, it would be interesting to examine the ability of moisture to tune or detune propagating mountain waves in multi-layer atmospheres. However, the basic nonreflective cases presented here are more useful for a first investigation because they are simple, yet realistic, situations.

In these nonreflective cases, when precipitation is not present clouds act to damp the waves and reduce the momentum flux. This effect is stronger in finite amplitude waves than in their small amplitude counterparts. When precipitation occurs, the wave amplitudes and momentum fluxes are stronger than those produced by nonprecipitating flows, but still significantly weaker than in the dry case. The investigation of precipitation effects was limited to moisture profiles where the relative humidity upstream was uniform with height, or concentrated in low level clouds. Other behaviors might be produced by different moisture distributions, but since the temperature, and hence the potential for large amounts of latent heating, decreases rapidly with height in the real atmosphere, the profiles considered may be the most physically significant.

VII. CONCLUSION

In the preceding chapters the effect of moisture on the dynamics of mountain lee waves has been investigated by numerical simulation. The numerical model, which was originally designed to simulate convective storms, was modified for lee wave calculations and tested to verify its accuracy. The model seems capable of simulating linear and moderately nonlinear mountain waves quite well, but its ability to faithfully calculate the wave response in very nonlinear conditions (particularly when the wave breaks) has not been demonstrated. In this thesis we have considered only those situations to which the model can be applied with confidence, the linear and moderately nonlinear mountain waves. In the actual atmosphere, most mountain wave activity probably occurs at moderately nonlinear wave amplitudes, so this restriction does not significantly reduce the applicability of the results. However, the strongest and most important mountain wave events may be associated with wave breaking, so further study of the dynamics of moist and dry breaking waves seems warranted.

Moisture appears to affect trapped lee waves in several ways. When moisture is introduced into the lowest layer of a two layer tropospheric structure favorable for the development of trapped lee waves, three different behaviors are encountered. If the atmosphere is convectively unstable, any clouds which form act like buoyant plumes and destroy the lee waves. If the effective moist stability in the wave environment is weak, but positive, the waves are distorted and untrapped as the upstream humidity increases. If there is strong

moist stability in the lowest layer, changes in the upstream humidity change the tuning properties of the trapped waves. In the last instance, moisture can amplify or damp the wave, depending on the wavenumber spectrum of the orographic forcing.

In the real atmosphere, the potential influence of latent heating decreases, along with the available water vapor, as the temperature decreases with height. As a consequence, variations in the lower tropospheric humidity probably have a greater practical impact on lee wave dynamics than changes in the moisture content at higher levels. Nevertheless, there are at least two situations where changes in mid-tropospheric moisture can exert a significant influence on trapped lee waves. In the first, weak dry waves can be amplified by the addition of mid-level moisture which effectively reduces the height of the wave trapping interface. In the second case, the lower layer is very deep, so that in the absence of moisture, strong waves form with a single nodal line in the middle of the layer. If mid-level moisture is introduced, the deep two layer structure is destroyed, the waves weaken, and the nodal line disappears.

The investigation of trapped waves concentrated on atmospheres with a simple two-layer Scorer parameter structure. Although the windspeed and stabilities in those atmospheres were realistic, the Scorer parameter structure in any individual sounding would certainly be more complicated. In fact, when trapped lee waves are observed in the atmosphere, the actual Scorer parameter often has a rough two or three layer structure. The addition of a third layer is sometimes required by the presence of a well mixed layer near the ground. Corby

and Wallington (1956) have examined the effects of a low-level adiabatic layer on dry linear trapped waves and found that the general conclusions reached with a two-layer model are equally applicable to the three-layer situation. Thus, one might expect that in most instances, the influence of moisture on trapped waves in the real atmosphere should be qualitatively similar to the behaviors in the two level cases described here.

In the study of propagating waves, the only atmospheres examined were ones in which the dry Scorer parameter did not change abruptly with height, so there was little downward partial reflection of wave energy (at least in the dry case). Although the windspeed profiles examined were realistic, the assumption of constant stability was not. During actual mountain wave events there is likely to be a region of relatively low stability in the upper troposphere sandwiched between regions of high stability in the stratosphere and lower troposphere. Partial reflections may occur from sharp gradients in the Scorer parameter structure at the layer interfaces, which significantly change the wave amplitude. In such multi-layer situations, the presence of moisture might greatly modify the waves by tuning or detuning the Scorer parameter structure. The study of moisture effects on propagating waves in multi-layer atmospheres certainly warrants further research. Nevertheless, the basic nonreflective, constant stability cases presented here are very useful for a first investigation such as this, since they are simple, yet reasonably realistic. However, because of this limitation, the

results presented in this thesis should not be generalized to propagating waves in which the atmospheric stability changes rapidly with height.

In the nonreflective case, when precipitation is not present clouds act to damp the waves and reduce the momentum flux. This effect is stronger in finite amplitude waves than in their small amplitude counterparts. When precipitation occurs, the wave amplitudes and momentum fluxes are stronger than those produced by nonprecipitating flows, but still significantly weaker than in the dry case. The investigation of precipitation effects was limited to moisture profiles where the relative humidity upstream was uniform with height, or concentrated in low level clouds. Other behaviors might be produced by different moisture distributions and this possibility should be considered in future investigations, but since the temperature, and hence the potential for large amounts of latent heating, decreases rapidly with height in the real atmosphere, the profiles considered may be the most physically significant.

When precipitation occurs, the momentum flux in the propagating waves is not constant with height. It is not trivial to predict apriori how the latent heat release in precipitating waves will affect the momentum flux divergence, but since the strong momentum fluxes associated with large propagating waves can have a significant impact on the synoptic scale flow, this area also deserves further research. One might start with the work of Smith and Lin (unpublished manuscript) who discuss the effects of externally specified heating on linear hydrostatic waves.

In both trapped and propagating waves, one could try to approximate the effects of moisture by assuming that the flow is completely saturated in certain horizontal layers, and replacing the dry stability with a suitably reduced stability representative of that in the saturated flow. In the propagating wave case it seems possible to roughly estimate the actual flow by such a procedure. In the trapped wave case, a better result can generally be obtained by ignoring moisture altogether and estimating the wave structure based on the dry flow. However, both of these procedures yield only rough estimates which can be misleading, particularly when the saturated stability is low. An accurate calculation of the flow can only be obtained by explicitly including the moisture field in the computations.

VIII. REFERENCES

Barcilon, A., J. C. Jusem and S. Blumsack, 1980: Pseudo-adiabatic flow over a two-dimensional ridge. Geophys. Astrophys. Fluid Dynamics, 16, 19-33.

Barcilon, A., J. C. Jusem and P. G. Drazin, 1979: On the two-dimensional hydrostatic flow of a stream of moist air over a mountain ridge. Geophys. Astrophys. Fluid Dynamics, 13, 125-140.

Booker, D. R., 1963: Modification of convective storms by lee waves. Meteorological Monographs 5(7), Boston, Amer. Meteor. Soc., 129-140.

Claus, A. J., 1964: Large amplitude motion of a compressible fluid in the atmosphere. J. Fluid Mech., 19, 267-289.

Clark, T., 1977: A small scale dynamic model using a terrain following coordinate transformation. J. Comput. Phys., 24, 186-

Clark, T., and W. Peltier, 1977: On the evolution and stability of finite amplitude mountain waves. J. Atmos. Sci., 34, 1715-1730. 215.

Corby, G. A. and C. E. Wallington, 1956: Airflow over mountains: the lee wave amplitude. Quart. J. Roy. Meteor. Soc., 82, 266-274.

Deardorff, J. W., 1976: On the entrainment rate of a stratocumulus-topped mixed layer. Quart. J. Roy. Meteor. Soc., 102, 563-582.

Deardorff, J. W., 1972: Numerical investigation of neutral and unstable planetary boundary layers. J. Atmos. Sci., 29, 91-115.

Deardorff, J. W., 1971: On the magnitude of the subgrid scale eddy coefficient. J. Comput. Phys., 7, 120-133.

Eliassen, A., and E. Palm, 1960: On the transfer of energy in stationary mountain waves. Geofys. Publ., 22, 1-23.

Fraser, A., R. Easter and P. Hobbs, 1973: A theoretical study of the flow of air and fallout of solid precipitation over mountainous terrain: Part I. Airflow model. J. Atmos. Sci., 30, 801-812.

Gal-Chen, T., and R. Somerville, 1975: Numerical solution of the Navier-Stokes equations with topography. J. Comput. Phys., 17, 209-223.

Holmboe, J., and H. Klieforth, 1957: Investigations of mountain waves and the airflow over the Sierra Nevada. Final Report, Contract No. AF 19(604)-728.

Klemp, J. B., and D. K. Lilly, 1980: Mountain waves and momentum flux. Orographic Effects in Planetary Flows, GARP Publication Series 23, 116-142.

Klemp, J., and D. K. Lilly, 1978: Numerical simulation of hydrostatic mountain waves. J. Atmos. Sci., 35, 78-106.

Klemp, J., and R. Wilhelmson, 1978: The simulation of three-dimensional convective storm dynamics. J. Atmos. Sci., 35, 1070-1096.

Klemp, J., and D. K. Lilly, 1975: The dynamics of wave-induced downslope winds. J. Atmos. Sci., 32, 320-339.

Larsson, L., 1954: Observations of lee wave clouds in the Jämtland Mountains, Sweden. Tellus, 6, 124-138.

Lilly, D. K. and J. B. Klemp, 1980: Comments on "The evolution and stability of finite amplitude mountain waves. Part II: Surface drag and severe downslope windstorms." J. Atmos. Sci., 37, 2119-2121.

Lilly, D. K. and J. Klemp, 1979: The effects of terrain shape on nonlinear hydrostatic mountain waves. J. Fluid Mech., 95, 241-261.

Lilly, D. K., 1978: A severe downslope windstorm and aircraft turbulence event induced by a mountain wave. J. Atmos. Sci., 35, 59-77.

Lilly, D. K., 1962: On the numerical simulation of buoyant convection. Tellus, 14, 148-172.

Lilly, D. K., 1960: On the theory of disturbances in a conditionally unstable atmosphere. Mon. Wea. Rev., 88, 1-17.

Long, R., 1955: Some aspects of the flow of stratified fluids. III. Continuous density gradients. Tellus, 7, 341-357.

Long, R., 1953: Some aspects of flow of stratified fluids. I. A theoretical investigation. Tellus, 5, 42-58.

Lyra, G., 1943: Theorie der stationären Leewellenströmung in freier Atmosphäre. Z. angew. Math. Mech., 23, 1-28.

Miles, J., 1969: Waves and wave drag in stratified flows. Proc. 12th Int. Cong. Appl. Mech., Hetenyi and Vincenti Eds., Springer-Verlag, 52-76.

Miles, J. W. and H. E. Huppert, 1969: Lee waves in a stratified flow. Part 4. Perturbation approximations. J. Fluid Mech., 35, 497-525.

Miles, J., 1968: Lee waves in a stratified flow. Part 2. Semi-circular obstacle. J. Fluid Mech., 33, 803-814.

Orlanski, I., 1976: A simple boundary condition for unbounded hyperbolic flows. J. Comp. Phys., 21, 251-269.

Peltier, W. R. and T. L. Clark, 1980: Reply. J. Atmos. Sci., 37, 2122-2125.

Peltier, W. R., and T. L. Clark, 1979: The evolution and stability of finite-amplitude mountain waves. Part II. Surface wave drag and severe downslope windstorms. J. Atmos. Sci., 36, 1498-1529.

Queney, P., G. Corby, N. Gerbier, H. Koschmieder, and J. Zierep, 1960: The airflow over mountains. WMO Tech Note 34.

Queney, P., 1948: The problem of air flow over mountains: A summary of theoretical studies. Bull. Amer. Met. Soc., 29, 16-25.

Queney, P., 1947: Theory of perturbations in stratified currents with application to airflow over mountain barriers. The Univ. of Chicago Press, Misc. Rep. No. 23.

Scorer, R., 1949: Theory of waves in the lee of mountains. Quart. J. Roy. Meteor. Soc., 75, 41-56.

Smith, R. B., 1977: The steepening of hydrostatic mountain waves. J. Atmos. Sci., 34,. 1634-1654.

Smith, R. B., 1976: The generation of lee waves by the Blue Ridge. J. Atmos. Sci., 33, 507-519.

Soong, S-T. and Y. Ogura, 1973: A comparison between axi-symmetric and slab-symmetric cumulus cloud models. J. Atmos. Sci., 30, 879-893.

Vergeiner, I., 1971: An operational lee wave model for arbitrary basic flow and two dimensional topography. Quart. J. Roy. Meteor. Soc., 97, 30-60.

APPENDIX: LIST OF SYMBOLS

A_r autoconversion of cloud to rain

a half-width of Witch of Agnesi Mountain

C_r collection of cloud by raindrops

$\bar{c}$ mean state speed of sound

c_p specific heat of air at constant pressure

c_v specific heat of air at constant volume

f Coriolis parameter

g effective gravity

k horizontal wavenumber

k_r resonant horizontal wavenumber

k_s Scorer parameter

K_H eddy diffusivity of heat

K_M eddy diffusivity of momentum

H depth of the lower layer in the two layer trapped-wave atmospheres

h height of Witch of Agnesi mountain

L latent heat of condensation

M momentum flux computed by numerical simulation

M_{LC} linear hydrostatic momentum flux for an atmosphere with constant windspeed and stability (also M_L)

M_{LS} linear hydrostatic momentum flux for an atmosphere with constant wind shear and stability

M_p pressure drag across the mountain

N Brunt-Väisälä frequency

N_E effective Brunt-Väisälä frequency for small displacements in saturated air

p pressure

q_v mixing ratio of water vapor

q_c mixing ratio of cloud water

q_r mixing ratio of rain water

q_{vs} saturation mixing ratio

R gas constant for dry air

RH relative humidity

T sensible temperature

u horizontal velocity

V raindrop fall speed

x horizontal coordinate perpendicular to the mountain ridge axis

w vertical velocity

z vertical coordinate

z_s terrain height

z_T height of the top of the modeling region

γ_d dry adiabatic lapse rate

γ_m moist adiabatic lapse rate

δ deviation of a streamline from its height far upstream

ϵ ratio of the molecular weights of dry air and water vapor

θ potential temperature

θ_E equivalent potential temperature

θ_M $\theta(1 + .61\ q_v)(1 - q_c - q_r)$

ζ transformed vertical coordinate

π perturbation nondimensional pressure

$\bar{\Pi}$ mean nondimensional pressure

ρ density of moist air